A ROBUST WIRELESSLY-POWERED RECORDING AND STIMULATION SYSTEM FOR A FREELY-MOVING ANIMAL SUBJECT

A Dissertation

Presented to

The Academic Faculty

By

Byunghun Lee

In Partial Fulfillment

Of the Requirements for the Degree

Doctor of Philosophy in the

School of Electrical and Computer Engineering

Georgia Institute of Technology

May 2017

A Robust Wirelessly-powered Recording and Stimulation System for a Freely-moving Animal Subject

Approved by:

Dr. Maysam Ghovanloo, Advisor
School of Electrical and Computer Engineering
Georgia Institute of Technology

Dr. Omer T. Inan
School of Electrical and Computer Engineering
Georgia Institute of Technology

Dr. John D. Cressler
School of Electrical and Computer Engineering
Georgia Institute of Technology

Dr. Yoonsu Choi
Department of Electrical Engineering
University of Texas, Rio Grande Valley

Dr. Hua Wang
School of Electrical and Computer Engineering
Georgia Institute of Technology

Date Approved: March 30, 2017

Table of Contents

LIST OF TABLES

LIST OF FIGURES

SUMMARY

The objective of my research was to develop a robust wirelessly-powered recording and stimulation system for a freely-moving animal subject. Several innovative system- and circuit-level techniques are proposed towards the development of a novel wireless power transfer (WPT) system and an inductively-powered wireless implantable neural-recording and stimulation system (WINeRS-8) for a freely-moving animal subject.

My research goal is composed of two parts: 1) several WPT systems for a transmitter (Tx), 2) a wireless recording/stimulating system in a receiver (Rx). In the WPT systems, a triple-loop WPT system is proposed to keeps the power transfer efficiency (PTE) dynamically at its peak by simultaneously operating three loops, while maintaining the system robustness and stability. In addition, a new Q-modulation method is demonstrated which can maintain the high PTE in wirelessly powered applications that operate in dynamic environments with motion and variable loading. A new architecture for a three-phase time-multiplexed power Tx, which has ability to wirelessly power a large number of distributed receivers with arbitrary angle and spatial misalignments across a large plane is proposed. The wirelessly-powered homecage system, called the EnerCage-HC, that is equipped with a multi-coil WPT, an optical behavioral tracking, and a graphic user interface (GUI) is proposed for long-term behavioral experiments with implantable medical devices (IMDs). In the wireless recording/stimulating system, a completed inductively-powered wireless implantable neural recording and stimulation system, called WINeRS-8 is presented. The WINeRS-8 system equips 32-channel adaptive averaging low noise analog front-end (AFE) with 10-bit successive approximation ADC (SAR-ADC), which is suitable for central and peripheral nerve recording applications. The transmitted RF signal from WINeRS-8 is detected by two individual software-defined ratio (SDR) receiver (Rx) to increase the directivity and coverage of the received RF signal over the experimental space, resulted in the reduced

RF Tx power consumption in the mobile unit. In two *in vivo* experiments, five types of WINeRS-8 headstage and implantable device are designed to demonstrate the recording and stimulating functionalities for the central/peripheral nervous system in the EnerCage-HC2 system. To the best of our knowledge, the proposed WINeRS-8 system is the first wirelessly powered implanted device without the battery for the central and peripheral nerve recording/stimulation on a freely-moving animal subject while providing the tracking functions.

My contributions in this research work are summarized as follows:

1. Development of an triple-loop power transmission system
2. Analysis and development of a multi-cycle Q-modulation power transfer system
3. Analysis and development of three-phase time-multiplexed power transfer system for distributed implants
4. Development of a smart wirelessly power homecage system equipped with 2D/3D animal subject tracking
5. Development of adaptive averaging low noise front-end for central and peripheral nerve recording
6. Development of a wireless neural recording RF receiver using software defined radio for wideband data transmission
7. Implementation of near-field data transmission between a wirelessly-powered homecage and mobile unit
8. Development and *in vivo* experiments of new inductively-powered neural recording and stimulation system compatible with a wirelessly-powered homecage for a freely-moving animal.

I. INTRODUCTION

Behavioral neuroscience research on small awake animal subjects, such as rodents, has benefited from recent advances in neural interfacing technology. Neural interfaces have been traditionally hardwired to deliver power and communicate with neural recording or stimulation instruments attached to the animal body, called a mobile unit, thereby restricting experiments that involve freely behaving animal subjects [1]. These studies also require labor-intensive human operator involvement to ensure continuous and smooth flow of the experiments, which imposes a barrier to conducting long-term experiments over the span of several days, weeks, or months. In an attempt to overcome the limitations imposed by cables, several battery-powered neural recording systems have been developed [2]-[4]. Although these setups can eliminate the cables from the mobile unit, they are still not suitable for longitudinal studies due to the limited lifetime of the batteries, which also add to the animal payload.

In order to address these limitations, a few wirelessly-powered system have been developed to either directly power the mobile unit or recharge the batteries during the experiment [5]-[10]. These wirelessly-powered systems are composed of a wireless power Tx, equipped with one or several Tx coils to wirelessly power up the mobile unit, and wireless implantable microelectronic devices (IMDs) in the mobile unit for recording or stimulating capability. Fig. 1.1 shows a conceptual view of the wirelessly-powered system with recording/stimulation in the mobile unit for long-term experiment on freely-moving small animals [11]. However, conventional wireless power Tx suffered from poor PTE because the coil geometries were not optimized. Moreover, when there is a need for higher received power, e.g. wireless neural stimulation, the heat dissipation on the Tx side can be prohibitive because the entire cage volume is continuously powered, as opposed to where the animal is located. In IMDs, high PTE is also desired to reduce heat dissipation in the coils, exposure to electromagnetic field, which can cause

additional heat dissipation in the medium, size of the external energy source, and interference with nearby electronics that is necessary to satisfy regulatory requirements [12]-[14].

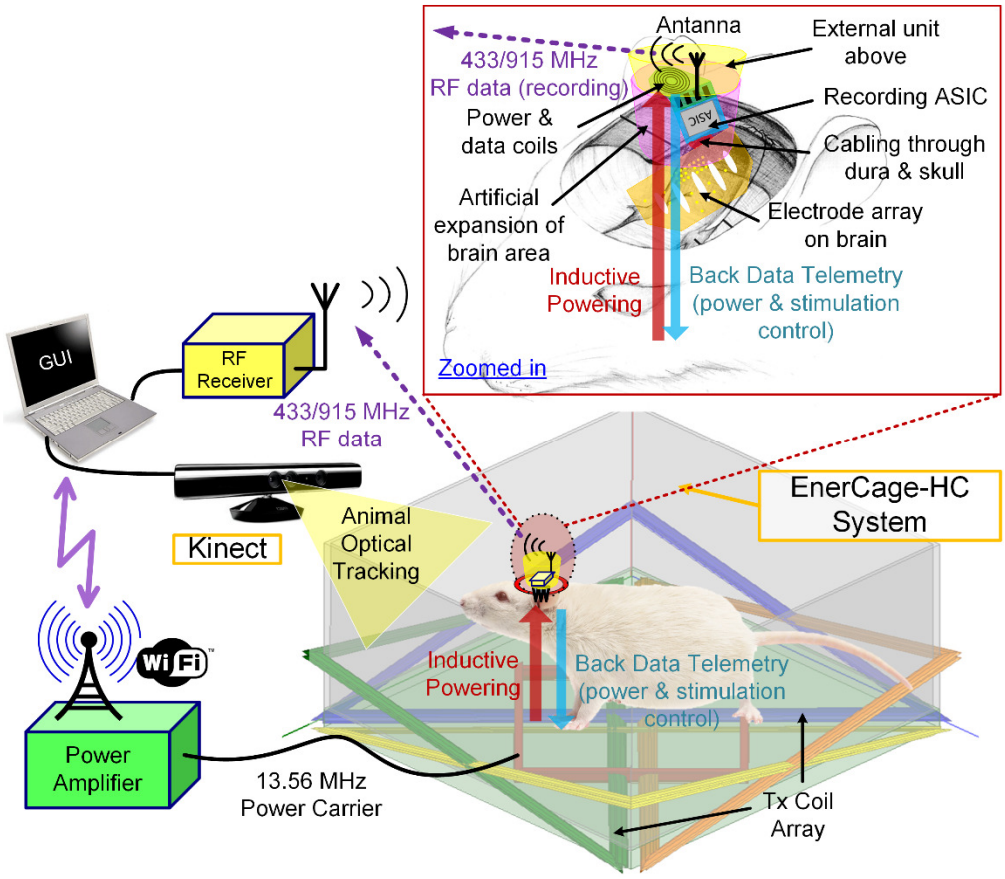

Fig. 1.1 Conceptual view of the wirelessly-powered system with recording/stimulation in mobile unit for long-term experiment on freely-moving small animals.

1.1 Wireless Power Transmission System for Implantable Microelectronic Devices (IMDs)

In inductive power transmission, which its principle is based on the Faraday's law, a primary loop generates the varying magnetic field that results in an induced current in the secondary loop as shown in Fig. 1.2. Inductive power transfer is used in many IMDs to enhance their performance by increasing the number of electrodes, stimulation current, and stimulus rate [13]-[18]. Compared to batteries or transcutaneous interconnects, inductive powering is safer, more convenience for the patient, and smaller

in size. Inductive links have also been used in near-field radio-frequency identification (RFID) to power up and interrogate transponders [19]. More recently, inductive link have also gained attention in charging mobile electronics [20][21]. The Tx in an inductively-powered system includes a power amplifier (PA) followed by a matching circuit and the primary coil, L_2. In a 3-coil configuration, the Rx includes two coils, L_3 and L_4, in which L_4 is used for impedance matching with the load, followed by a power management circuitry for voltage rectification and regulation [22]-[24]. Since high PTE is desired to reduce heat dissipation in the coils, exposure to electromagnetic field, size of the external energy source, and interference with nearby electronics, several methods have been proposed to enhance the PTE, such as geometrical optimization of the 2-, 3-, 4-coil inductive links [22]-[29]. However, in practice, optimizing the coil geometries alone is not sufficient to maintain the high PTE.

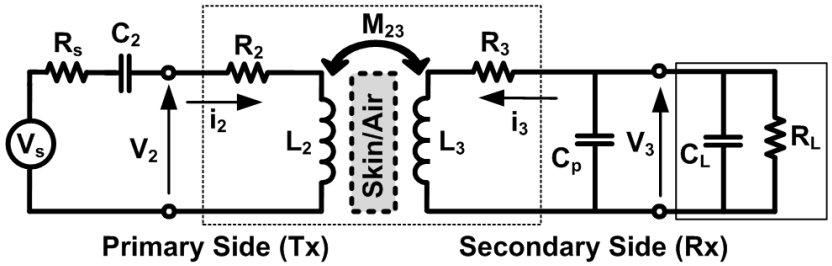

Fig. 1.2. An inductive link with resonance circuits to increase the secondary voltage, V_3.

In addition to the geometry and alignment, the PTE highly dependent on how well the Tx and Rx tank circuits are tuned at the operating frequency, f_p [30]. In IMDs, the inductive link often adversely affected by the parasitic capacitance of the surrounding tissue environment, which can significantly degrade the PTE, particularly when the Q-factor is high [26]. A few methods have been proposed to adaptively tune the Rx LC-tank [31][32]. These methods employ a variable LC-tank on the Rx side to compensate for variations in the Rx resonance capacitance. However, the Tx LC-tank detuning could still degrade the wireless link PTE. In particular, if the Tx coil happens to be planar and flexible to better conform to the outer body profile, both L_2 and parasitic components of

the resonance capacitor, C_2, could continuously change on the Tx side with subject's body motion. To address this issue, an adaptive Tx that adjusts either the carrier frequency or the matching circuit of the Tx coil can be used. The adaptive f_p that tends to overcome the PTE degradation in real-time has been demonstrated in [33]-[35]. However, it could be inefficient when LC matching network with high Q-factor or frequency-sensitive PA topologies, such as a class-E amplifier, have been used. Moreover, compliance with regulations could be more complicated with a variable f_p and a simple Rx may not be able to continuously track the f_p variations.

Closed-loop power control is also required for efficient power transfer in the presence of coil coupling and loading variations [36]-[38]. Either the PA output power or f_p is adaptively adjusted to maintain the Rx voltage constant in the presence of perturbations. Although each control loop and a combination of two loops has been implemented and discussed in the literature [31][32][39], a complete system with all three loops working together in real time to address all the aforementioned issues has not been demonstrated.

1.2 Smart Wireless Power Transmission System for a Freely-Moving Animal

The conventional wirelessly-power cages are shown in Fig. 1.3. To address the limitations of the conventional wirelessly-powered systems, which directly power the mobile unit or recharge the batteries with the poor PTE during the experiment [5]-[10], smart wirelessly-powered systems have been reported, which can significantly improve the PTE [40]-[45]. In these systems, batteries on the mobile units have been eliminated or replaced by smaller capacitors, and an array of coils at the bottom of the experimental arena are automatically selected based on the position of the animal subject to couple with the power Rx in the mobile unit. As an alternative, a single Tx coil mechanically moving on XY-rails was also reported in [46]. Although these system can achieve high PTE and operate at low temperature, they are too bulky to be integrated with the standard

homecage in a way that high throughput experiments can run in parallel over extended periods of time inside the animal research facilities without occupying the lab space and limited human resources of research laboratories. Moreover, the animal subject tracking resolution and quality in the earlier work were not sufficient for behavioral experiments.

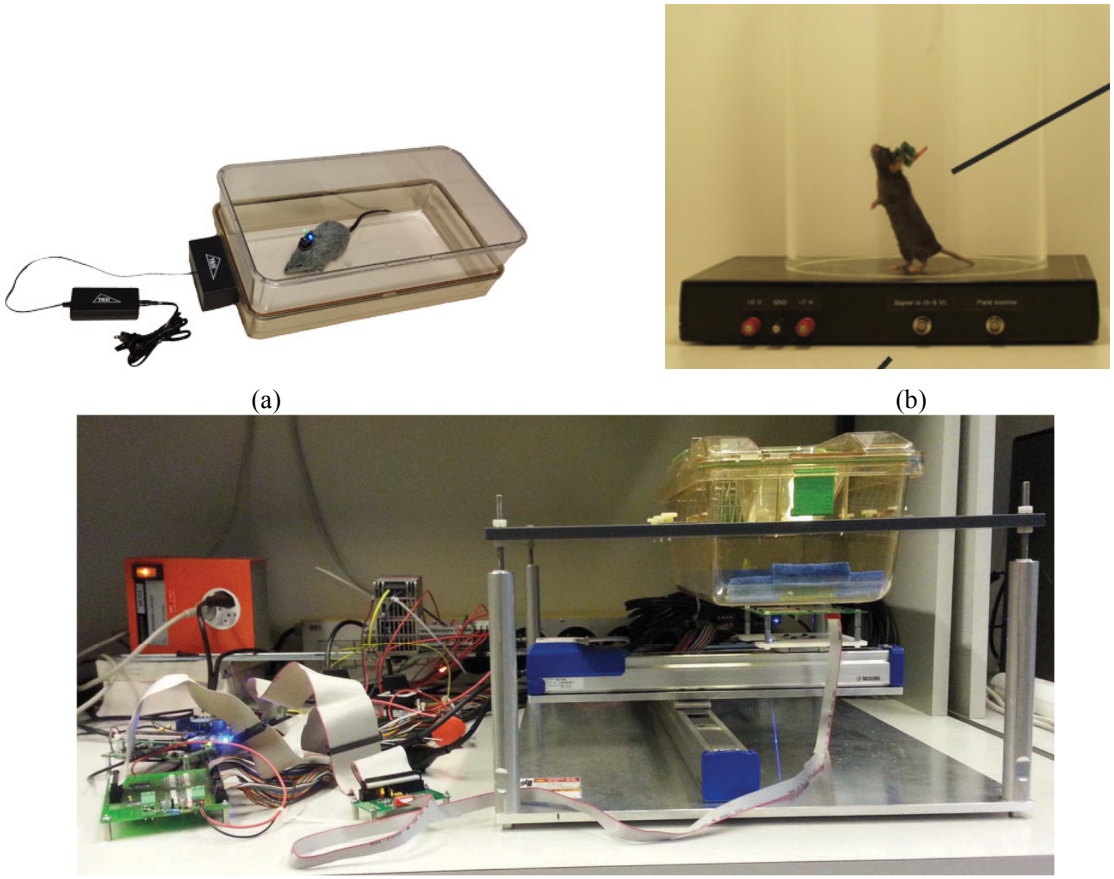

(a) (b)

(c)

Fig. 1.3. Conventional wirelessly-power cages. (a) Wireless charging system by [9], (b) by [11], and (c) by [46].

Tracking animal subjects to analyze the locomotion has been separately studied on different animal species including rodents [47]-[50]. Automated locomotion measurement using computer vision can improve accuracy and significantly lower the cost of labor, thus it is rapidly growing [51]-[53]. Microsoft Kinect® is a popular, high precision and low-cost imager that is equipped with infrared depth (IR-3D) and Red-Green-Blue (RGB-2D) cameras, allowing animal tracking in both bright and dark

conditions. This is particularly important for nocturnal animal species, which include most rodents. Kinect® has been recently adopted in a few automated locomotion tracking experiments [54][55]. However, only the depth camera has been previously used for tracking the subject's position in real time.

1.3 Wireless Power Transmission System for Distributed Implants

Recently, neuroscientists are asking for advanced tools capable of recording the activities of individual neurons from all over the brain because most brain functions are also distributed [56]-[58]. In addition to area coverage, it is important to maintain a high spatial resolution in recording brain activity. The highest spatial resolution is provided by small electrodes inserted in the brain to record extra cellular activities of nearby neurons, leading to single unit activity (SUA) recording. Good area coverage with lower spatial resolution is offered by electro-corticography (ECoG) and electroencephalography (EEG) with planar electrodes that are implanted on the surface of the brain or under the scalp, respectively [56]. The lack of proper tools for obtaining high spatial resolution signals over large areas in the brain over extended periods is considered one of today's key challenges in neuroscience research.

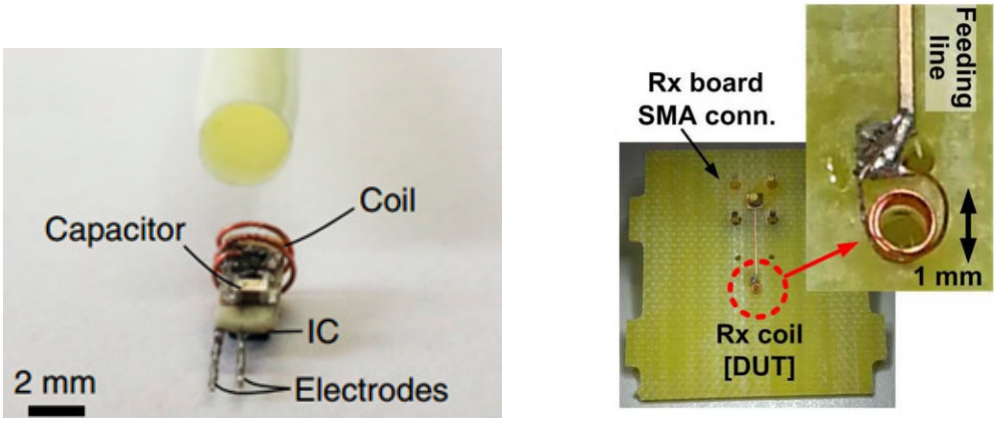

(a) (b)

Fig. 1.4. Single miniature Rx coil for distributed implants. (a) Wireless cardiac pacing [69], and (b) optimized Rx coil for mm-size distributed implants [70].

Instead of the conventional single, large, and centralized implant, a large number of tiny implants, distributed over a large brain area has been proposed as an alternative for recording from the brain [59][60]. In the distributed system architecture, implants are small, wireless, central rigid, and form a large network [61]. Therefore, the main constrains for these distributed implants are size, power, and functionality. Neither batteries nor other large storage elements, such as super-capacitors, are feasible in a distributed architecture. Energy harvesting from glucose fuel cell [62], thermoelectric [63], or piezo transducers [64] have been proposed, but unlikely to provide sufficient power for the desired functionality [65]. Ultrasonic power transfer might be an option. However, since ultrasound cannot penetrate through the skull, it can only be used either for short distance of a few mm across the cortical membranes, e.g. dura, or for deeper targets through soft tissue, e.g. in peripheral nerve interfacing [60]. Electromagnetic WPT, on the other hand, can penetrate through hard and soft tissue, while providing high power density [66]-[69]. Even though several focused WPT methods for a single miniature implant have been proposed [70]-[73] as shown in Fig. 1.4, there has been few external power Tx designed for numerous floating implants with arbitrary angular and spatial misalignments, distributed all over a large brain area, as shown in Fig. 1.5.

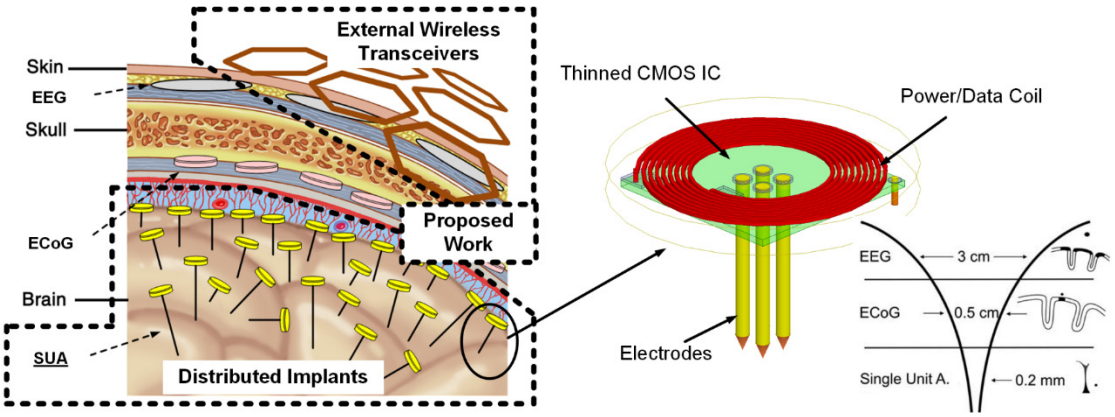

Fig. 1.5. Rendered view of a distributed brain-computer interface (BCI). Three different categories of recording devices, i.e. EEG, ECoG, and SUA, powered and communicated by an external hexagonal planar spiral coil (PSC) array [74].

1.4 Wireless Powered Neural Recording/Stimulation System

Over the past few years, multichannel neural-recording and stimulation systems have been developed for minimum disturbance to animal subject. Wireless recording system has several advantages in comparison to conventional wired operation in terms of no tethering effects, a lower risk of infection, smaller size, and easy usage as shown in Fig. 1.6a. However, a key limitation of common wireless neural-recording systems is the need for the animal subject to carry a large payload of batteries. This may not matter when recording from costly primates [75]. However, most labs use small animals, such as rats and mice, for which there must be a compromise between the size and weight of the headstage and the uninterrupted duration of the experiments as shown in Fig. 1.6b. The ability to conduct long-term uninterrupted recording is very attractive to neuroscientists because the neural population under analysis often changes over time. Therefore, overnight recording is needed to track neurons over an extended period of time for learning studies, or for combining experimental trials across consecutive days [76].

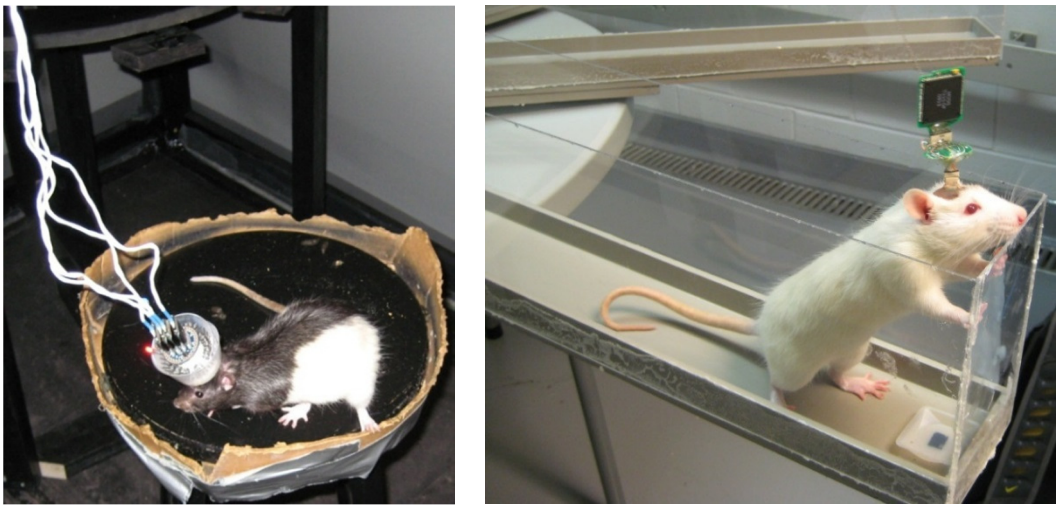

(a) (b)

Fig. 1.6. Conventional neural recording and stimulation system using (a) hard-wired connection and (b) battery-powered wireless data transmission [77].

Some applications require a system that interacts bidirectionally with the central and peripheral nervous system. For example, deep brain stimulation (DBS), which is an

effective neuro-modulation therapy for Parkinson's disease (PD), requires neural recording for closed-loop operation. Shahrokhi et al. developed a 128-channel neural recording and stimulation interface [78], but it did not operate with a wireless system, featured no stimulus-artifact rejection, and did not be used to perform *in vivo* experiments. Lee et al. introduced 64-channel stimulators and an 8-channel neural-recording system [79] with an external wireless micro controller. Azin et. al. used two identical 4-channel modules in one SoC [80]. However, there has been no wirelessly-powered recording and stimulation device for a freely-moving animal subject.

The structure of the dissertation is as follows: In Chapter II, a high-efficiency and adaptive wireless power transfer system is proposed by introducing triple-loop wireless inductive link and the concept of multi-cycle Q-modulation technique with theoretical calculation, simulation and measurement results. Chapter III includes a new architecture for a three-phase time-multiplexed scalable power Tx which has the ability to wirelessly power a large number of distributed Rx with arbitrary angular and spatial misalignments across a large plane. Chapter IV describes a novel wireless platform for electrophysiology experiments inside the standard homecage called EnerCage-HC, which takes advantage of multi-coil coupling and Kinect® based optical localization to offer an efficient and low-cost technology for wireless powering any electronics attached to a small animal subject and tract its behavior. Chapter V proposes a robust wireless implantable neural and peripheral recording and stimulation (WINeRS-8) system fully compatible with the EnerCage-HC system and *in vivo* experimental results in chapter VI. Finally, the contributions of this dissertation and suggested future works are summarized in Chapter VII.

II. HIGH-EFFICIENCY AND ADAPTIVE WIRELESS POWER TRANSMISSION SYSTEM

In this chapter, two novel techniques are presented for high-efficiency and adaptive wireless power transmission system in 2- or 3- coil inductive link. A triple-loop wireless power transmission system equipped with closed-loop global power control, adaptive transmitter (Tx) resonance compensation (TRC), and automatic receiver (Rx) resonance tuning (ART) is presented. This system not only opposes coupling and load variations but also compensates for changes in the environment surrounding the inductive link to enhance power transfer efficiency (PTE) in applications such as implantable medical devices (IMDs). The Tx was built around a commercial off-the-shelf (COTS) radio- frequency identification (RFID) reader, operating at 13.56 MHz. A local Tx loop finds the optimal capacitance in parallel with the Tx coil by adjusting a varactor. A global power control loop maintains the received power at a desired level in the presence of changes in coupling distance, coil misalignments, and loading. Moreover, a local Rx loop is implemented inside a power management integrated circuit (PMIC) to avoid PTE degradation due to the Rx coil surrounding environment and process variations.

A new method, called multi-cycle Q-modulation, can be used in wireless power transmission (WPT) to modulate the quality factor (Q) of the Rx coil and dynamically optimize the load impedance to maximize the PTE in especially two-coil links. A key advantage of the proposed method is that it can be easily implemented using off-the-shelf components without requiring fast switching at or above the carrier frequency, which is more suitable for integrated circuit design. Moreover, the proposed technique does not need any sophisticated synchronization between the power carrier and Q-modulation switching pulses. The multi-cycle Q-modulation is analyzed theoretically by a lumped circuit model, and verified in simulation and measurement using an off-the-shelf prototype. The ART in the Rx, combined with multi-cycle Q-modulation helped maximizing PTE of the inductive link dynamically in the presence of environmental and

loading variations, which can otherwise significantly degrade the PTE in multi-coil settings.

2.1 A Triple-loop Inductive Power Transmission System for Biomedical Applications

2.1.1 System Overview

The Tx in an inductively-powered system includes a power amplifier (PA) followed by a matching circuit and the primary coil, L_2, as shown in Fig. 2.1. In a 3-coil configuration, the receiver (Rx) includes two coils, L_3 and L_4, in which L_4 is used for impedance matching with the load, followed by a power management circuitry for voltage rectification and regulation [22]-[24].

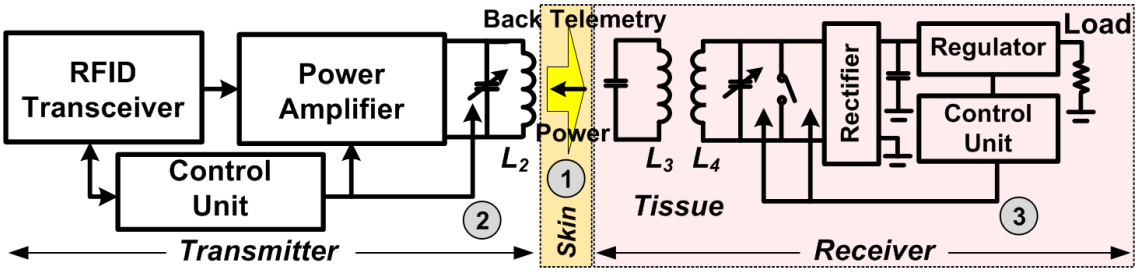

Fig. 2.1. Triple-loop inductive wireless power transmission using a 3-coil link.

The PTE is highly dependent on how well the Tx and Rx tank circuits are tuned at the operating frequency, f_p [30]. In IMDs, the inductive link is often adversely affected by the parasitic capacitance of the surrounding tissue environment, which can significantly degrade the PTE, particularly when the Q-factor is high [25]. A few methods have been proposed to adaptively tune the Rx LC-tank [31], [32]. These methods employ a variable LC-tank on the Rx side to compensate for variations in the Rx resonance capacitance. However, the Tx LC-tank detuning could still degrade the wireless link PTE. In particular, if the Tx coil happens to be planar and flexible to better conform to the outer body profile, both L_2 and parasitic components of C_2 in Fig. 2.1 could continuously change on the Tx side with body motion. To address this issue, an adaptive Tx that adjusts either the carrier

frequency or the matching circuit of the Tx coil can be used. The adaptive f_p that tends to overcome the PTE degradation in real-time has been demonstrated in [33]-[35]. However, it could be inefficient when LC matching network with high Q-factor or frequency-sensitive PA topologies, such as class-E have been used. Moreover, compliance with regulations could be more complicated with a variable f_p and a simple Rx may not be able to continuously track the f_p variations.

Closed-loop power control is also required for efficient power transfer in the presence of coil coupling and loading variations [36]-[38]. Here, either the PA output power or f_p is adaptively adjusted to maintain the Rx voltage constant in the presence of perturbations. Although each control loop and a combination of two loops has been implemented and discussed in the literature ([31], [32], and [39]), a complete system with all three loops working together in real time to address all the aforementioned issues has not been demonstrated.

A triple-loop wireless power transmission system is demonstrated that includes 1) closed-loop power control, 2) adaptive Tx resonance compensation (TRC), and 3) automatic Rx resonance tuning (ART). The proposed system keeps the PTE of the wireless power transmission system dynamically at its peak by simultaneously operating these three loops, while maintaining the system robustness and stability. The Tx is built around a commercial off-the-shelf (COTS) RFID reader, operating at f_p =13.56 MHz. To reduce size and power consumption, we have designed an application-specific power management integrated circuit (PMIC) for the Rx, which uses load-shift keying (LSK) for back telemetry [81].

2.1.2 System Architecture

Fig. 2.2 shows a simplified block diagram of the proposed triple-loop wireless power transmission system. In this system, a .56 MHz RFID reader (TRF7960) on the Tx side drives L_2 and recovers back telemetry data from the Rx. Independent loops in Tx

adjust the LC-tank resonance capacitance (C_{Tx}) and PA supply voltage (VDD_PA) to compensate for any environmental or physical (e.g. L_2 deformation) detuning and coupling/loading variations, respectively. On the Rx side, the PMIC ASIC rectifies and regulates the 13.56 MHz power carrier and tunes the Rx LC-tank at the operation frequency, f_p. The rectifier voltage, V_{REC}, is divided in half and digitized in 10 bits by an MSP430 microcontroller, which combines them with start bits, "01", following a 300 µs-long stream of zeroes, and sends them back to the Tx through the PMIC ASIC by shorting L_4 at a rate of 250 kHz. V_{REC} information on the Tx side is then used by both the TRC and power control loops.

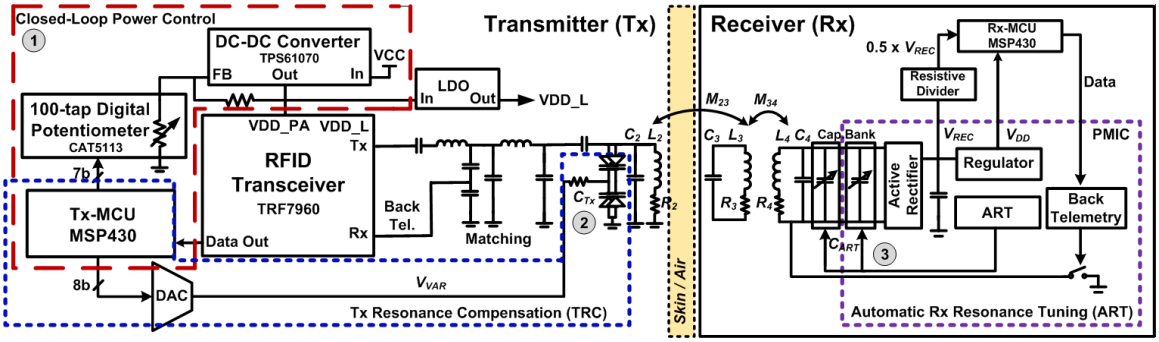

Fig. 2.2. Block diagram of the triple-loop power transmission system. An RFID reader on the Tx side drives the primary coil, L_2, at f_p = 13.56 MHz and recovers the LSK back telemetry data from the Rx. On the Tx side, first control loop adjusts the power amplifier supply (VDD_PA) to oppose coils' coupling and Rx loading variations. A second control loop (TRC) tunes the Tx LC-tank to compensate for any detuning due to environmental or physical changes to L_2. On the Rx side, a high efficiency power management IC (PMIC) rectifies the AC carrier and a third loop (ART) automatically tunes the Rx LC-tank at f_p. A low power MCU digitizes $V_{REC}/2$ and sends the data serially to the PMIC to be keyed back to the RFID reader. This info is used for both closed-loop power control and Tx LC-tank tuning.

The ART is implemented locally in the PMIC ASIC using a combination of internal and external switched-capacitor banks. The 13.56 MHz carrier is rectified by a high efficiency full- wave active rectifier, followed by a low dropout (LDO) regulator to provide V_{DD} = 3.3 V for the rest of the system [81].

The ART seeks maximum PTE in the presence of any undesired varying parasitic capacitance, C_{PAR}, imposed by the Rx surrounding environment (e.g. human body), by tuning L_4 at f_p = 13.56 MHz. In the ART block, two 5-bit binary-scaled on-chip and off-

chip capacitor banks are swept within L_4C_4- tank. The envelope of the carrier signal across L_4C_4-tank is sampled before and after stepping C_{ART} to decide the direction of the total capacitance change in real time. A small base capacitance, C_4, is added in parallel with L_4 for proper startup when the ART loop is off or disabled. The ART ensures that ($C_4 + C_{ART} + C_{PAR}$) perfectly resonates with L_4 at f_p.

The RFID reader not only drives L_2 by its built-in class-D PA but also recovers the LSK back telemetry signal, which is over- sampled by the Tx MCU (MSP430). V_{REC} data is then used to adjust the supply voltage of the PA (VDD_PA) inside the RFID reader. In this prototype, VDD_PA is generated by a high efficiency DC-DC converter (TPS61070), and it is adjustable from 3 V to 5.5 V in 100 steps through a digital potentiometer (CAT5113). The Tx MCU continuously searches for a 300 µs zero bit stream followed by the start bits "01". When "01" bits are detected, it recovers the rest of the 10 bits packet, which is V_{REC}. Considering the efficiency and dropout voltage of the LDO, the upper and lower threshold voltages are designated at 4.2 V and 3.6 V, respectively. To maintain V_{REC} inside a designated range of lower V_{RLT} = 3.6 V and upper V_{RUT} = 4.2 V thresholds, the binary value of $V_{REC}/2$ is compared with a programmable window (650 ~ 560) in the MCU. If $V_{REC} < V_{RLT}$, the MCU increases the VDD_PA and vice versa. If V_{REC} is inside the desired window, VDD_PA is not changed. In the presence of any external disturbance, the Tx MCU reduces or increases the transmitted power until it receives a value within 560-650 [37].

Although the Tx LC-tank can be manually tuned before its operation, in most applications, including IMDs, the resonance conditions constantly change during the operation when the Tx coil is exposed to variable surrounding environments or bends as a result of body movements. Therefore, an adaptive Tx LC-tank resonance compensation (TRC) circuit can improve the PTE. Based on our previous measurements in [26], parasitic capacitance variations for printed spiral coils (PSCs) with 2.4 cm in diameter can be up to 7.72 pF in the muscle environment.

The prototype TRC (Fig. 2.2) was composed of an MCU, an 8-bit digital-to-analog converter (DAC) (Max 522), and four varactors (SMV 1265). The MCU controls the DAC output voltage, V_{VAR}, and the total capacitance of the varactors, C_{Tx}, changes from 22.47 pF to 6.1 pF by changing V_{VAR} from 0 to 3.3 V. Anti-series configuration for varactors is utilized to achieve lower distortion than a single varactor connection [41]. The TRC loop changes V_{VAR} and the L_2C_2-tank resonance to achieve maximum V_{REC} for any particular VDD_PA value, which corresponds to the peak resonance condition on the Tx side.

2.1.3 Triple-Loop Control Algorithm

Fig. 2.3a shows the flowchart of the triple-loop control algorithm that maintains the rectifier voltage, V_{REC}, within a designated range in response to different types of external disturbances to the wireless power transmission link, while ensuring its high PTE and stability. In order to maintain simplicity of the system and low power consumption, we have avoided a central controller that would observe simultaneous operation of the three loops, which would have required a separate wireless data communication path. Instead, the control algorithm sequentially activates one loop at a time, normally in this order: 1) power, 2) TRC, and 3) ART, at the cost of a somewhat slower response time.

During start-up, the Tx MCU sets the DC-DC converter output to VDD_PA = 3 V, which corresponds to the lowest RF power. It gradually increases the VDD_PA until enough power is delivered to the PMIC to enable the back telemetry link. The RFID reader detects the LSK pulses and the global power control loop becomes operational. This loop has the highest priority in the system to ensure that Rx receives the minimum required power to remain operational. The programmable window (V_{RUT} - V_{RLT}) for V_{REC} limits fluctuations due to noise or instability. If the received V_{REC} through back telemetry

is outside this window, the power loop adjusts VDD_PA in proper direction until V_{REC} returns inside the desired range.

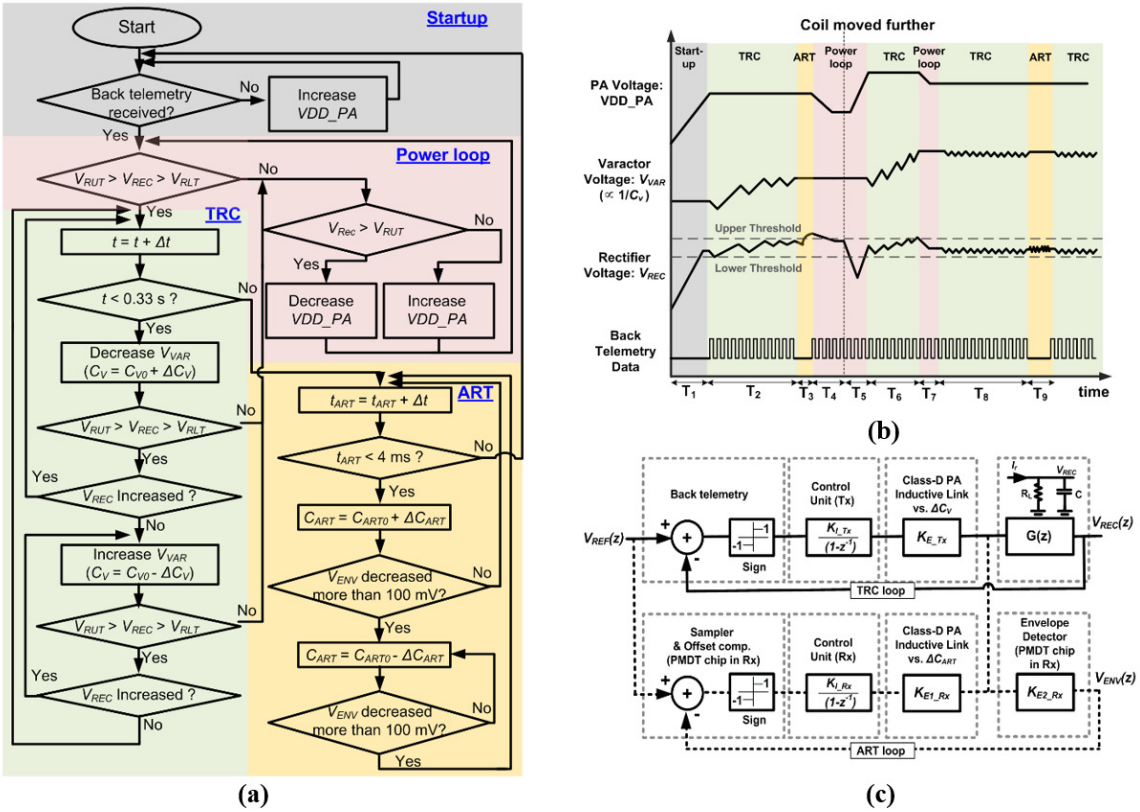

Fig. 2.3. Control algorithm of the proposed triple-loop: (a) flow chart, (b) conceptual transient waveform, and (c) discrete-time model of the TRC and ART loops in the triple-loop WPT system.

Once V_{REC} is within V_{RUT} - V_{RLT}, the power loop is disabled and TRC loop is enabled to find the optimal resonant capacitance for the L_2C_2-tank. The control algorithm in the Tx MCU increases V_{VAR} to decrease C_{Tx} in Fig. 2.2 until V_{REC} starts decreasing. Then it decreases V_{VAR} and monitors V_{REC} until C_{Tx} passes the optimal resonance value, at which point V_{REC} starts decreasing again, and the MCU switches the direction of V_{VAR} variations. This up/down cycle ensures that C_{Tx} wiggles around its optimal value, while responding to the environmental inputs. Considering 256 steps in the 8-bit DAC and the varactor used in this prototype (SMV 1265), there is a 70 fF capacitance change across the L_2C_2-tank for every step. The high resolution varactor-based TRC design prevents sudden voltage variations across L_2 without adding the bulk of an 8-bit capacitor bank.

If V_{REC} exits V_{RUT} - V_{RLT} window during TRC operation, the TRC loop is immediately paused and the power loop is enabled to return V_{REC} back to the designated range. The TRC loop is then activated again to tune C_{Tx} at the new PA output power. The TRC loop may also time-out after 0.33 s by the Rx MCU internal timer, which activates the ART loop to fine-tune C_{ART} on the Rx side.

The ART loop operates based on a 26 kHz clock, extracted in the PMIC from the 13.56 MHz power carrier. A 10-bit capacitor bank, C_{ART}, is swept across L_4C_4-tank in both directions to fine tune the L_4C_4-tank every 0.33 s by maximizing the received power carrier envelope (V_{ENV}). In steady state, V_{ENV} reaches its maximum level and wiggles around it with a 100 mV ripple. The ART loop finds the optimal C_{ART} in less than 3 ms if it only utilizes the 5-bit on-chip capacitors. Since the ART loop operates much faster than the TRC and power control loops, it is enabled only for ~4 ms every 0.33 s. Back telemetry is disabled during the ART operation to prevent erronious RFID readings on the Tx side.

Fig. 2.3b shows an exemplar operation of the sequential control algorithm in Fig. 2.3a and the resulting key transient waveforms. During T_1 start-up period, PA output power increases until V_{REC} is enough to initiate back telemetry data. Once V_{REC} reaches the designated window, shown with horizontal dashed lines, the power loop is deactivated and the TRC loop starts to adjust C_{VAR} to find max(V_{REC}) for the given PA output power at the end of T_1. The ART loop starts after T_2 = 0.33 s is timed-out and continues periodically for T_3 = 4 ms, while back telemetry is disabled. During T_3, V_{REC} is increased by the ART loop while the Rx L_4C_4-tank is fine-tuned and may exceed the upper threshold, as shown in Fig. 2.3b. If this occurs, during T_4 the power control loop decreases the PA output power to return V_{REC} back to the designated range, V_{RUT} - $V_{RLT.}$

If there is a sudden change in the coils' coupling, e.g. k_{23} reduction in Fig. 2.2, or a sudden increment in the Rx power consumption at the end of T_4, which is identified by a vertical dashed line in Fig. 2.3b, V_{REC} will drop below V_{RLT} and the power loop

immediately reacts by increasing VDD_PA during T_5. During T_6, the TRC loop pushes V_{REC} beyond the upper threshold, which results the power loop activation during T_7 to reduce the PA output power. Following the same routine, the TRC and ART loops alternate during T_8, T_9, and beyond, respectively, to maximize the PTE, keep V_{REC} within V_{RUT} - V_{RLT}, and tune the Tx and Rx resonant tanks at f_p.

According to the control algorithm in Fig. 2.3a, the three loops operate at different time periods to maintain the triple-loop system stability as long as each individual loop is stable. The requirements for the stability of the global power loop have already been studied and presented in the previous work [37]. In this implementation, we have chosen the power update frequency to be 300 Hz, resulting in a settling time of 500 ms.

The discrete-time model of the TRC and ART loops is shown in Fig. 2.3c. The TRC loop is divided into four key building blocks; 1) back telemetry (BT) circuit, 2) control unit including the DAC, 3) the RFID class-D PA and inductive link, and 4) the resistive-capacitive (R_LC) load following the rectifier circuit in the Rx. The desired reference voltage, V_{REF}, is the system input and the Rx rectifier voltage, V_{REC}, is the system output. The BT circuit is modeled by an adder followed by a sign block, which compares V_{REC} and V_{REF} to generate an increment "+1" or decrement "-1" command for the class-D PA output power. A sampler with a comparator, which is designed to have a 100 mV offset constitutes the sign block.

The control units for the TRC and ART loops are modeled by the integrators with gains K_{I_Tx} and K_{I_Rx}, respectively. In the TRC loop, the control unit either increases or decreases the varactor voltage, V_{VAR}, using the Tx DAC, based on the BT data. Therefore, K_{I_Tx} is determined by the capacitance variation of the varactor, ΔC_V, for a least significant bit (LSB) change in the DAC output. In the ART loop, the resolution of the capacitor bank across L_4C_4-tank determines K_{I_Rx}. The gain factors, K_{E_Tx} and K_{E1_Rx}, are determined by the ratio of the average current variation delivered to the RC load (ΔI_r) caused by a change in VDD_PA, following ΔC_V and ΔC_{ART} changes in the TRC and ART

loops, respectively. The TRC loop tracks V_{REC} via the BT circuit. In the ART loop, the sampler tracks the envelope voltage across L_4C_4-tank, V_{ENV}, through an envelope detector and resistive divider in the PMIC ASIC, which are modeled by another gain factor, K_{E2_Rx}.

The capacitive and resistive components of the rectifier load current, I_c[n] and I_{RL}[n], are given by,

$$I_C[n] = \frac{q[n] - q[n-1]}{T} = \frac{C(V_{REC}[n] - V_{REC}[n-1])}{T}$$

$$I_{RL}[n] = \frac{V_{REC}[n]}{R_L} \tag{2.1}$$

where T is the loop sampling period, which has significantly different values in the TRC (T_{TRC} = 3.3 ms) and ART (T_{ART} = 77 μs) loops, depending on the controller time base and other component values. V_{REC}[n] is the rectifier voltage at time $t = nT$, and q is the total charge stored in the rectifier capacitor. The impedance of the rectifier RC load, $G(z)$, in the z domain can be defined as

$$G(z) = \frac{V_{REC}(z)}{I_r(z)} = \frac{R_L}{1 + \frac{R_L C}{T} - \frac{R_L C}{T} z^{-1}} \ . \tag{2.2}$$

Since the discrete-time model for the TRC and ART loops is non-linear due to the presence of sign and offset comparator blocks, the system response was verified using Simulink (MathWorks, Natick, MA). The transient step responses of these loops to V_{REF} variation from V_{RLT} = 3.6 V to V_{RUT} = 4.2 V are shown in Fig. 2.3c. When V_{REC} is out of this window, the power loop regulates V_{REC} to return within these boundaries. It can be seen that each loop follows the step response and fluctuates within a narrow voltage range. In the TRC loop, the 103 mV fluctuation is defined by the resolution of the ADC and DAC in the Rx MCU and TRC loop, respectively. In the ART loop, the 28 mV fluctuation depends on the comparator offset in the PMIC ASIC. T_{TRC} and T_{ART} also affect the settling time and voltage range. When T_{TRC} and T_{ART} decrease, the voltage fluctuations and settling time also decrease. The settling times of the TRC and ART loops for the

above step response, were 360 ms and 20 ms, respectively. These are the maximum settling times for the worst-case disturbance of the TRC and ART loops.

2.1.4 Power Management ASIC for Triple-Loop System

Fig. 2.4 shows the block diagram of the PMIC ASIC compatible with the proposed triple-loop system, which includes an active rectifier, a 3.3 V low dropout (LDO) regulator, the ART circuitry, and the LSK circuitry for back telemetry.

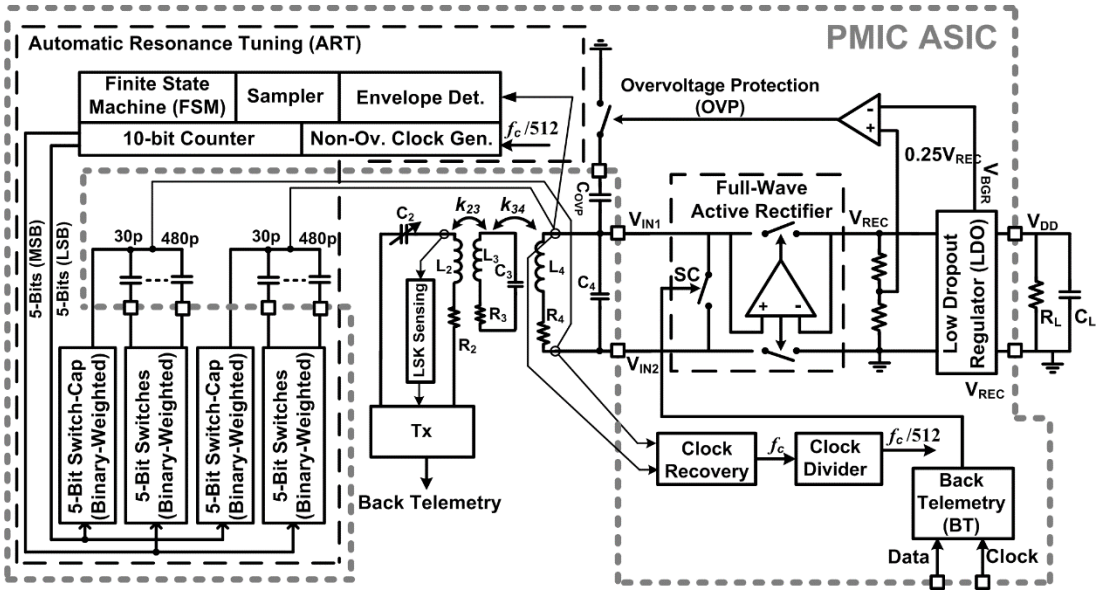

Fig. 2.4. Block diagram of the efficient and adaptive PMIC ASIC, developed specifically for inductively-powered devices operating at 13.56 MHz. The AC carrier is rectified by a full-wave active rectifier followed by an LDO to provide a constant 3.3 V supply. The ART block sweeps 0-480 pF across L_4C_4-tank with 0.5 pF resolution to find the optimal capacitance to resonate with L_4 at 13.56 MHz in the presence of varying parasitic capacitance.

A full-wave rectifier is consisting of PMOS and NMOS pass transistors, which are driven by two high-speed offset-controlled comparators to operate at 13.56 MHz [81]. The ART sweeps two 5-bit binary-weighted on-chip (1 pF, 2 pF, 4 pF, 8 pF, 16 pF) and off-chip (30 pF, 60 pF, 120 pF, 240 pF, 480 pF) capacitor banks resulting in a wide (0-480pF) capacitance tuning change across L_4 with 0.5 pF resolution. There is also an over-voltage protection (OVP) hysteresis comparator that detunes the L_4C_4-tank by the off-

chip C_{ovp} = 100 nF when V_{REC} > 4.8 V to protect the PMIC input when the coupling is too strong or loading is light (large R_L).

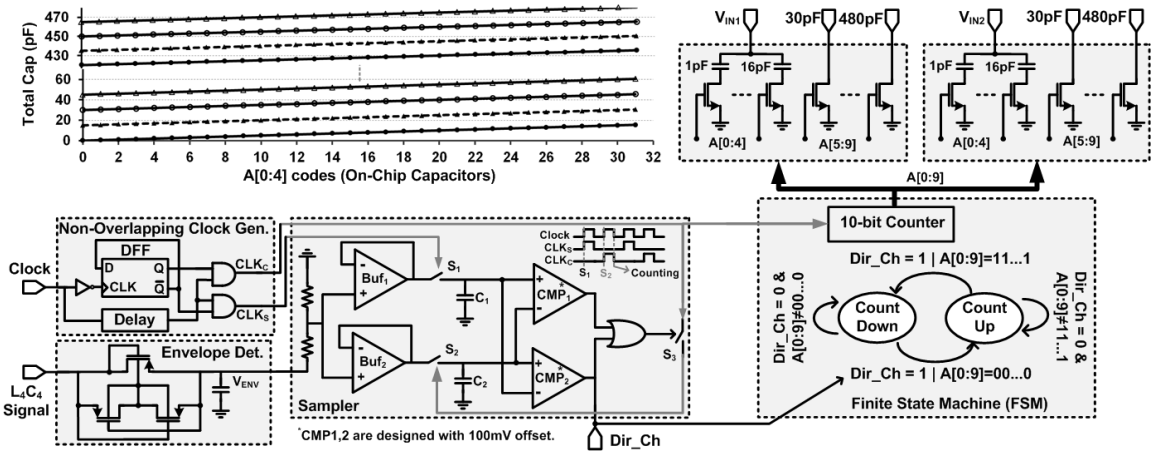

Fig. 2.5. Schematic diagram for the automatic resonance tuning (ART) circuit blocks in the PMIC ASIC.

The ART sweeps two identical 10-bit capacitor banks, which are connected to a 10-bit counter, in one direction (up or down) until the voltage envelope across L_4C_4-tank, V_{ENV}, reduces by 100 mV, as shown in Fig. 2.5. Then the sweeping direction changes until V_{ENV} again drops by 100 mV. This up/down cycle ensures that the L_4C_4-tank is always tuned at f_p = 13.56 MHz with a small offset. V_{ENV} is first detected by a passive rectifier, divided by 1.4, and buffered before being sampled. Two non- overlapping clocks, CLK_C and CLK_S, are generated from the $f_p/512$ = 26.4 kHz signal that results from the clock recovery and divider blocks in Fig. 2.4. The first sampler, S_1, always samples V_{ENV} at the rising edge of CLK_S while S_2 only samples V_{ENV} at the rising edge of CLK_C when V_{ENV} increases or decreases by 100 mV. $CMP_{1,2}$, which are 100 mV offset comparators, close S_3 when the difference between C_1 and C_2 voltages is ±100 mV. When the offset voltage of the comparator decreases, the fluctuation voltage reduces. However, the system becomes more sensitive to external perturbations.

When V_{ENV} drops by 100 mV, CMP_2 output, which is labeled Dir_Ch in Fig. 2.5, changes the direction of the counter according to a finite state machine (FSM). The FSM starts the counter from the middle of the capacitor banks, 240 pF across the L_4C_4-tank,

when the PMIC is powered up. The counter operates at the falling edge of CLK_C to be time-shifted from V_{ENV} samplings at the rising edges. The back telemetry circuit creates ~250 ns pulses, when data is "1" to short the L_4C_4-tank by closing the SC switches in the rectifier. An RC delay cell is used to generate the 250 ns delay. The data and clock signals are generated by the Rx-MCU, as shown in Fig. 2.2.

2.1.5 Measurement Results

Fig. 2.6 shows the measurement setup of the proposed triple- loop system and the PMIC die photo. The PMIC ASIC was fabricated in the TSMC 0.35-μm 4M2P standard CMOS process, occupying 2.54 mm^2 of silicon area. Printed spiral coils (PSC) were used for the primary (L_2) and load (L_4) coils, while a high-Q wire-wound coil (WWC) was used for the secondary coil (L_3) to maximize the 3-coil link PTE. The 3-coil link was designed based on the optimization procedure in [22] with the link specifications summarized in Table 2.1. The maximum output power of the RFID reader is 200 mW, which was enough to transfer ~10 mW to the Rx at d_{23} = 2 cm nominal coupling distance. In this prototype, we chose a 3-coil link to perform impedance modulation on the Rx using an extra coil. Because we are using a class-C power amplifier with its LC-network matching circuit, there is no need for an additional coil on the Tx side [22].

TABLE 2.1. THREE-COIL INDUCTIVE LINK SPECIFICATIONS

Parameters	Measured Value
Printed-spiral primary coil (L_2)	Inductance = 361 nH Outer diameter = 2.8 cm Line width = 10 mm Number of turns = 4 Q_2 = 86.1
Wire-wound secondary coil (L_3)	Inductance = 729 nH Outer diameter = 3.4 cm Wire diameter = 0.64 mm Number of turns = 3 Q_3 = 181.0
Printed-spiral load coil (L_4)	Inductance = 607 nH Outer diameter = 3.4 cm Line width = 1 mm Number of turns = 3 Q_4 = 50.1
L_2-L_3 nominal distance	20 mm
L_3-L_4 separation	3 mm
Coupling coefficients	k_{23} = 0.081, k_{24} = 0.049, k_{34} = 0.459
Nominal load (R_L)	500 Ω
Operation frequency	13.56 MHz

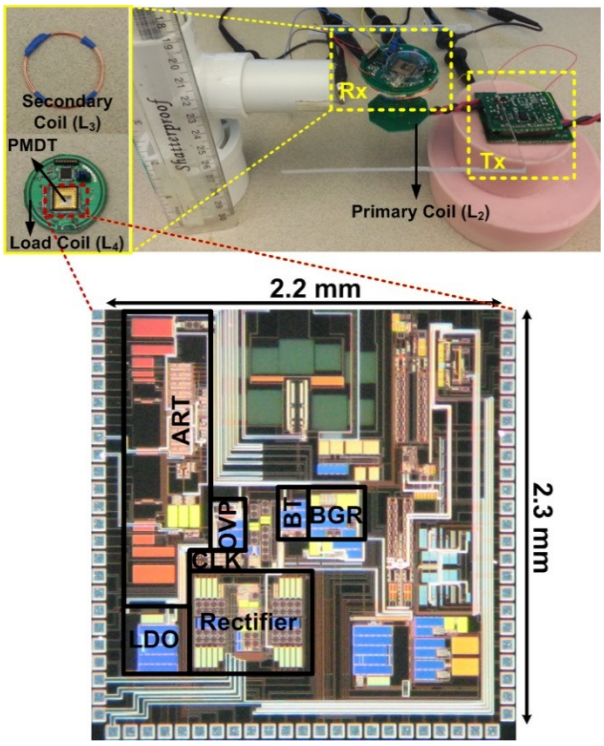

Fig. 2.6. Triple-loop wireless power transmission measurement setup and die micrograph of the PMIC chip, occupying 2.2 × 2.3 mm^2 silicon area.

Fig. 2.7 shows the measured transient waveforms for the current triple-loop prototype in Fig. 2.6 and control algorithm in Fig. 2.3a. In Fig. 2.7a, the Rx coils were

suddenly moved from d_{23} = 2.1 cm to 2.9 cm and back to 2.0 cm away from the Tx coil. d_{23}, which was extracted from the recorded video during coil movements, is shown on the top of Fig. 2.7a. It can be seen that the power control loop responds to the Rx movements within ~50 ms by decreasing VDD_PA (1st trace on the 2nd panel in Fig. 2.7a) when d_{23} drops because V_{REC} (3rd trace) is increased above V_{RUT} = 4.2 V. Similarly, VDD_PA increases when Rx returns to its original location and V_{REC} drops below V_{RLT} = 3.6 V.

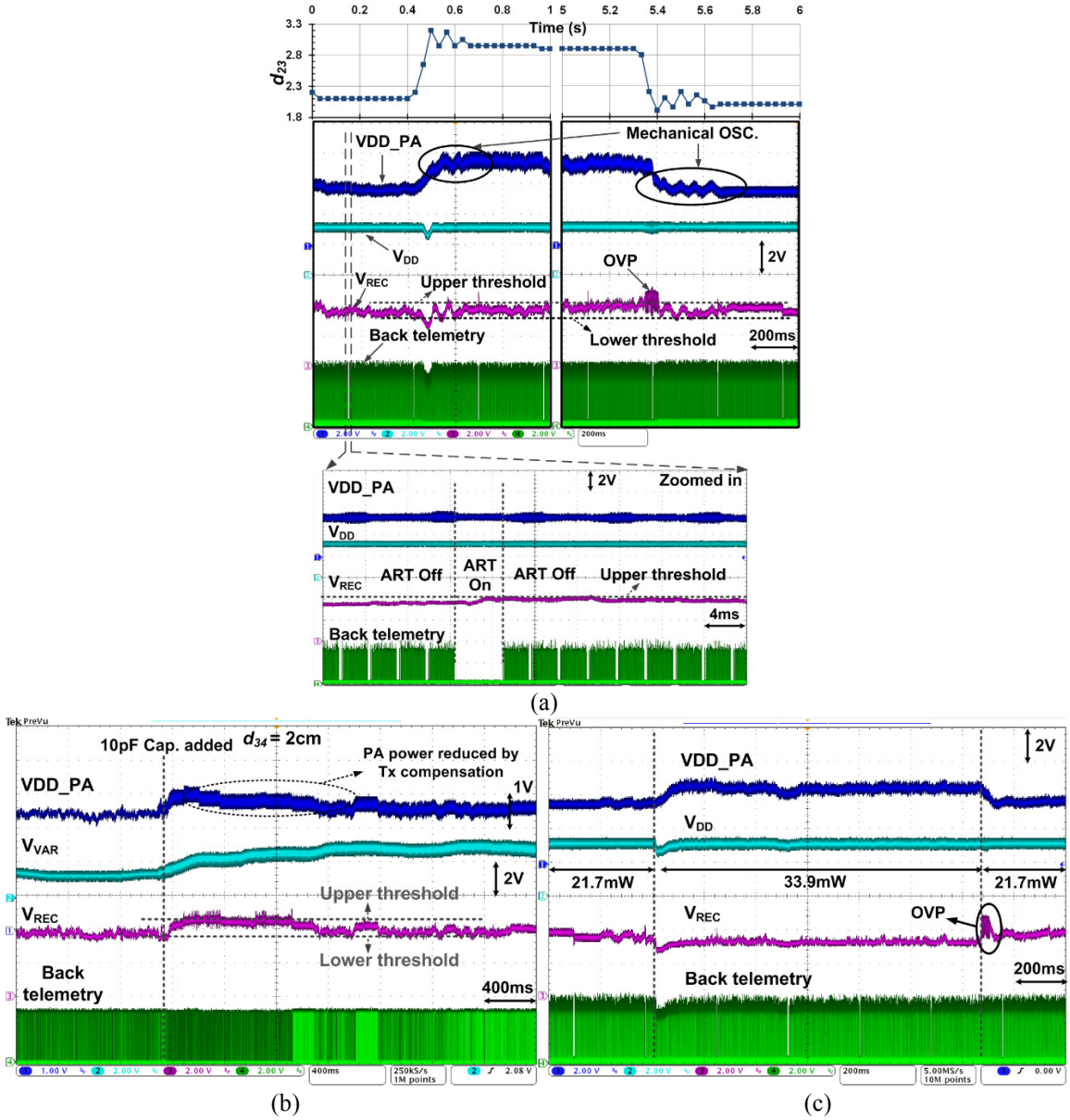

Fig. 2.7. Triple-loop power transmission system measured waveforms: (a) disturbed by 0.9 cm coil distance (b) adding 10 pF capacitive disturbance (c) transient load variation from 21.7 mW to 33.9 mW.

During this test, V_{REC} information was fed back to the Tx via back telemetry every 3.3 ms, as shown in the 4th trace on the 2nd panel in Fig. 2.7a. Overall, the power loop successfully opposed the coils' coupling variations and maintained V_{REC} and V_{DD} within their designated range. Also note that when d_{23} suddenly drops in Fig. 2.7a, the OVP circuit kicks in for a brief period to protect the PMIC input from the large voltage transient across L_4. During the power loop operation, the Rx ART was enabled every 0.33 s for ~ 4 ms to find the Rx resonant capacitor, as shown in the zoomed inset at the bottom of Fig. 11a. In this measurement, as expected, V_{REC} was increased when the ART was enabled because of the optimal tuning.

Fig. 2.7b shows the transient response when a 10 pF capacitor was added to L_2 in parallel at the time indicated by a vertical dashed line. V_{REC} has dropped as a result, and the power loop has immediately taken action against this disturbance by increasing VDD_PA. Once V_{REC} was returned within the desired window, the TRC loop was activated to compensate for this Tx parasitic capacitance change by elevating V_{VAR} to lower C_{Tx}. Similar to Fig. 2.7a, the ART loop was also periodically enabled to find the optimal resonance capacitance for the L_4C_4-tank. Since ART had already found the optimal resonance condition in the earlier periods (no disturbance on the Rx side), V_{REC} was not changed significantly by the ART operation. Thanks to the TRC loop, VDD_PA returned back to its original value (~3.5 V) before adding the parasitic capacitance, because L_2 was re-tuned at 13.56 MHz and the same amount of power was being delivered to the Rx with the same VDD_PA. The transient response in Fig. 2.7c shows how V_{REC} and V_{DD} drop by a sudden increase in the Rx loading from 21.7 mW to 33.9 mW. VDD_PA is immediately increased by the power control loop to compensate for the higher power demand. Once the load current returns back to 21.7 mW, the OVP circuit kicks in to protect the PMIC ASIC when $V_{REC} > 4.8$ V, similar to Fig. 2.7a, while all voltages return back to their original values.

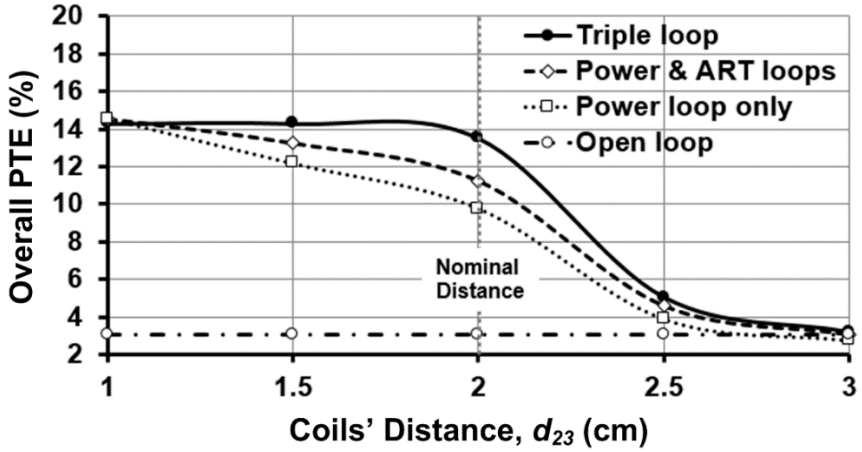

Fig. 2.8. Measured overall PTE vs. the coil's distance in the open-loop, power control loop only, power and ART dual-loop, and the triple-loop conditions when environmental effects were emulated by detuning the Tx and Rx coils with 8.3 pF and 14.4 pF capacitors, respectively.

Fig. 2.8 compares the measured PTE, which is defined as the overall efficiency from the power supply in Tx to the load in Rx, vs. d_{23} from 1 cm to 3 cm in the open-loop, power control loop only, power and ART dual-loops, and the triple-loop conditions when the environmental effects were emulated by detuning the Tx and Rx coils with 8.3 pF and 14.4 pF capacitors, respectively. In the mono-, dual-, and triple-loop measurements, we have included the power dissipation of all the additional circuits in the overall PTE. Because open-loop system should operate at the worse-case conditions to remain operational, i.e. d_{23} = 3 cm and VDD_PA = 5.5 V, the open-loop PTE remains low at shorter coil distances. However, the power loop dynamically reduces the Tx power at short distances to the level that is just enough to operate the Rx circuitry, thus significantly improving the PTE from 3% to 9.8% (6.8% improvement) at the nominal distance of d_{23} = 2 cm, as shown by a vertical dashed line in Fig. 2.8.

The PTE improvements due to the proposed ART and TRC loops highly depend on the amount of detuning in the Tx and Rx LC-tanks due to environmental effects or deformations. In the exemplar test setup of Fig. 2.6, when 8.3 pF and 14.4 pF detuning capacitors were added to the Tx and Rx tank circuits, respectively, the PTE was improved for an additional 1.4% and 2.3% compared to the power-loop alone in Fig. 2.8 when the

ART and TRC loops were activated, respectively. Table 2.2 compares this work with the most recent open- and closed-loop wireless power transmission systems in the literature in terms of the techniques used to improve the PTE although the absolute value of the PTE is dependent on multiple parameters related to the design and application of an inductive link. This work is the first to demonstrate the dynamic operation of all three loops along with a simple but stable control strategy in a prototype system [82].

TABLE 2.2. BENCHMARKING OF WIRELESS POWER TRANSMISSION SYSTEM

Publication		2008 [33]	2009 [31]	2005 [36]	2009 [34]	2011 [35]	2010 [37]	2012 [39]	2013 [32]	**This work**
Power carrier frequency*		75 kHz	915 MHz	1 MHz	1 MHz	7.65 MHz	13.56 MHz	6.47 MHz	13.8 MHz	**13.56 MHz**
Coil configuration		2 coil	2 coil	2 coil	2 coil	4 coil	2 coil	2 coil	2 coil	**3 coil**
Closed-loop control		No	No	Yes	No	No	Yes	Yes	Yes	**Yes**
Adaptive Rx Tuning (ART)		No	Yes	No	No	No	No	No	Yes	**Yes**
TRC	Adaptive carrier frequency	Yes	No	No	Yes	Yes	No	Yes	No	**No**
	Adaptive matching circuit	No	Yes	No	No	No	No	No	No	**Yes**
Tx/Rx data communication		Far field	N/A	LSK	N/A	N/A	LSK	Far field	LSK /Optical	**LSK**
Power Transfer Efficiency (%)		80	**0.056	36.3	~18	50	6.9	75	N/A	**13.5**
Distance (mm)		10	15	15	50	700	10	600	N/A	**20**
Tx/Rx coil diameter (mm)		N/A	20/2	40/32	100/100	590/590	20/10	390/390	N/A	**28/34**
Potential application		IMD	IMD	IMD	N/A	N/A	IMD	Electronic appliances	IMD	**IMD**

* Center frequency of the tuning range
** Calculated value

2.2 A Multi-Cycle Q-Modulation for Dynamic Optimization of Inductive Link

This chapter introduces a new method, called multi-cycle Q-modulation, which can be used in wireless power transmission (WPT) to modulate the quality factor (Q) of the receiver (Rx) coil and dynamically optimize the load impedance to maximize the power transfer efficiency (PTE) in two-coil links. A key advantage of the proposed method is that it can be easily implemented using off-the-shelf components without requiring fast switching at or above the carrier frequency, which is more suitable for integrated circuit design. Moreover, the proposed technique does not need any sophisticated synchronization between the power carrier and Q-modulation switching pulses. The multi-cycle Q-modulation is analyzed theoretically by a lumped circuit model, and verified in simulation and measurement using an off-the-shelf prototype. Automatic resonance tuning (ART) in the Rx, combined with multi-cycle Q-modulation helped maximizing PTE of the inductive link dynamically in the presence of environmental and loading variations, which can otherwise significantly degrade the PTE in multi-coil settings.

2.2.1 System Overview

The proposed multi-cycle Q-modulation with automatic resonance tuning (ART) is shown in Fig. 2.9, for the first time, in a prototype utilizing COTS components, such as a rectifier, regulator, analog switch, capacitor bank, and microcontroller (MCU). The series Rx LC-tank is composed of L_3 and $C_3+\Delta C_{ART}$ with its parasitic resistance, R_3, and it is assumed that the Rx LC-tank is always resonant at f_p because ΔC_{ART} is adaptively adjusted to maintain the resonant condition via ART operation. The power amplifier (PA) can be modeled with a sinusoidal voltage source, V_S, plus its output impedance, R_S. The Tx LC-tank is composed of L_2, C_2, and the series resistance, R_2. The mutual inductance, M_{23}, is decided by the coupling coefficient, k_{23}, and the Tx and Rx coil inductances, L_2

and L_3. We have also derived the governing equations over the new multi-cycle Q-modulation technique using a lumped circuit model, and verified them via simulation and measurements. The ART combined with multi-cycle Q-modulation keeps the PTE of the inductive link at its peak dynamically by simultaneously matching the load and tuning the Rx LC-tank at the carrier frequency, f_p.

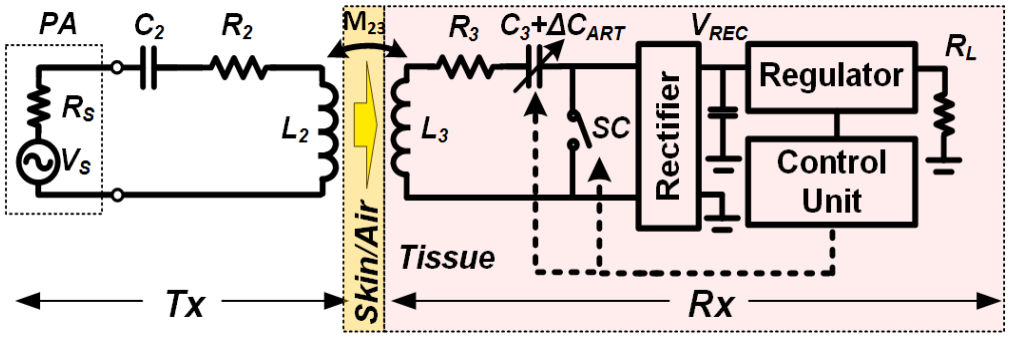

Fig. 2.9. Block diagram of a multi-cycle Q-modulation with automatic resonance tuning (ART), which adaptively transforms any arbitrary load to the optimal loading and tunes the Rx LC-tank at the carrier frequency for continuous operation at the highest PTE.

2.2.2 Modeling and Analysis of Multi-Cycle Q-Modulation

Fig. 2.10a shows a lumped model of the proposed multi-cycle Q-modulation inductive link along with its switching waveforms in Fig. 2.10b. The parasitic components are not considered in the lumped model of the proposed Q-modulation inductive link in Fig. 2.10 to avoid the complex analysis. In the conventional 2-coil inductive link, the PTE can be derived as [22],

$$\eta_{2-coil} = \frac{k_{23}^2 Q_2 Q_{3L}}{1 + k_{23}^2 Q_2 Q_{3L}} \cdot \frac{Q_{3L}}{Q_L}, \tag{2.3}$$

where $k_{23} = M_{23}/(L_2L_3)^{0.5}$, $Q_2 = \omega L_2/R_2$, and $Q_{3L} = Q_3Q_L/(Q_3+Q_L)$, in which $\omega=2\pi f_p$, $Q_3 = \omega L_3/R_3$ and $Q_L = R_L/\omega L_3$. The high quality factors of Q_2, Q_3, and Q_{3L} are desirable to achieve high PTE in a 2-coil inductive link. During coil optimization, Q_2 and Q_3 are decided by their geometrical limitation and carrier frequency, and Q_{3L} is limited by the load resistance. The Q-modulation technique proposed in this section modulates the

loaded Q-factor, Q_{3L}, in the Rx coil by the switched L_3C_3-tank to transform R_L into optimal equivalent load, R_{opt}, for optimization of the 2-coil inductive link. Two control parameters are employed to achieve the highest PTE in the multi-cycle Q-modulation technique: 1) the switching time, T_{on}, and 2) the switching period, T_{np}, both of which are multiple times longer than the carrier period, $T_p = 1/f_p$. The SC signal closes or opens a switch with its ON resistance of R_{SW} to modulate the load, R_L, and maximize the voltage across the load, V_L, and consequently the received power.

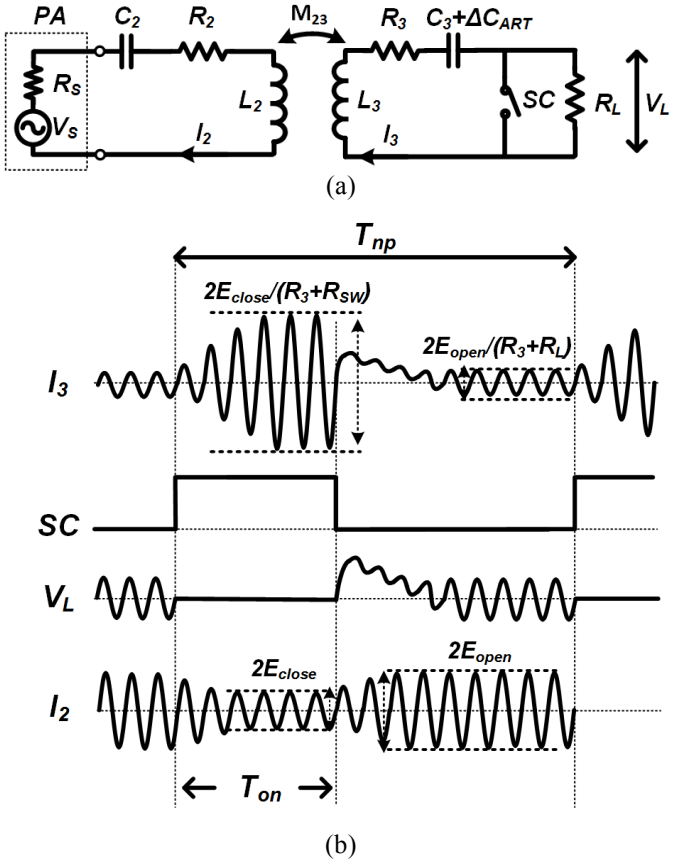

Fig. 2. 10. (a) The circuit model of the proposed multi-cycle Q-modulation with ART inductive link. (b) Voltage and current waveforms, controlled by T_{on} and T_{np}.

The equivalent circuit of Fig. 2.10a is shown in Fig. 2.11a, in which $\omega = 2\pi f_p$, $R_{22} = R_S + R_2$, $V_S(t)=E_0\cos(\omega t)$, and $C_3' = C_3 + \Delta C_{ART}$. The equivalent resistance, R_{33}, is $R_3 + R_{SW}$ for $0 \le t < T_{on}$, and R_3+R_L for $T_{on} \le t < T_{np}$, where R_{SW} is the ON resistance of the SC switch ($R_{SW} << R_L$). V_{23} and V_{32} in the equivalent circuit can be found from,

$$V_{23} = -jwM_{23}I_3, \tag{2.4}$$

$$V_{32} = jwM_{23}I_2. \tag{2.5}$$

The reflected impedance onto the primary side, Z_{ref}, can be derived from,

$$Z_{ref} = \frac{V_{23}}{I_2} = \frac{(wM_{23})^2}{jwL_3 + \frac{1}{jwC_3} + R_{33}}. \tag{2.6}$$

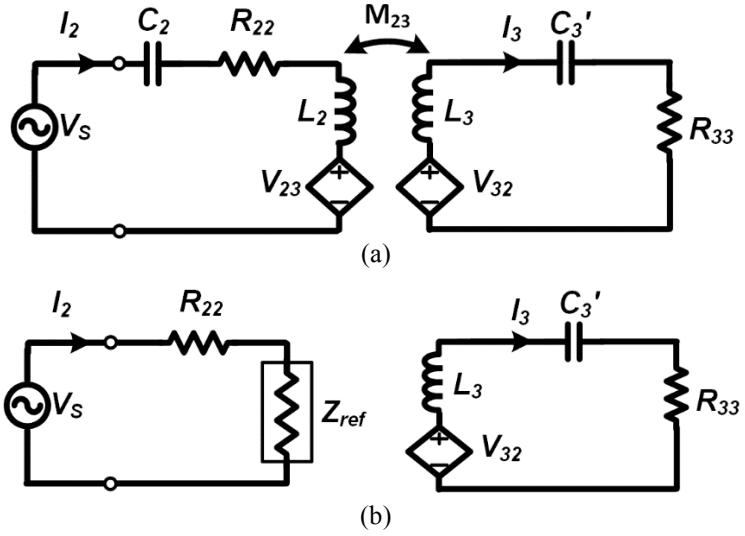

Fig. 2.11 (a) Equivalent circuit of lumped model in Fig. 2a. (b) Simplified equivalent circuit seen from the primary (Tx) side at resonance. The secondary (Rx) side is maintained because of its effect on the transient mode calculations.

Assuming that L_2 and C_2 on the primary (Tx) side are tuned at f_p, the equivalent circuit seen from the primary and secondary sides can be simplified to what is shown in Fig. 2.11b. When L_3C_3-tank is also tuned at f_p, the primary current, I_2, and the secondary reflected voltage, V_{32}, in the steady-state condition can be calculated as,

$$I_2 = \frac{V_S}{R_{22} + \frac{w^2 M_{23}^{\ 2}}{R_{33}}}, \tag{2.7}$$

$$V_{32} = \frac{jwM_{23}V_S}{R_{22} + \frac{w^2 M_{23}^{\ 2}}{R_{33}}}. \tag{2.8}$$

Therefore, the steady-state current in the Rx, I_3(t), can be derived by Kirchhoff's voltage law (KVL),

$$V_{32}(t) = L_3 \frac{dI_3(t)}{dt} + \frac{1}{C_3'} \int_0^t I_3(\tau) d\tau + I_3(t) \cdot R_{33} = E_1 \sin(wt), \quad (2.9)$$

$$E_1 = \frac{wM_{23}E_0}{R_{22} + \frac{w^2 M_{23}^2}{R_{33}}}. \quad (2.10)$$

Since R_{33} is either R_3+R_{SW} or R_3+R_L during Q-modulation, we substitute E_1 with E_{close} and E_{open}, which imply the steady-state amplitudes of $I_2(t)$ for $0 \le t < T_{on}$ and $T_{on} \le t < T_{np}$, respectively. When SC is closed, the Rx circuit would be underdamped due to its small parasitic resistance and (2.9) can be solved by summing the particular integral (2.11) and the complementary function (2.12),

$$I_{3P,close}(t) = \frac{E_{close}}{R_3 + R_{SW}} \sin(wt), \quad (2.11)$$

$$I_{3C,close}(t) = e^{-\alpha t}(A_1 \cos(wt) + A_2 \sin(wt)), \quad (2.12)$$

$$I_{3,close}(t) = I_{3C,close}(t) + I_{3P,close}(t), \quad (2.13)$$

where $\alpha = (R_3+R_{SW})/2L_3$. Considering the initial condition from $t = 0^-$, where SC is opened, the secondary steady-state current during $0 \le t < T_{on}$ can be found from,

$$I_{3,close}(t) = \left[\frac{E_{close}}{R_3 + R_{SW}}(1 - e^{-\alpha t}) + \frac{E_{open}}{R_3 + R_L} e^{-\alpha t} \right] \sin(wt). \quad (2.14)$$

When SC is open at $t = T_{on}^+$, the energy stored in the L_3C_3-tank is transferred to R_L. Since the load has a relatively large resistance compared to R_{SW}, the circuit condition is normally over-damped and the solution for (2.9) takes the form of,

$$I_{3,open}(t) = B_1 e^{s_1(t-T_{on})} + B_2 e^{s_2(t-T_{on})} + \frac{E_{open}}{R_3 + R_L} \sin(w(t - T_{on})) \quad (2.15)$$

where,

$$s_{1,2} = \frac{-(R_3 + R_L)}{2L_3} \pm \sqrt{\left\{\frac{(R_3 + R_L)}{2L_3}\right\}^2 - \frac{1}{L_3 C_3'}}, \tag{2.16}$$

$$B_1 = \frac{-V_C(T_{on}^-)}{L_3(s_1 - s_2)} + \frac{s_1 \times I_{3.close}(T_{on}^-)}{s_1 - s_2}, \tag{2.17}$$

$$B_2 = \frac{V_C(T_{on}^-)}{L_3(s_1 - s_2)} - \frac{s_2 \times I_{3.close}(T_{on}^-)}{s_1 - s_2}. \tag{2.18}$$

The two initial conditions, $I_{3,close}(T_{on}^-) = 0$ and $V_C(T_{on}^-)$, which is the voltage across C_3' at $t = T_{on}^-$, that are needed to solve (2.15) can be iteratively calculated from (2.14) by utilizing the new initial condition from (2.15) in the transient state.

Although the transient waveforms of $I_{3,close}(t)$ and $I_{3,open}(t)$ can be derived from (2.13) and (2.15), the transient voltages reflected onto the secondary side, $E_{close}(t)$ and $E_{open}(t)$, are also affected by the LCR components on both primary and secondary sides while both L_2C_2- and L_3C_3-tanks are tuned at f_P. It is necessary to solve the overall transient equation derived from Fig. 2.11a to extract the exact waveforms for $E_{close}(t)$ and $E_{open}(t)$,

$$M_{23}\frac{dI_2(t)}{dt} = L_3\frac{dI_3(t)}{dt} + \frac{1}{C_3'}\int_0^t I_3(\tau)d\tau + I_3(t)\cdot R_{33}, \tag{2.19}$$

$$V_S \sin(wt) = L_2\frac{dI_2(t)}{dt} + \frac{1}{C_2}\int_0^t I_2(\tau)d\tau + I_2(t)\cdot R_{22} + M_{23}\frac{dI_3(t)}{dt}. \tag{2.20}$$

Since (2.19) and (2.20) create a 4th order differential equation, we estimate the transient voltage for $E_{close}(t)$ and $E_{open}(t)$ in this paper, when the overall system is in the over-damped condition,

$$E_{close}(t) = E_{close}(1 - e^{-\alpha t}) + E_{open}\, e^{-\alpha t}, \tag{2.21}$$

$$E_{open}(t) = E_{open}(1 - e^{-\alpha (t - T_{on})}) + E_{close}\, e^{-\alpha (t - T_{on})}, \tag{2.22}$$

where $\alpha = (R_S+R_2)/2L_2$.

Assuming that the Tx and Rx LC-tanks are fully resonated, V_S and I_2 are in-phase because the reflected load in (2.6) has only the real part. The estimated transient voltage for $E_{close}(t)$ and $E_{open}(t)$ are used to calculate V_S output power in the transient state. Since power is only delivered to the load when SC is open, $T_{on} \le t < T_{np}$, the PDL and V_S (source) output power for the multi-cycle Q-modulation can be derived from,

$$P_{L,Q\mathrm{mod},average} = \frac{R_L}{T_{np}} \int_{T_{on}}^{T_{np}} I_{3,open}(t)^2 dt , \tag{2.23}$$

$$P_{Vs,close,rms} = V_{S,rms} \times I_{2,close,rms} = \frac{V_S}{\sqrt{2}} \times \sqrt{\frac{\int_0^{T_{on}} \left[\frac{E_{close}(t)}{wM} \sin(wt) \right]^2 dt}{T_{on}}} , \tag{2.24}$$

$$P_{Vs,open,rms} = V_{S,rms} \times I_{2,open,rms} = \frac{V_S}{\sqrt{2}} \times \sqrt{\frac{\int_{T_{on}}^{T_{np}} \left[\frac{E_{open}(t)}{wM} \sin(wt) \right]^2 dt}{T_{np} - T_{on}}} , \tag{2.25}$$

$$P_{Vs,Q\mathrm{mod},average} = \frac{T_{on} \times P_{Vs,close,rms} + (T_{np} - T_{on}) \times P_{Vs,open,rms}}{T_{np}} , \tag{2.26}$$

where $P_{L,Qmod,average}$ is the PDL, $P_{Vs,close,rms}$ is the power drained from V_S for $0 \le t < T_{on}$, $P_{Vs,open,rms}$ is the power drained from V_S for $T_{on} \le t < T_{np}$, and $P_{Vs,Qmod,average}$ is the average power drained from V_S. Moreover, the PA + link efficiency can be calculated as,

$$\eta_{Qmod}\% = 100 \times P_{L,Qmod,average}/P_{Vs,Qmod,average}. \tag{2.27}$$

The proposed Q-modulation boosted Q_{3L} equal to Q_3 during $t < T_{on}$, and the boosted energy is stored in the Rx LC-tank although the power is not transferred to the load compared to the conventional 2-coil inductive link without the Q-modulation, which transfer the continuous inductive power to the load with relatively low Q_{3L} due to low Q_L. The stored energy in the Rx LC-tank is transferred to the load during T_{np}-T_{on}, to achieve

the modulated loaded quality factor, $Q_{3L,eq}$, which can be found from $Q_{3L,eq} = Q_3Q_{L,eq}/(Q_3+Q_{L,eq})$, where $Q_{L,eq} = \omega L_3/R_{opt}$, and $R_{opt} = (1-T_{on}/T_{np})R_L$.

2.2.3 Verification of Theoretical Model of Multi-Cycle Q-Modulation

The key parameters used in calculation, simulation, and proof-of-concept prototype measurement setup of the multi-cycle Q-modulation method are summarized in the Table 2.3. The carrier frequency was chosen at 13.56 MHz in the industrial-scientific and medical (ISM) band. The Tx planar spiral coil (PSC) and Rx wire-wound coil are designed for a nominal distance of 3 cm and have a measured k_{23} = 0.044. The class-E PA used in the measurement setup had an output impedance of 3.1 Ω, and the switching resistance of the MOSFET pair (DMN5L06K) used for Q-modulation in the prototype Rx was 2 × 2 Ω.

TABLE 2.3. PROTOTYPE MULTI-CYCLE Q-MODULATION INDUCTIVE LINK SPECIFICATIONS

Parameters	Value
PSC primary coil (L_2)	Inductance = 5.8 µH Outer diameter = 4 cm Line width = 0.4 mm Line spacing = 0.2 mm Number of turns = 9 Quality factor = 187
Wire-wound secondary coil (L_3)	Inductance = 3.85 µH Outer diameter = 2.2 cm Wire diameter = 0.2 mm Number of turns = 10 Quality factor = 93.7
Resonance Capacitance	C_2 = 23.8 pF, C_3 = 36.0 pF
L_2-L_3 nominal distance (d_{23})	3 cm
Coupling coefficient (k_{23})	0.044
Switch Resistance (R_{SW})	4 Ω
PA output resistance (R_S)	3.1 Ω
Carrier frequency (f_p)	13.56 MHz
Loading (R_L)	500 Ω

Using Table 2.3 parameters in (2.23)-(2.27), and sweeping T_{on} and T_{np} from 1 to 10 power carrier cycles, result in Fig. 2.12a, which shows how the inductive link PTE changes with multi-cycle Q-modulation. Fig. 2.12a also shows the optimal values for T_{on} and T_{np} that would maximize the PA + link efficiency, η_{Qmod}.

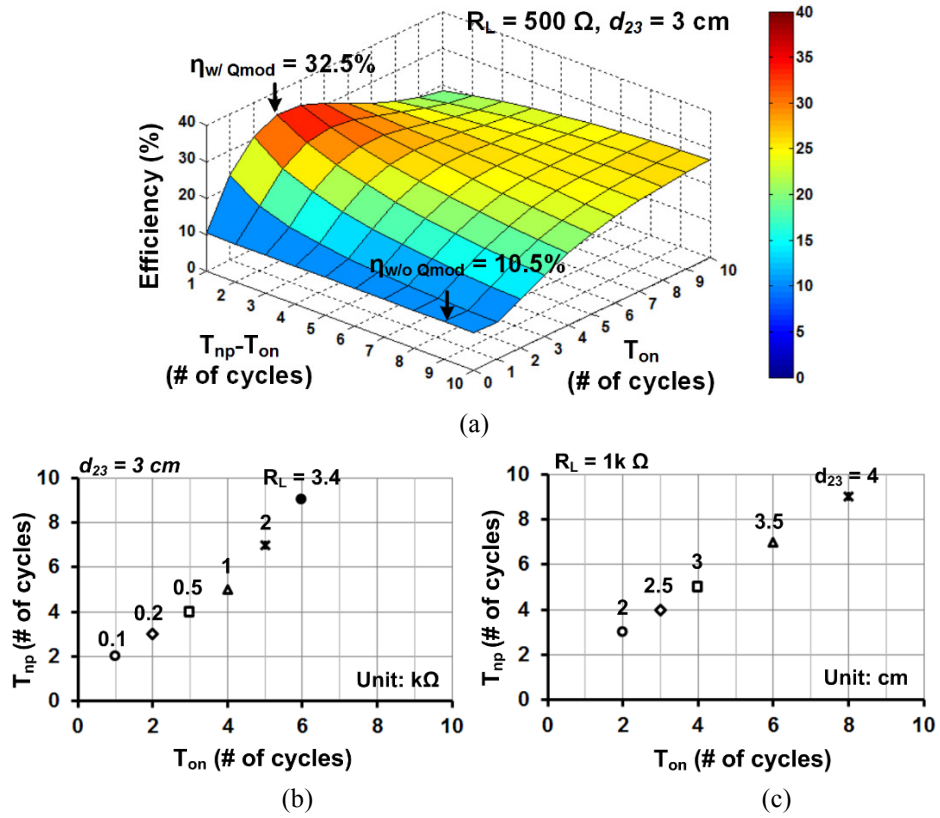

Fig. 2.12. Calculated optimal T_{on} and T_{np} to maximize the PA + link efficiency in 2-coil inductive link using parameters in Table 2.3. (a) $T_{on} = 3T_p$, $T_{np} = 4T_p$ at $R_L = 500\ \Omega$ and $d_{23} = 3$ cm. (b) Optimal T_{on} and T_{np} vs. load variations at $d_{23} = 3$cm. (c) Optimal T_{on} and T_{np} vs. coil distance variations at $R_L = 1\ \text{k}\Omega$.

According to Fig. 2.12a, with $R_L = 500\ \Omega$ and $d_{23} = 3$ cm, the 2-coil inductive link in Table 2.3 provides $\eta_{w/o\ Qmod} = 10.5\%$ at $d_{23} = 3$ cm. Using multi-cycle Q-modulation with $T_{on} = 3T_p$, $T_{np} = 4T_p$, the peak efficiency increases to 32.5%, which represents 182% improvement. Moreover, using the same theoretical analysis in section 2.2.2, we can find how T_{on} and T_{np} should be changed in response to changes in R_L and d_{23}, which are the two parameters that often change during operation of the system. These results, which are shown in Figs. 2.12b and 2.12c, respectively, indicate that more load modulation is necessary to achieve the maximum η_{Qmod} when R_L increases or k_{23} decreases.

To compare the theoretical model in section 2.2.2 with circuit simulation, we used the Simulink (Mathworks, Natick, MA) environment and parameters in Table 2.3. The calculated and simulated transient waveforms, with $T_{on} = 3T_p$, $T_{np} = 4T_p$, $R_L = 500\ \Omega$, and

d_{23} = 3 cm, using (2.14) for closed switch, (2.15) for open switch, and Simulink are presented in Fig. 2.13a, and show a very good agreement. Fig. 2.13b shows the calculated, simulated, and measured PA + link efficiency over a wide range of R_L, from 100 Ω to 3.4 kΩ. Since the inductive link is designed by the series LC-tank, the measurement result shows higher PA + link efficiency for the smaller R_L without the Q-modulation while the efficiency dramatically decreases as R_L increases.

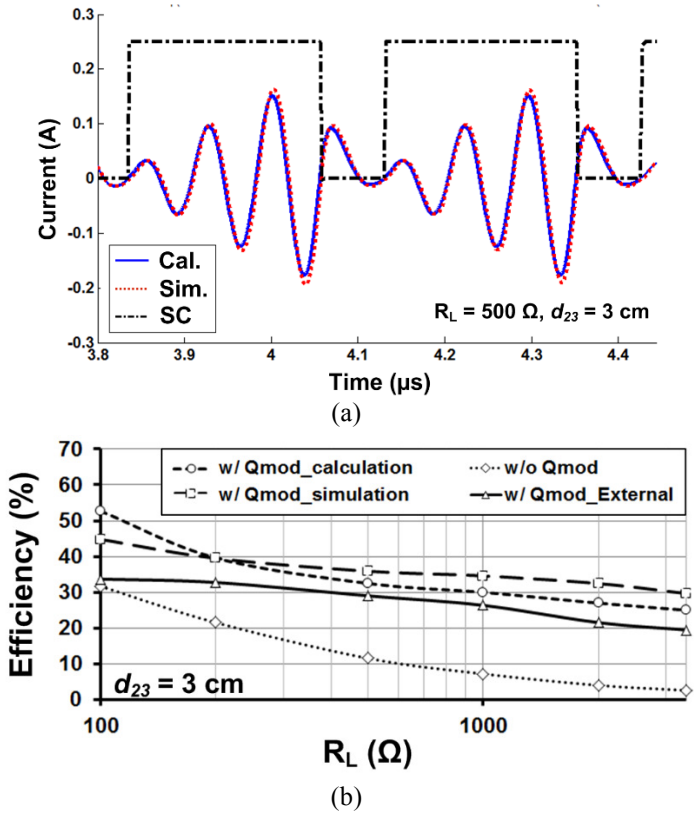

Fig. 2.13. (a) Calculated vs. Simulated transient waveform for $I_3(t)$ at R_L = 500 Ω and d_{23} = 3 cm, and other parameters in Table 2.3. (b) PA + link efficiency vs. loading variations from 100 Ω to 3.4 kΩ with and without multi-cycle Q-modulation.

The external SC pulse (external Q-modulation) generated by the signal generator opens or closes the MOSFET pair in order to verify the effect of the proposed multi-cycle Q-modulation. Because of the approximations in calculating the transient voltage between $E_{close}(t)$ and $E_{open}(t)$ in (2.21) and (2.22) followed by (2.24) and (2.25), the calculated and simulated PA + link efficiencies are not perfectly matched in a wide range of R_L. Parasitic components in the actual circuit further affect the PA + link efficiency by

degrading it in the measurement results with externally applied Q-modulation switching pulse. Nonetheless, the calculated, simulated, and measured efficiencies show similar trends, and the multi-cycle Q-modulation in each case significantly increases η_{Qmod} over a wide range of R_L and k_{23} variations thanks to the dynamic impedance matching capability of the Rx.

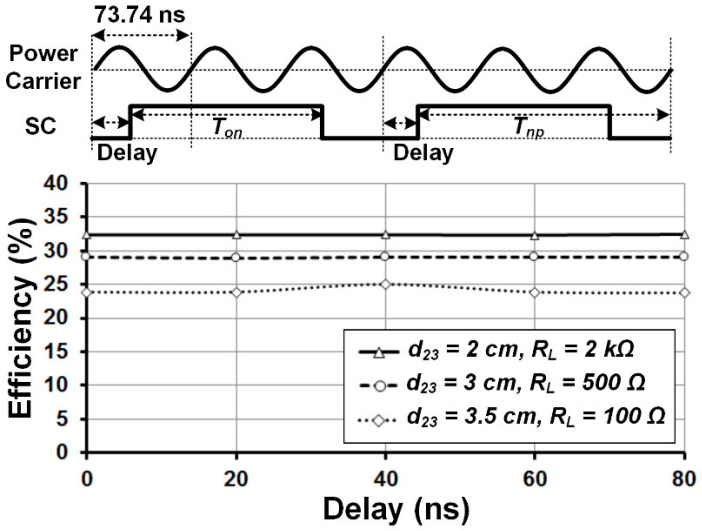

Fig. 2.14. Measured η_{Qmod} for variable delay between the power carrier at 13.56 MHz and the optimal SC pulses for three cases of (d_{23} = 2 cm, R_L = 2 kΩ), (d_{23} = 3 cm and R_L = 500 Ω), and (d_{23} = 3.5 cm, R_L = 100 Ω).

A key advantage of the multi-cycle Q\modulation is that it does not need delicate synchronization between the current in the Rx L_3C_3-tank and the SC pulse, which might be difficult to achieve when the carrier frequency is high. Although we constructed the lumped circuit model and its waveforms in section 2.2.2 based on the synchronized condition between the switching pulse and the power carrier, adding delay to the SC signal does not affect the circuit performance because in the steady state the energy stored in the L_3C_3-tank is independent of the delay of the SC signal, but dependent on T_{on} that spans over multiple periods of T_P. Fig. 2.14 shows the measured η_{Qmod} with fixed T_{on} and variable delays between the power carrier and SC pulse. The optimal SC pulse periods for several R_L and d_{34} combinations are found from Fig. 2.12 and the SC signal

was generated externally with 0 to 80 ns delay with respect to the power carrier (T_P = 73.74 ns). It can be seen that η_{Qmod} is almost independent of the delay of the SC pulse.

2.2.4 Automatic Resonance Tuning in Multi-Cycle Q-Modulation

It is important to ensure that the Tx and Rx LC-tanks are tuned at the carrier frequency, f_p, to achieve the best PTE against changes in the parasitic capacitance of the surrounding environment or various objects around the inductive link. The inductive link in the IMD is often adversely affected by the parasitic capacitance of the surrounding tissue environment, which can significantly degrade the PTE, particularly when the Q-factor is high [34]. Proper tuning of the Rx LC-tank becomes even more important when Q-modulation is employed because of the impact of this technique on boosting the Q of Rx to improve the overall PTE. Moreover, small deviation in C_3 due to Q-modulation results in reduction of the stored energy in L_3C_3-tank, leading to degradation in the PTE more severely than a conventional 2-coil inductive link. Fig. 2.15 shows the simulated η_{Qmod} vs. variations in C_3' for conventional and Q-modulated 2-coil inductive links at R_L = 200 Ω and d_{23} = 3 cm. A 11.4% variation in C_3' results in 7.5% degradation in the η_{Qmod} of the Q-modulated inductive link, while the same change results in only 2% degradation in the $\eta_{w/o\ Qmod}$ of the conventional 2-coil.

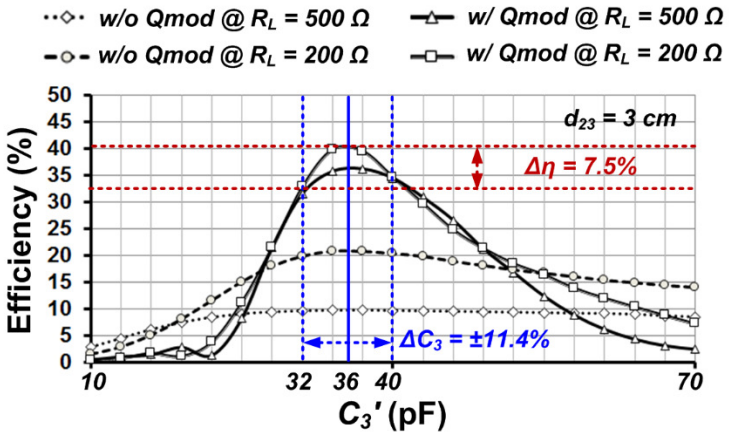

Fig. 2.15. Simulated η_{Qmod} vs. C_3' variations with and without multi-cycle Q-modulation when R_L = 200 Ω and d_{23} = 3 cm. With 11.4% change in C_3', η_{Qmod} decreases by 7.5% in the Q-modulated 2-coil link, while it only decreases by 2% in the conventional 2-coil link.

To resonate the L_3C_3-tank at f_p, a mechanism similar to the ART used in the power management integrated circuit (PMIC) in [82] was adopted, but implemented with COTS components only. Details of the ART design and operation, and its impact on the inductive link are discussed in [82]. The ART constantly tries to find the maximum η_{Qmod} in a closed loop to oppose any capacitance or inductance changes imposed by the surrounding environment, parasitic components, process, or duty-cycle variations. In the current prototype, C_{ART} is implemented as a 5-bit binary capacitor bank, swept from 0.15 pF to 11.7 pF by the MCU on the Rx side. Considering the parasitic capacitance of the NMOS switches (~5.9 pF), the implemented ART can compensate the L_3C_3-tank variations to resonate at f_p = 13.56 MHz.

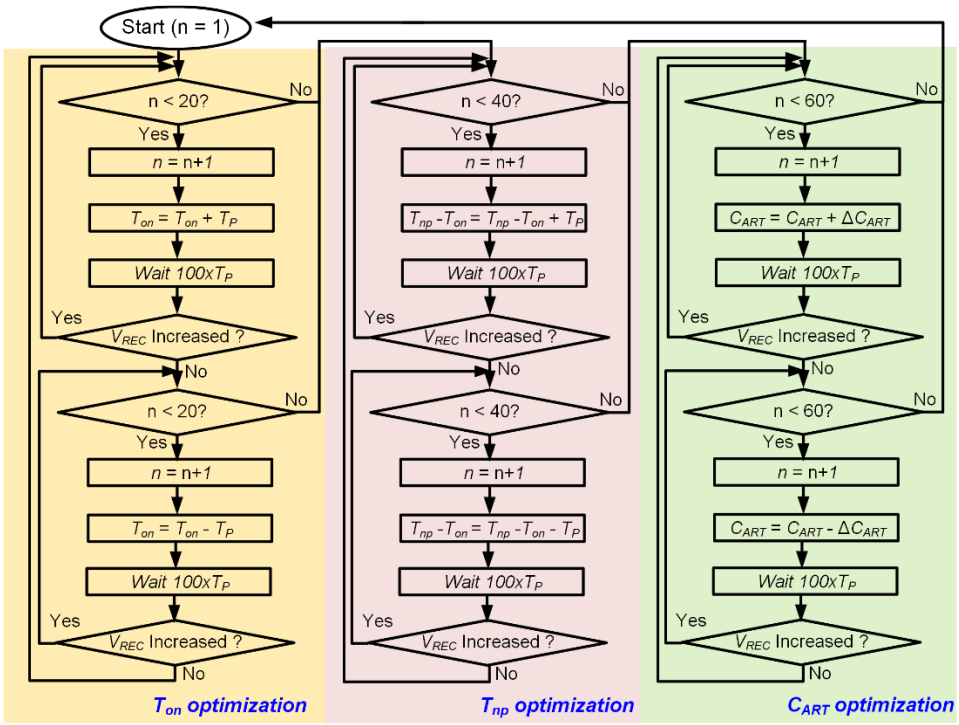

Fig. 2.16. Flowchart of the control algorithm for multi-cycle Q-modulation with ART, which is implemented in the MCU of the current proof-of-concept prototype Rx module.

The implemented algorithm in the MCU, shown in Fig. 2.16, seeks maximum PDL by sweeping T_{on} and T_{np} for the multi-cycle Q-modulation and C_{ART} for the ART, while monitoring V_{REC}. Since k_{12} between the coils in this prototype is small, as shown in

Table 2.3, the optimal R_L for PTE and PDL is almost the same [22], and the proposed algorithm to monitor V_{REC} in the multi-cycle Q-modulation optimizes the PTE as well.

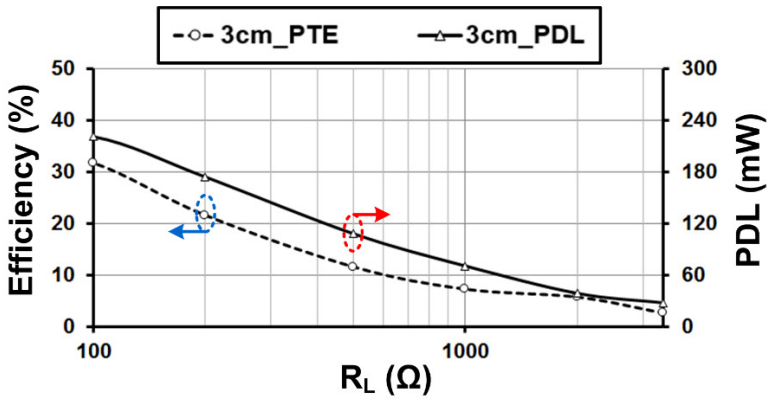

Fig. 2.17. Measured PA + link efficiency and PDL in the 2-coil inductive link at d_{23} = 3 cm vs. loading variations from 100 Ω to 3.4 kΩ without multi-cycle Q-modulation.

In Fig. 2.17, the measured PA + link efficiency (PTE) and PDL are shown in the 2-coil inductive link at d_{23} = 3 cm *vs.* loading variations from 100 Ω to 3.4 kΩ without multi-cycle Q-modulation. These curves show that the PDL and PTE follow the same trend and their optimization within PTE < 40% lead to the same result. V_{REC} is sampled and digitized before and after stepping T_{on} to decide the optimal pulse width of the SC signal, during which resonating power builds up in the Rx LC-tank. Then, the optimal T_{np}-T_{on} is decided for transferring the stored energy to R_L through the same procedure, while T_{on} is fixed. In the last step, the optimal C_{ART} is decided based on the optimal T_{on} and T_{np} values (see Fig. 2.16). The optimization order of T_{on}, T_{np}-T_{on}, and C_{ART} is not very important because they are repeatedly optimized during the operation. Since these parameters effects on the PTE independently, they can be optimized individually unless the Rx can't receive the enough power from the inductive link. This simple iterative process, which has been implemented in an ultra low power MCU (MSP430), can dynamically search for and reach/track the highest available PDL and PTE for any given inductive link combination, unless the PTE distribution in Fig. 2.12a, which is decided by T_{on} and T_{np}-T_{on}, has more than one peak.

2.2.5 Measurement Results

The proposed multi-cycle Q-modulation + ART techniques were verified by a small (1.5 × 1.8 cm^2) proof-of-concept prototype Rx module made of COTS components for the experimental setup shown in Fig. 2.18. The 5-bit capacitor bank, controlled by 5 NMOSs and an MSP430 MCU running the algorithm in Fig. 2.16, provides fine-tuning in parallel with the Rx series LC-tank, which can be considered as part of the resonance capacitor, C_3 [40]. For instance, when SC is closed, the parallel capacitor bank and C_3 are connected to the DC ground, and resonate at f_p. The SC is controlled by the MCU to reduce the current from the L_3C_3-tank to the rectifier down to zero. This has the same effect as directly shorting the load in the theoretical model of Fig. 2.10 because the loading, R_L, is defined as the resistive equivalent of all the power consumption following the rectifier.

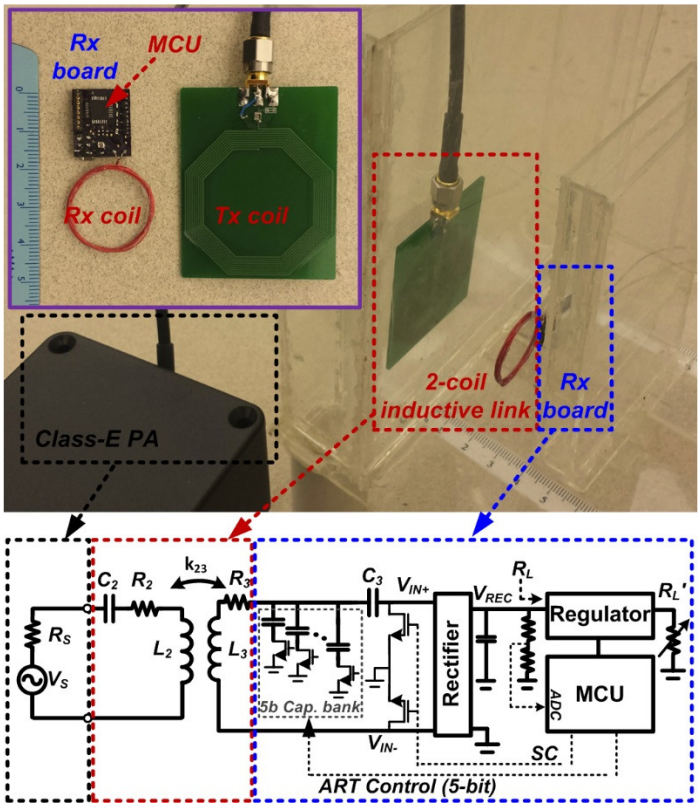

Fig. 2.18. Experimental setup and block diagram of a simple proof-of-concept multi-cycle Q-modulation Rx prototype with ART (enclosed in the blue box).

Rectification following the LC-tank is provided by a full-wave low dropout Schottky diode bridge (BAS4002A). V_{REC} is sampled and digitized by the MSP430 built in ADC through a resistive attenuator. To demonstrate the PA + link efficiency dependence on the load with and without multi-cycle Q-modulation, the 7.4 mW power consumption of in the MCU is excluded from this measurement. As shown in Fig. 2.18 schematic, R_L in these measurements is the equivalent resistance following the rectifier, calculated from V_{REC}/I_{REC}, where I_{REC} is the average current out of the full-wave rectifier. In order to set R_L at a desired value, besides the MCU and regulator internal power consumption, which are relatively constant, an additional variable resistance, R_L', was added to the Rx board and its value was swept from 110 Ω to 27 kΩ.

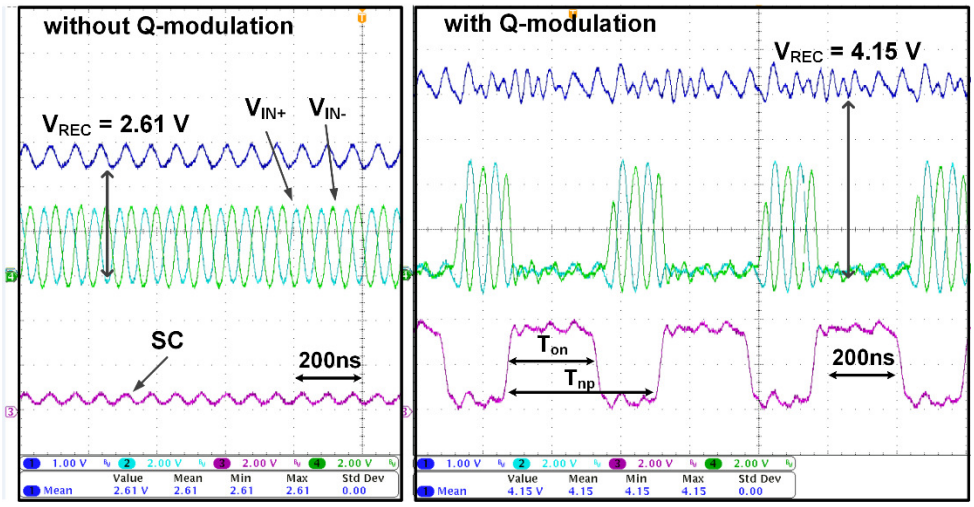

Fig. 2.19. Measured transient waveforms of V_{REC}, V_{IN+}, V_{IN-}, and SC in Fig. 2.16 without and with automatic multi-cycle Q-modulation at $P_{Vs,rms}$ = 151 mW, f_p = 13.56 MHz, R_L = 500 Ω, and d_{23} = 3 cm.

Fig. 2.19 shows the measured transient waveforms of V_{REC}, V_{IN+}, V_{IN-}, and SC in Fig. 2.18 with and without the proposed multi-cycle Q-modulation algorithm in Fig. 2.16, when R_L = 500 Ω and d_{23} = 3 cm. It can be seen that the rectifier input voltages, V_{IN+} and V_{IN-}, are boosted by Q-modulation, and V_{REC} has increased significantly from an average of 2.61 V to 4.15 V with the same RF input source, V_S, coil separation, and R_L.

To evaluate the performance of the multi-cycle Q-modulation and ART in terms of PA + link efficiency, η_{Qmod}, six conditions were tested in Fig. 2.18 setup: 1) manual

tuning without Q-modulation, 2) deliberate 4 pF detuning of C_3' without Q-modulation, 3) ART without Q-modulation, 4) manual tuning with Q-modulation, 5) automatic Q-modulation, and 6) ART + automatic Q-modulation, using the algorithm in Fig. 2.16. Figs. 2.18a and 2.18b show the results of these measurements vs. R_L at d_{23} = 3 cm and vs. d_{23} at R_L = 500 Ω, respectively. The PA + link efficiency was calculated by measuring the input power from the source and input power before the rectifier, considering the rectifier efficiency from the datasheet.

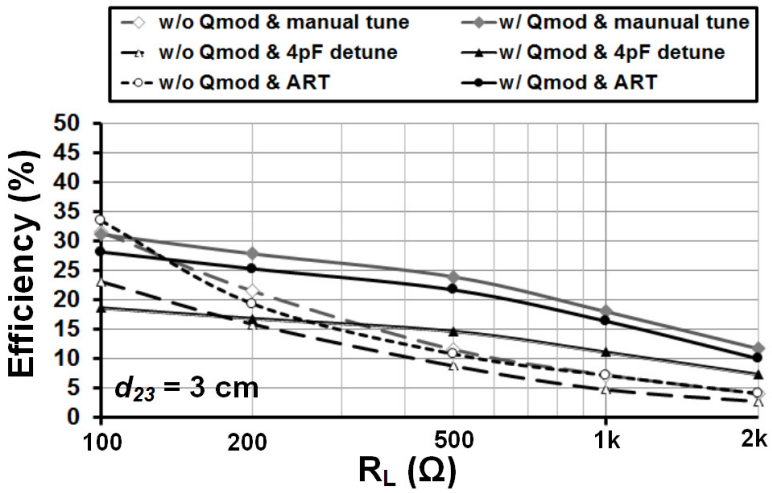

(a)

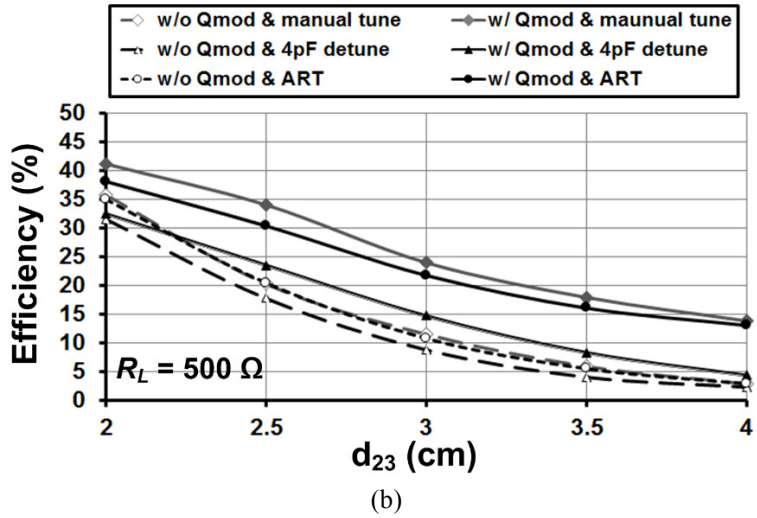

(b)

Fig. 2.20. Measured results of PA + link efficiency in 6 different conditions: with and without Q-modulation and manual tuning, with and without Q-modulation and 4 pF detuning of the Rx LC-tank, without Q modulation but with ART, and with both automatic Q-modulation and ART. (a) η_{Qmod} vs. load at d_{23} = 3 cm, and (b) η_{Qmod} vs. distance at R_L = 500 Ω.

The results show that the proposed multi-cycle Q-modulation has significantly increased η_{Qmod} over a wide range of R_L and d_{23}, which are two parameters that often change during WPT in operation. For instance, in Fig. 2.20a, the multi-cycle Q-modulation with manual tuning has increased η_{Qmod} from 7.2% to 18.1% at R_L = 1 kΩ and d_{23} = 3 cm. Similarly, in Fig. 2.20b, the multi-cycle Q-modulation has improved η_{Qmod} from 20.4% to 34.0% at d_{23} = 2.5 cm and R_L = 500 Ω.

The fully automated multi-cycle Q-modulation and ART show a slightly lower efficiency than the externally controlled Q-modulation, because T_{on}, T_{np}-T_{on}, and C_{ART} fluctuate due to their continuous up/down search around their optimal values, according to the algorithm in Fig. 2.16. The 4 pF detuning degrades η_{Qmod} with Q-modulation more than a conventional 2-coil link, as discussed in Fig. 2.15, because of the higher Q-factor in the former link. However, the ART can successfully compensate for detuning of C_3' to achieve the highest η_{Qmod} close to manual tuning. Figs. 2.20a and 2.20b also show that the ART operation with and without the multi-cycle Q-modulation at R_L = 500 Ω and d_{23} = 3 cm improves the efficiency by 1.9 % and 7.1 % for a 4 pF detuning of C_3', respectively. The measurement results demonstrate that the effect of the ART operation with the multi-cycle Q-modulation in the 2-coil inductive link is advantageous compared to the same condition without multi-cycle Q-modulation, which can also be seen in Fig. 2.15. In this experiment, the maximum PDL was 168.1 mW at R_L = 100 Ω when V_{REC} = 4.1 V.

Fig. 2.21 shows the measured transient waveforms of V_{REC}, V_{IN+}, V_{IN-}, and SC with automatic multi-cycle Q-modulation and ART when the load suddenly changes from R_L = 500 Ω to R_L = 250 Ω at d_{23} = 3 cm. V_{REC} suddenly drop from 4.22 V to 3.33 V due to higher current demand. Fig. 8 algorithm in the MSP430 tries to find a new optimal T_{on} and T_{np} combination that would be a batter match for the new loading, and as a result, recovers part of V_{REC} drop to stabilize at 3.78 V. The zoomed-in segments at the bottom

of Fig. 13 shows that at steady state, T_{on} and T_{np} have changed from 258 ns and 437 ns for R_L = 500 Ω to 191 ns and 371 ns for R_L = 250 Ω, respectively.

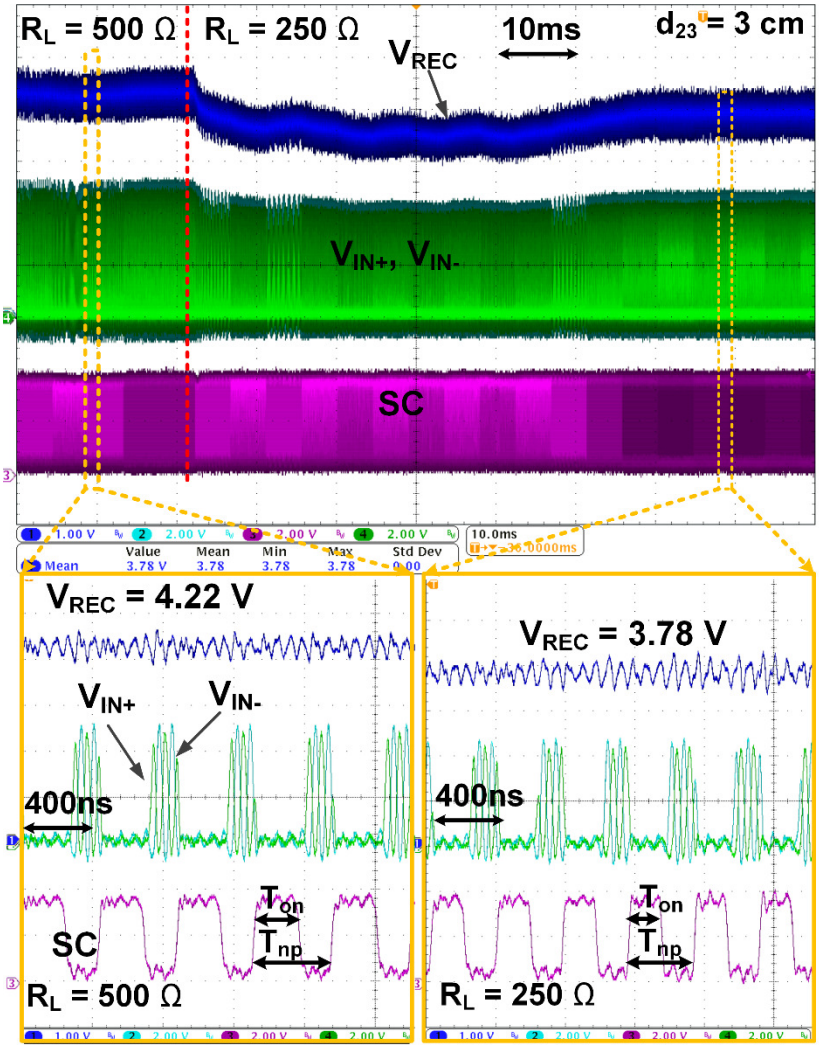

Fig. 2.21. Measured transient waveforms of V_{REC}, V_{IN+}, V_{IN-}, and SC with automatic multi-cycle Q-modulation and ART for sudden load variation from R_L = 500 Ω to 250 Ω at d_{23} = 3 cm. The algorithm in Fig. 2.16 finds new optimal T_{on} and T_{np} to maximize η_{Qmod} for the new load condition, and as a result T_{on} and T_{np} change from 258 ns and 437 ns to 191 ns and 371 ns, respectively.

III. TOWARDS A THREE-PHASE TIME-MULTIPLEXED PLANAR POWER TRANSMISSION TO DISTRIBUTED IMPLANTS

3.1 Three-Phase Time-Multiplexed Planar Power Transmission to Distributed Biomedical Implants

In this chapter, a new architecture for a three-phase time-multiplexed scalable power Tx was presented, which has the ability to wirelessly power a large number of distributed receivers (Rx) with arbitrary angular and spatial misalignments across a large plane as shown in Fig. 1.5. The Tx includes three layers of hexagonal planar spiral coils (hex-PSC) for homogeneous distribution of the power transfer efficiency (PTE) and an array of three-phase time- multiplexed RF drivers to generate both vertical and lateral magnetic flux over the entire powered 3D volume. The proposed architecture can not only be applicable to small biomedical implants distributed over large areas of the brain but also any wirelessly-powered mobile unit, with random angular or spatial misalignments, such as multiple socially interacting animal subjects in an EnerCage system [40].

3.1.1 Theory of Three-Phase Power Transmitter for Hex-PSC Array

The origin of the proposed Tx architecture is a proven technology, called EnerCage [40][85], which was developed to continuously power and communicate with an electronic device attached to or implanted in a freely behaving animal in a smart cage. In the EnerCage system, three layers of overlapping hex-PSCs are used to provide homogeneous PTE over an extended area. However, only one or two hex-PSCs are activated at any time to power one Rx in the cage. Here, the goal is to simultaneously power numerous receivers distributed over an extended target area with arbitrary position and angular misalignments. Fig. 3.1a shows three examples of angular alignment in a spherical coordinate system, used in this paper and represented by (θ, φ).

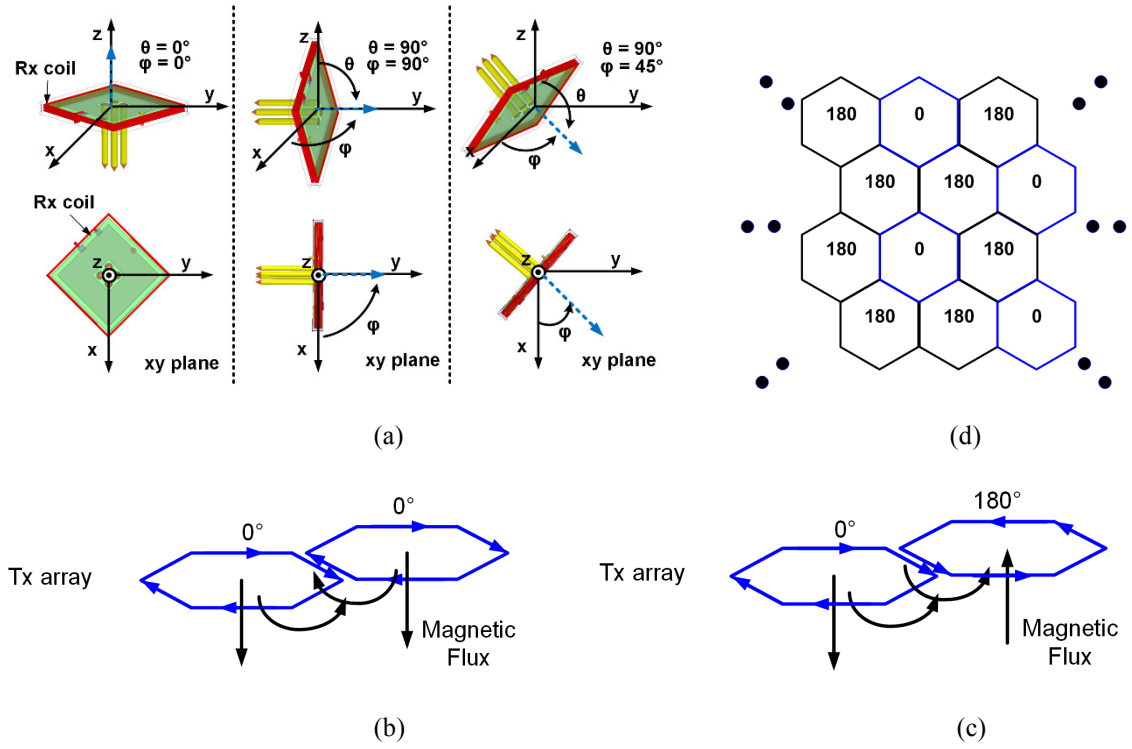

Fig. 3.1. (a) Three examples of angular alignment in the spherical coordinate system used in this paper and represented by (θ, φ). (b) Conventional in-phase excitation of the hex-PSC array. Current flows in opposite directions in adjacent segments of the neighboring hex-PSCs. (c) Out-of-phase excitation of the hex-PSC array, which helps with (90°, 90°) case. However, the vertical field is weakened for horizontal Rx coils (90°, any) when the hex-PSC array is extended over the 2D plane, as shown in (d).

If all hex-PSCs in each layer are activated in-phase, as shown in Fig. 3.1b, current flows in opposite directions in the adjacent coils and the resulting magnetic fields cancel out, leaving only the edges of the hex-PSCs on the outer perimeter of the array, and reducing the overall PTE. Moreover, since the resulting magnetic field is primarily vertical to the hex-PSC plane, this method of excitation does not address the Rx angular misalignment, resulting from the fact that the coupling coefficient, k, drops roughly proportional to $cos(\theta)$ [86].

The solution offered in [87] for the angular misalignment was driving the adjacent coils closest to the Rx with a pair of out-of- phase carrier signals to reinforce the horizontal component of the magnetic field at the Rx location, as shown in Fig. 3.1c. This out-of-phase excitation can power an Rx coil that is close to the hex-PSC array when it is

tiled by θ = 90° (worst case condition). However, it is not extendable to a large number of arbitrarily located/aligned Rx coils over an extended area. Because the vertical magnetic field generated by the adjacent out-of-phase hex-PSCs weaken one another at the positon of a horizontal Rx that is further away from the PSC array, resulting in significant reduction in the PTE. The 180° phase-shift cannot be extend over the coverage area either because each hex-PSC is surrounded by 6 adjacent PSCs, as shown in Fig. 3.1d. Although 180° out-of-phase array satisfies extension via square-shaped PSCs in 4 layers [88], the vertical magnetic field attenuation at the Rx positon would still occur.

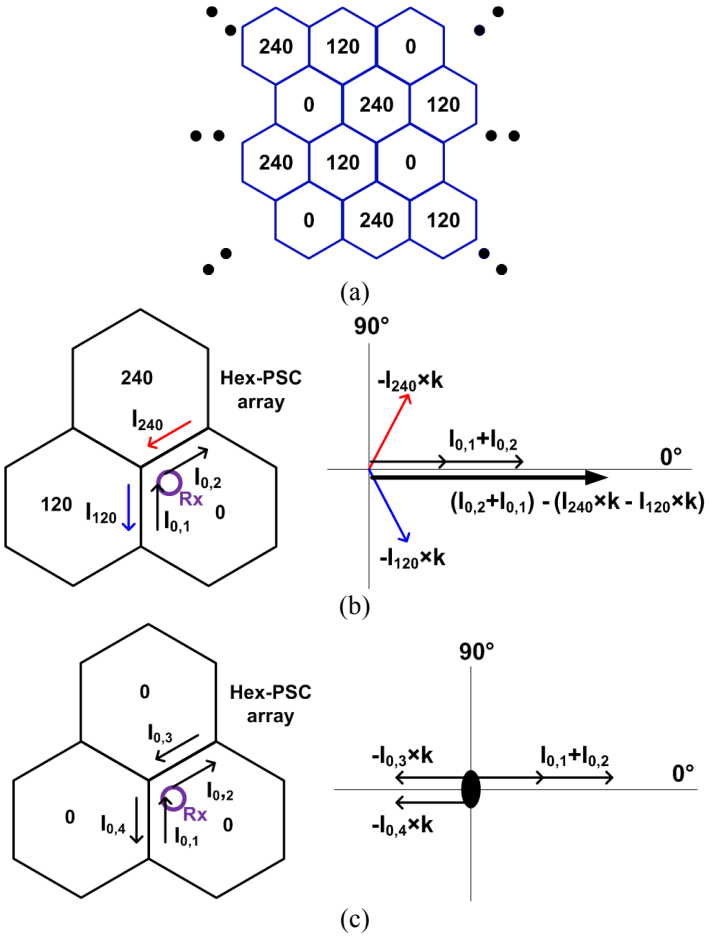

Fig. 3.2. (a) Phase distribution among the hex-PSCs in one conductive layer: The phase difference between any two adjacent hex-PSCs is either 120˚ or 240˚. (b) Current vector diagram in the proposed 120˚offset excitation: Part of the magnetic field generated from I_{240} and I_{120} is coupled with coupling coefficient k to the magnetic field generated from $I_{0,2}$ and $I_{0,1}$. The resulting current induced by the 0˚ coil is increased from its original value $I_{0,1}+I_{0,2}$ because of the constructive nature of the adjacent fields. (c) Current vector diagram in in-phase excitation: The direction of magnetic field coupling is destructive, and the resulting current in the Rx coil is reduced.

Here, we present a new solution for driving a scalable array of hex-PSCs in a way that it can power not only vertically- oriented receivers but also those with angular misalignments. Fig. 3.2a shows the geometry and relative positioning of the hex-PSCs with 120° excitation phase shift between adjacent coils. This arrangement significantly improves both the vertical and angular magnetic fields over the extended 3D space. In this excitation scheme, every three adjacent hex-PSCs are driven by β = 0°, 120°, or 240° carrier signals, similar to three-phase electric power grids. Fig. 3.2b shows that the inductive coupling between any two adjacent coils is constructive at the Rx position, thanks to the 120° phase difference. If we consider a simple case of an Rx coil positioned symmetrical with respect to the nearest hex-PSC segments, and superimpose the magnetic field generated from those segments of the 120° and 240° phase shifted hex-PSCs (carrying I_{120} and I_{240}) with those from the 0° hex-PSC (carrying I_0) and consider their associated coupling coefficient, k, then, the resultant magnetic field of the 0° coil with respect to Rx, B_0, is increased from its original value according to,

$$\begin{cases} I_{0,1} = I_{0,2} = \alpha \sin(\beta) \\ I_{120} = \alpha \sin(\beta - 120\,^\circ) \\ I_{120} = \alpha \sin(\beta - 240\,^\circ) \end{cases} \tag{3.1}$$

$$\begin{aligned} B_0 &\propto (I_{0,1} - k \cdot I_{120} + I_{0,2} - k \cdot I_{240}) \\ &= 2 \cdot \alpha \sin(\beta) - k \cdot \alpha \sin(\beta - 120\,^\circ) - k \cdot \alpha \sin(\beta - 240\,^\circ) \\ &= 2 \cdot \alpha \sin(\beta) + k \cdot \alpha \cdot [2 \cdot \sin(-\beta + 180\,^\circ) \cdot \cos(120\,^\circ)] \\ &= 2 \cdot \alpha \sin(\beta) - k \cdot \alpha \sin(\beta - 180^\circ) \\ &= \alpha (2 + k) \sin(\beta) \end{aligned} \tag{3.2}$$

where α is the amplitude of the current and β is the phase of the current. In contrast, in the in-phase excitation in Fig. 3.2c, the coupling between any two adjacent hex-PSCs is destructive, resulting in weakening of the induced current in the Rx coil,

$$B_0 \propto (I_{0,1} - k \cdot I_{0,3} + I_{0,2} - k \cdot I_{0,4})$$
$$= 2 \cdot \alpha \sin(\beta) - 2k \cdot \alpha \sin(\beta) = \alpha(2-2k)\sin(\beta) \quad (3.3)$$

Therefore, the proposed three-phase excited hex-PSC array is able to extend the WPT coverage without suffering from the magnetic field attenuation effect, and can also accommodate Rx coils with angular misalignments.

3.1.2 Three-Phase Time-Multiplexed Transmitter

Although the hex-PSC array with three-phase excitation can simultaneously power the horizontally- and even vertically- oriented Rx coils, our simulations showed that there still exist dead-zones for these extreme Rx orientations at the boundaries of every two adjacent hex-PSCs and at the center of each hex-PSC, respectively. Fig. 3.3a shows a few Rx coils distributed over one layer of hex-PSC array with various positions and orientations. The horizontally-oriented Rx coils #1, #5, and #10 are located near the center of hex-PSCs and can be powered, as shown in Fig. 3.3b, while Rx coil #3 cannot be powered because the lateral magnetic field is weak in the center of a hex-PCS, as shown in Figs 3.3c. In contrast, at the boundaries of hex-PSCs, lateral magnetic fields are stronger and vertical magnetic fields are weaker, resulting in vertically-oriented Rx coils #2 and #6 in Fig. 4a receive more power than horizontally-oriented coils #4 and #9, as shown in Figs. 3.3b and 3.3c, respectively. The directionality (φ) of the vertically-oriented Rx coils is also important, as shown in the case of Rx coils #7 and #8 in Fig. 3.3c, which do not receive enough power despite being located near the boundaries of the hex-PSCs.

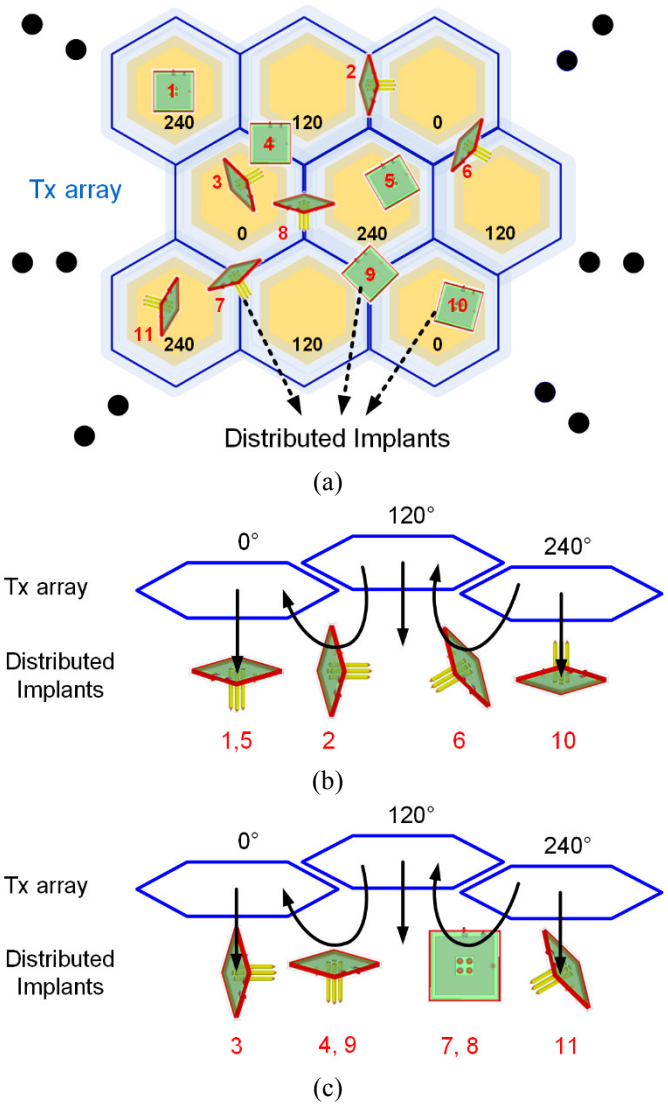

Fig. 3.3. (a) Top view of distributed Rx coils in various orientations and positions over one layer of three-phase driven hex-PSC array. (b) Distributed Rx coils which can receive enough power from this layer of the hex-PSC arrays. (c) Distributed Rx coils which cannot receive enough power from this layer and need to be powered by the other two overlapping layers.

To eliminate the aforementioned dead-zones and create a homogeneous PTE over an extended volume around the Tx plane, we have combined three layers of hex-PSC arrays by offsetting the centers of every three adjacent hex-PSCs on three different layers to be on the corners of an equilateral triangle [87]. This is shown from the top and side views in Fig. 3.4a, in which three conductive hex-PSC layers in blue, green, and red are stacked to create an overlapping hex-PSC array. These three layers cannot be driven with

the aforementioned three-phase signal at the same time because the magnetic fields from each layer will be destructive to the fields generated by the other two layers. Hence, each layer is time-division multiplexed (TDM), as shown in Fig. 3.4b, to avoid any electromagnetic interference between layers. The appropriate TDM period, *T*, is decided by the carrier frequency, time constant of the capacitance following the Rx coil and rectifier, Rx loading, and the acceptable level of ripple on the regulated supply voltage of the electronics that are powered by the Rx coil.

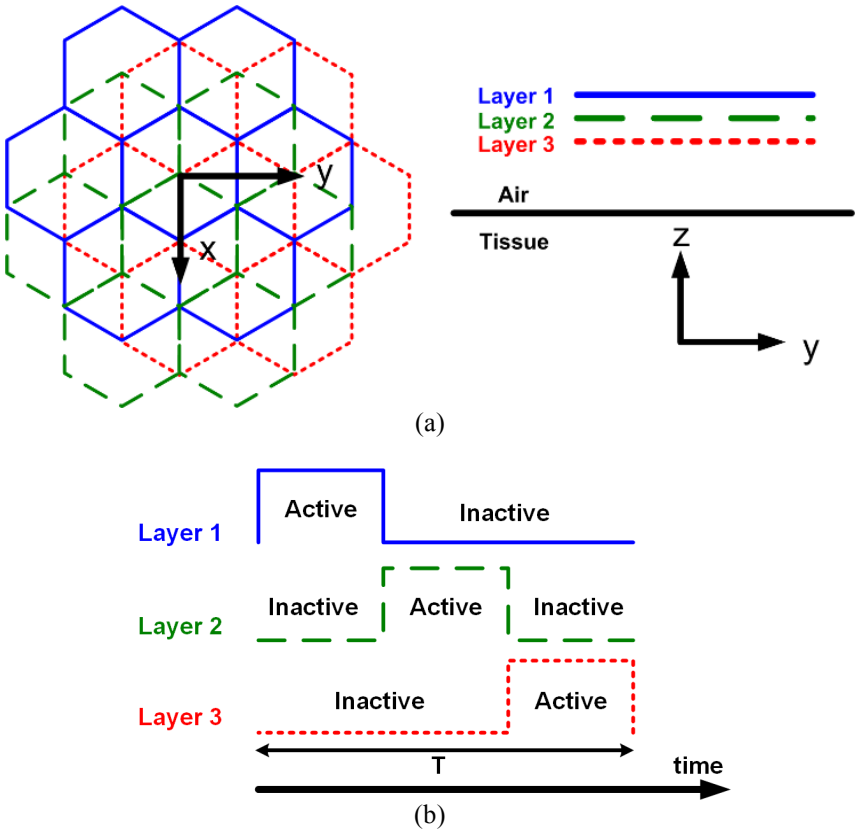

Fig. 3.4. (a) Schematic diagram of the three-layer hex-PSC array for the Tx plane from top (left) and side (right) views. (b) Active periods of each layer in Fig. 5a for 33% of the overall period, *T*, as each hex-PSC in each layer is driven by the three-phase carrier signal in Fig. 3.2.

One of the important design considerations for the power amplifiers (PA) used to drive the overlapping hex-PSC array in the three-phase TDM scheme is the ability to rapidly charge and discharge the LC-tank in each Tx coil. Because each hex-PSC array should be repeatedly turned on and off by the control signals, shown in Fig. 3.4b, and a

delayed charge or discharge time in one layer can affect the wireless link PTE by degrading the magnetic field generated by another layer. Normally when the PA is turned off, the residual energy stored in the LC-tank is dissipated by the parasitic resistance in the LC-tank and the matching circuit in the PA.

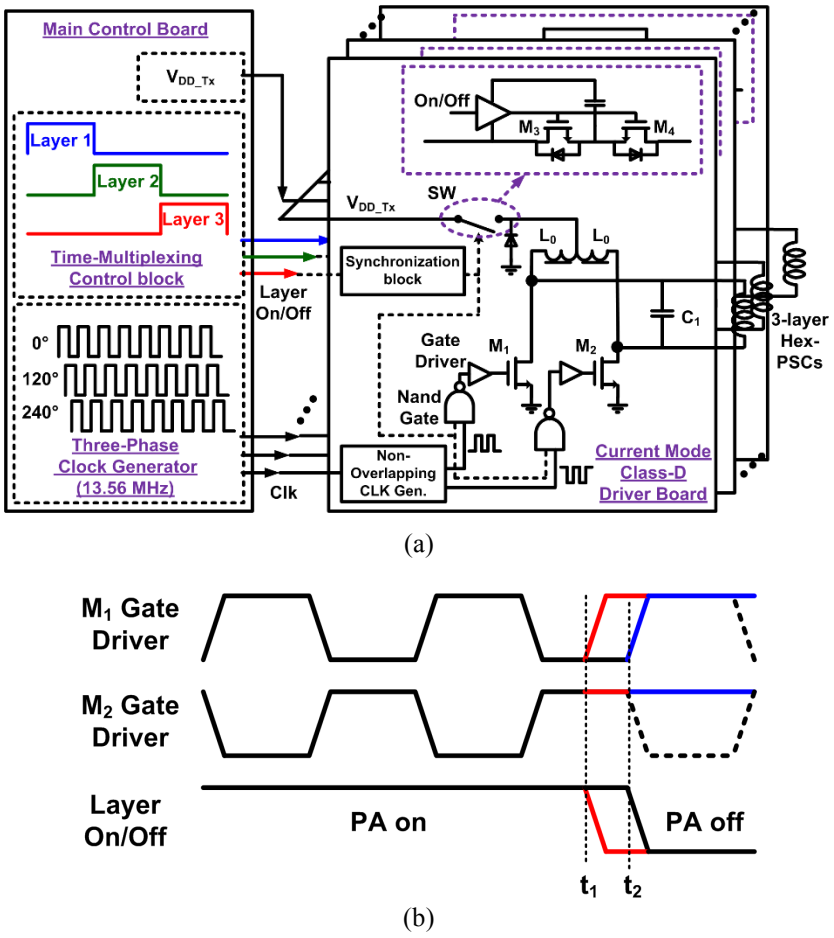

Fig. 3.5. (a) Schematic diagram of the three-phase TDM current mode class-D PA for driving three-layer overlapping hex-PSCs. (b) Control signals for the gate drivers of M_1 and M_2, and layer/PA on/off. The control signals should be synchronized at t_2 while switching at other times should be avoided.

Fig. 3.5a shows the simplified schematic diagram of a three- phase TDM current mode class-D (CMCD) PA, as part of the distributed Tx. The control block provides three-phase clock signals at 13.56 MHz in the industrial-scientific and medical (ISM) band, which are 0°, 120°, and 240° phase shifted, as well as three TDM control pulses for each CMCD PA board. The CMCD PAs in [89] is a suitable choice for rapidly

deactivating the LC- tank because the LC-tank terminals can be grounded and shorted by activating both M_1 and M_2 together. This will provide a free-wheeling path for the inductor current, avoiding a high voltage spike across M_1 and M_2, which could result in device failure.

A pair of non-overlapping clock pulses are generated in each PA from the three-phase clock signal associated to each layer to drive M_1 and M_2, while being masked with the layer on/off signal from the TDM control block. When the TDM signal is high, supply provides current to the corresponding CMCD PA board, and when the TDM signal is low, the PA is disabled and both gate drivers for M_1 and M_2 are raised to short the LC-tank to ground. The two ends of each parallel LC-tank in the Tx array are shorted to ground by switches M_1 and M_2 to quickly reduce the resonant current in the LC-tank down to zero during the off phase, and facilitate a sharp TDM using current mode class-D PAs. There is some undesired mutual coupling between the overlapping coils in different layers, which is small because the shorted parallel LC-tank does not resonate at 13.56 MHz. As a result, the induced current and corresponding power loss in the shorted Tx coil is not high. More specifically, the current in the shorted Tx coil depends on not only the mutual coupling but also its resonant frequency. Since the shorted Tx coil is no longer a resonator, the current is small. The on/off timing of the PA is critical because it should not be turned off when there is high voltage across the LC-tank. Simultaneous high voltages and currents across the MOSFET switches may destroy them when they are turned on by the TDM signal. Therefore, the PA should be turned off at a moment that the voltage across the LC-tank is the lowest. At this moment, the current in L_0 is the maximum based on the basic CMCD operation [90]. Back-to-back MOSFET switches, M_3 and M_4 are used to completely isolate the power source from the inductor, L_0 when the TDM signal goes low. The free-wheeling current in L_0 passes through the free-wheeling diode between L_0 center tap and ground, and the residual energy dissipates in the parasitic resistance of M_1 and M_2 during the M_1 and M_2 on time.

Fig. 3.5b shows the desired non-overlapping clock for M_1 and M_2 gates and the layer on/off TDM signals. The timing between TDM and gate drive signals should be synchronized at t_2 to achieve the zero-voltage switching condition. Switching the PA off at any other time, like t_1 should be avoided. Positive edge-triggered D-type flip-flop (74AHC74) is used in the sync block of Fig. 3.5a for this purpose. The TDM signal in Fig. 5b is implemented by a decade counter with a "master reset" pin to count up to three. The 120˚-shifted gate driver signals are generated by a DS1100Z fixed delay element. Each tap of DS1100Z has 25 ns delay, which is almost the equivalent of 120˚ phase shift in a 13.56 MHz clock. Fig. 3.6 shows the measured TDM signal and corresponding voltage across the LC-tank in a hex-PSC. The TDM frequency in this prototype is 10 kHz with 33% duty cycle. These waveforms show that TDM signal turns off the PA when the voltage across the LC-tank becomes low and the energy stored in the LC-tank dissipates in ~100 ns, without causing any voltage spike. The small oscillation across M_1 in Fig. 3.6 when the layer is off is partly because of this induced current and partly because of the induced voltage in the probing instrument, which also results in a noisy GND terminal, visible in the digital layer-on/off control signal in Fig. 3.6.

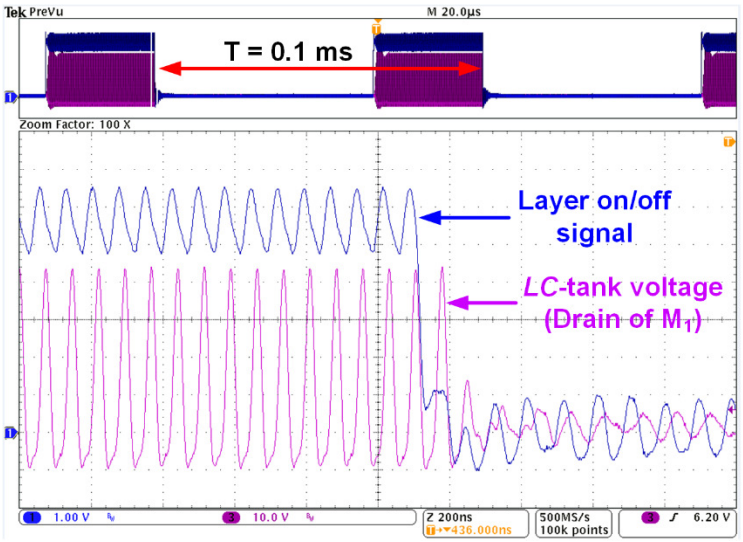

Fig. 3.6. Measured waveforms of layer on/off signal for controlling each hex-PSC layer and the corresponding LC-tank voltage at the drain of M_1.

3.1.3 Simulation Results

Scaled-up prototypes of the hex-PSC array and Rx coil were designed and fabricated as a proof-of-concept for the proposed three-phase TDM wireless power transmission to randomly distributed receivers. Unlike the earlier EnerCage design, which focuses the delivered power on a handful of moving targets, the new scheme is meant to homogeneously power an entire volume, where numerous receivers are distributed.

TABLE 3.1. COIL SPECIFICATIONS FOR THE PROTOTYPE 3-PHASE WPT SYSTEM

Parameters	Value
Hex-PSC implemented on two double-layer 1 oz FR4 PCBs as the substrate on the Tx side (L_2)	Inductance = 680 nH Outer diameter = 12.7 cm Number of turns = 2 Line width/spacing = 10/7 mm Conductor thickness = 35 µm Q_2 = ~160 for PSCs on layer 1 Q_2 = ~136 for PSCs on layer 2 Q_2 = ~154 for PSCs on layer 3
Wire-wound coil with 44 strand Litz wire on the Rx side (L_3)	Inductance = 224 nH Diameter = 1 cm Number of turns = 3 Wire diameter = 0.25 mm Quality factor = 125
L_2-L_3 nominal distance (d_{23})	7 cm
Nominal DC load (R_L)	5 kΩ (~5 mW)
Operating frequency (f_p)	13.56 MHz
TDM frequency (1/T)	10 kHz

Dimensions of the hex-PSC array and wire-wound coil on the Tx and Rx sides were adopted from the optimization procedure in [87], and summarized in Table 3.1. Each coil in the three- layered hex-PSC array has 12.7 cm outer diameter with two turns. A fourth layer on the printed circuit board (PCB) was used for interconnects between the PA and hex-PSCs. The Rx coil diameter was limited to 1 cm in the coil optimization procedure [25], and the nominal distance between the Rx coil and the Tx array was set to 7 cm in this proof-of-concept scaled-up prototype with a factor of ~7. The optimization procedure for small implants with shorter Tx-Rx separation has been presented elsewhere

[70]. The nominal DC load, RL = 5 kΩ, corresponds to ~5 mW power consumption in the Rx, in which the selected number of turns, n3 = 3, offers maximum PTE [25].

Operation of the three-layer overlapping hex-PSC array, driven by a three-phase TDM sinusoidal carrier signal at 13.56 MHz was simulated using a combination of the High Frequency Structure Simulator (HFSS, ANSYS) and Advanced Design System (ADS, Agilent) environments. To consider the cross- coupling among all coils, the S-parameters were extracted from the HFSS model, shown in Fig. 8a, in the form of a 13 × 13 matrix, consisting of 12 overlapping hex-PSCs on the Tx array and one Rx coil, which was swept within the orange-shaded area in three different scenarios of θ = 0°, φ = 0° (case-A), θ = 90°, φ = 90° (case-B), and θ = 90°, φ = 45° (case-C). The S-parameter matrix was then used in an ADS circuit model, in which 12 hex-PSCs were driven by three-phase signals at 13.56 MHz that were time-division multiplexed at 10 kHz to power the Rx coil, being loaded by a 5 kΩ resistor. In the HFSS simulation environment, a "lumped port" was defined between the two ends of each coil and the boundary property was selected as "Radiation". The Tx array was placed in "FR4_epoxy," which has a relative permittivity of 4.4, considering the actual PCB material.

Figs. 3.7b, 3.7c, and 3.7d show the simulated PTE distributions of the in-phase (left) vs. three-phase/TDM (right) excitation of the overlapping hex-PSC array in case-A, case-B, and case-C, respectively. Although the power consumption in each Tx layer is time multiplexed, i.e. varies with time, the excitation cycle is periodic with 33.3% duty cycle. Therefore, the power consumption can be averaged over *T* to calculate the overall system efficiency, which can be calculated by the ratio of the received power in the Rx and the average power consumed by one PA according to,

$$Efficiency(\%) = \frac{P_{R_L}}{P_{Supply} / n_{PA}} \times 100 \tag{3.4}$$

where P_{RL} is the power consumption in the load, P_{Supply} is the overall system power

consumption, and n_{PA} is the number of PAs used in the Tx.

With no angular misalignment in case-A, the average PTE with three-phase excitation has been reduced from 12.8% to 9.1%, because of the 120° phase-shift to increase the lateral magnetic flux between adjacent hex-PSCs. Since Rx coils that are in parallel with the hex-PSC plane are already in the best orientation to receive power, this nominal PTE reduction (28.9%) does not affect the system performance.

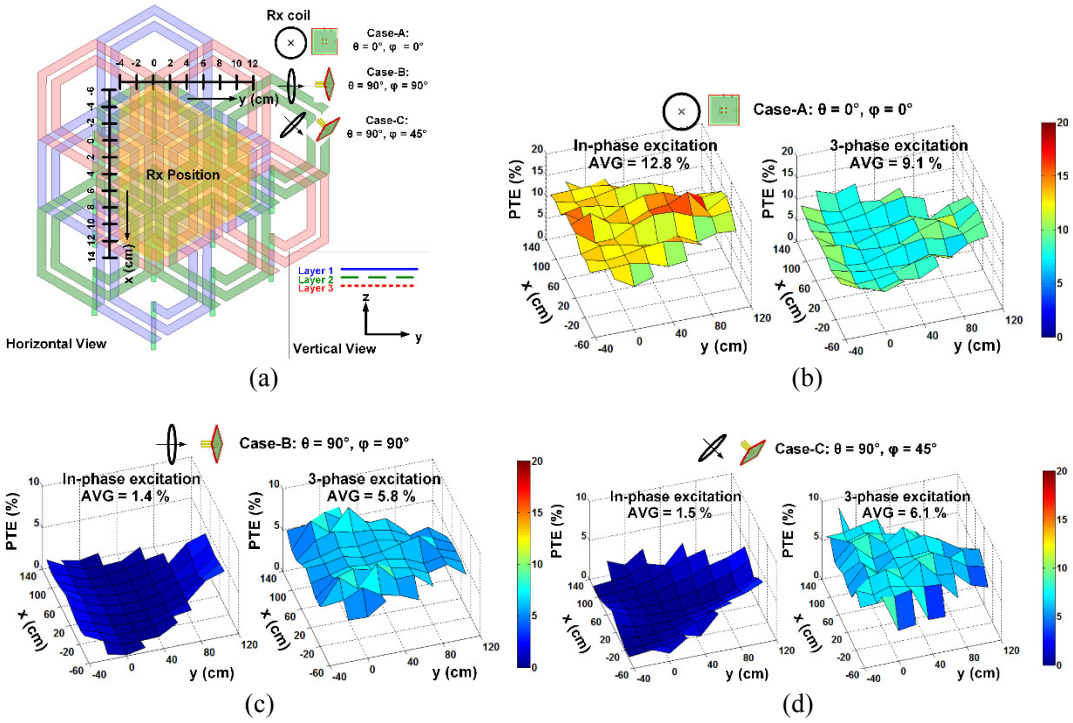

Fig. 3.7. Simulation results for three-phase TDM excitation of a three-layer hex-PSC array that constitutes the Tx plane with Rx at 7 cm above the surface: (a) HFSS model of the hex-PSC array with three cases of the Rx coil orientatoin. Orange-shaded area is where the Rx coil was swept to simulate the PTE distribution in the ADS for in-phase (left) and three-phase (right) excitations in (b) case-A, (c) case-B, and (d) case-C

The key impact of the three-phase excitation can, however, be observed in the significant increase in the average PTE in cases B and C, which are among the worst case scenarios for arbitrary Rx distribution. In Fig. 3.7c, the maximum and minimum PTEs in case-B are 4% and 0.02% for in-phase excitation vs. 8.66% and 4.1% for the three-phase excitation, respectively. Moreover, the average PTE across the powered area has been increased from 1.4% to 5.8%, a 392.8% increase. Similarly, in Fig. 3.7d, max/min and

average PTE have changed from 4.0%/0.02% and 1.5% for the in-phase to 8.4%/3.9% and 6.1% for the three-phase excitation, respectively, which represent a 306.6% improvement on average.

These simulation results clearly show that the proposed three-phase method for TDM excitation of overlapping three-layer hex-PSCs can significantly increases the PTE in the worst case scenarios, in which the power receivers are at the risk of malfunction due to insufficient power, at a cost of a modest PTE degradation in the best positions. Alternatively, these results indicate that to ensure fully functional receivers (e.g. implants) that are arbitrarily distributed within the powered 3D space, including those that are in the worst case positions or orientations, the transmitted power can be much less than the traditional in-phase method, using the same type of Tx coils. This is the result of a more homogeneous PTE distribution across the powered space for any angular and spatial misalignments. The PTE for the angular misalignment tends to drop along the edges of the simulated area because this simulation was limited to only 12 overlapping hex-PSCs due to extended simulation time with a larger number of coils. The uniform simulated area in Fig. 3.7a has a triangular shape inside (0, 0), (8, 0), (4, 7) coordinates. This inhomogeneity is expected to be reduced when the overlapping hex-PSC array is further extended to a larger array.

3.1.4 Experimental Measurements

Fig. 3.8 shows the measurement setup, with the hex-PSC array implemented on a pair of 2-layer 1 oz FR4 PCB, which are described in [85]. Each CMCD PA driver board, shown in the lower right inset was vertically mounted on the bottom of hex-PSC array, and connected to the main control board, shown in the lower right inset. The Rx board, shown in the upper right inset, includes the Rx coil specified in Table 3.1, a passive rectifier (BAS4002) followed by a 2 μF capacitor, and a 5 kΩ load. In this experiment, 7 coils were used to verify the operation of three-phase TDM excitation of a hex-PSC array,

as shown in Fig. 3.9a. The measurement procedure was similar to the simulations described in section IV.A, comparing the PTE of the in-phase and three-phase excitations for the three cases in Fig. 8a, while the Rx board was moved over the orange area in Fig. 3.9a at d_{23} = 7 cm.

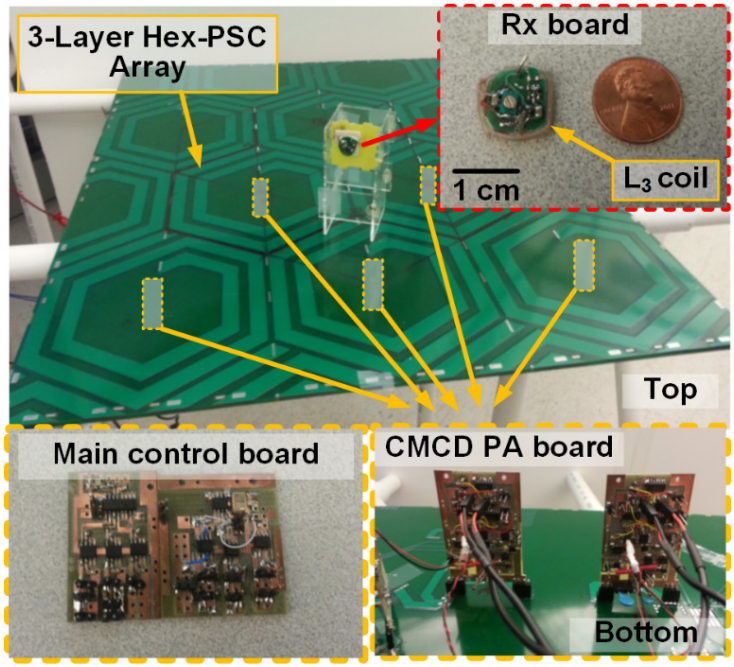

Fig. 3.8. Experimental set up for the three-phase TDM overlapping hex-PSC array. The control board on the lower left coordinates the activation of each CMCD PA board that is vertically mounted at the bottom of the PSC array to drive each hex-PSC. The Rx coil wound around the Rx board with 1 cm^2 area on the upper right has a rectifier circuit and 5 kΩ load.

Despite a smaller number of active hex-PSCs, the measured PTE distributions in Fig. 3.9 are in close agreement with the simulation results in Fig. 3.7. Although the average PTE for the parallel Rx coils, i.e. with no angular misalignment (case-A), was reduced from 12.8% with in-phase excitation to 9.1% with three-phase excitation, strengthened lateral magnetic field in three-phase excitation improved the average PTE from 0.86% to 4.9% in case-B and from 0.87% to 5.0% in case-C, where the average power delivered to the load (PDL) was 5.4 mW. Similar to simulation results, a drop in the PTE was observed at the boundaries of the area covered by the active hex-PSCs, which is expected to be flattened once the hex-PSC array and powered area is extended

beyond 7 coils. Multiple Tx coils that are in one layer and have the same phase can be driven by only one PA because they are all turned on/off at the same time and with the same phase. Therefore, theoretically, we only need three driver boards in each layer as long as the PA has the capability to drive all Tx coils. In practice, if some Tx coils are far from the PA, the long routing may cause additional losses. Therefore, determining the right number of PAs depends on each specific design.

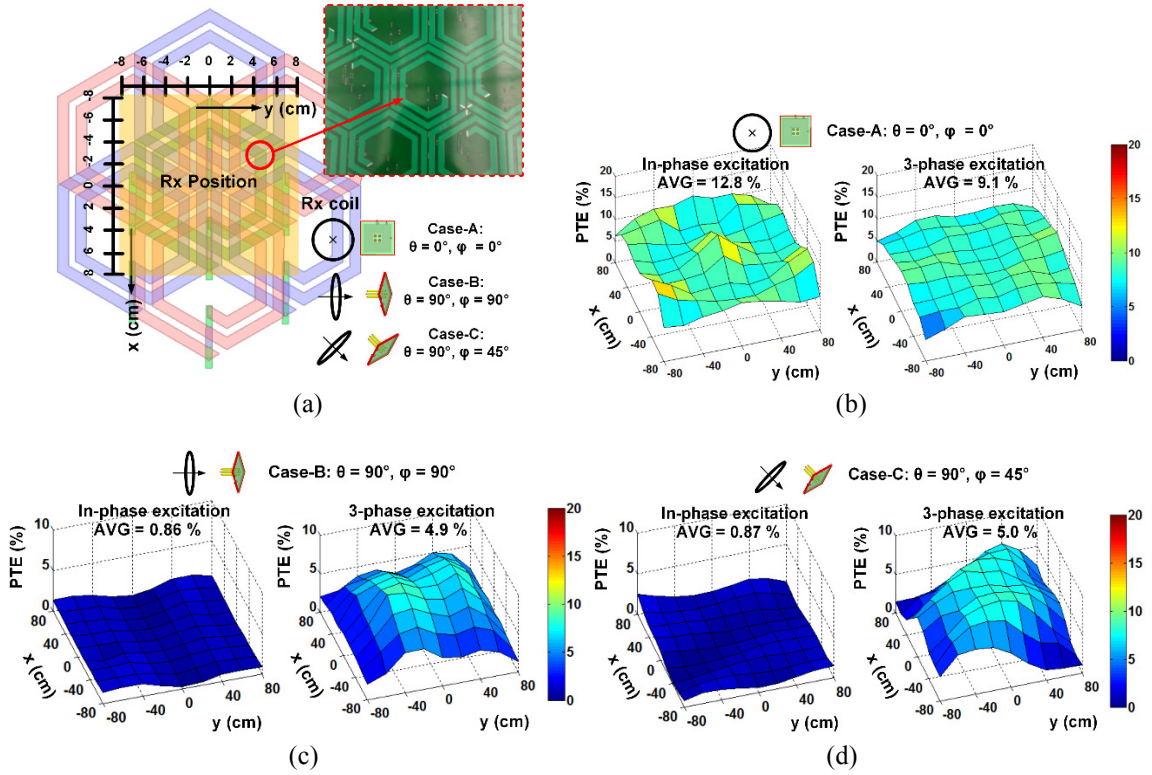

Fig.3.9. Measured results for three-phase TDM excitation of a three-layer hex-PSC array that constitutes the Tx plane with an Rx at 7 cm above the surface: (a) Top view of measurement setup with three cases of the Rx coil orientatoin. Orange-shaded area is where the Rx coil was swept to measure the PTE distributions for the in-phase (left) and three-phase (right) excitations in (b) case-A, (c) case-B, and (d) case-C.

Fig. 3.10 compares the measured and calculated PTE at 7 cm Tx-Rx separation and perfect alignment vs. load variations. The measured results indicate RL = 6 kΩ as the optimal loading, which is very close to the designed target of RL =5 kΩ. Fig. 3.11 shows the measured power flow from the DC source, VDD_Tx, to one of the distributed loads with θ = 90° and φ = 90° angular misalignment (case-B in Fig. 3.9c), using three-phase

excitation. In this case, for PDL = 5.4 mW at d_{23} = 7 cm, the power source supplies 2.24 W to seven CMCD PAs with 49% efficiency to drive seven overlapping hex-PSCs. The calculated power loss in each PA during LC-tank deactivation/discharge for TDM is ~12 mW, which is negligible with respect to the PA output power. Finally, the received power before and after the Rx rectifier was 7.6 mW and 5.4 mW, respectively.

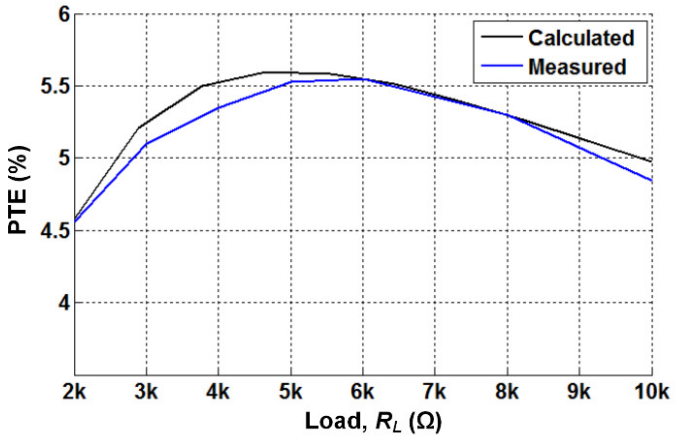

Fig. 3.10. Measured and calculated PTE vs. load variation at nominal distance d_{23} = 7 cm with no misalignment.

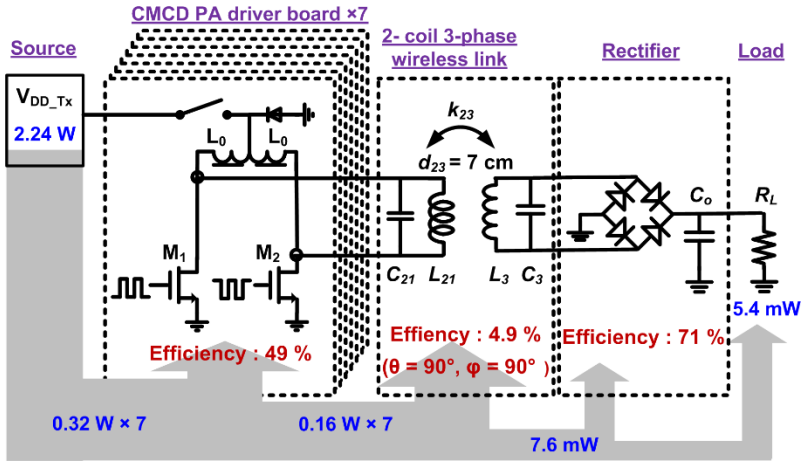

Fig. 3.11. Measured power flow for PDL = 5.4 mW at d_{23} = 7 cm and 90° misalignment of the Rx coil (case-B).

IV. WIRELESSELY-POWERED HOMECAGE SYSTEM (ENERCAGE-HC) FOR LONG-TERM BEHAVIORAL EXPERIMENTS

4.1 Wirelessly-Power Homecage for Long-Term Behavioral Experiments

In this chapter, a wirelessly-powered homecage system, called the EnerCage-HC, that is equipped with multi-coil wireless power transfer, closed-loop power control, optical behavioral tracking, and a graphic user interface (GUI) is presented for longitudinal electrophysiology and behavioral neuroscience experiments. The EnerCage-HC system can wirelessly power a mobile unit attached to a small animal subject and also track its behavior in real-time as it is housed inside a standard homecage. The EnerCage-HC system is equipped with one central and four overlapping slanted wire-wound coils (WWCs) with optimal geometries to form 3- and 4-coil power transmission links while operating at 13.56 MHz. Utilizing multi-coil links increases the power transfer efficiency (PTE) compared to conventional 2-coil links and also reduces the number of power amplifiers (PAs) to only one, which significantly reduces the system complexity, cost, and heat dissipation. A Microsoft Kinect installed 90 cm above the homecage localizes the animal position and orientation with 1.6 cm accuracy. Moreover, a power management ASIC, including a high efficiency active rectifier and automatic coil resonance tuning, was fabricated in a 0.35-μm 4M2P standard CMOS process for the mobile unit.

4.1.1 EnerCage-HC System Architecture

Fig. 4.1 shows a rendered view of the proposed EnerCage-HC system. The square-shaped center-WWC (L_1) at the bottom of the cage can directly form a 3-coil power transmission links with two coils (L_3, L_4) that are embedded in the mobile unit when the subject is located in the center of the cage. All other WWCs (L_{21}~L_{24}) are open-circuit. L_1 can also form a 4-coil link with one of the triangular-shaped overlapping slanted WWCs (L_{21}~L_{24}) when the subject is located near a corner of the homecage by

shorting that particular WWC with a resonant capacitor to form a series high-Q LC-tank. The sizes of the central and triangular WWCs are d_1 and d_2, respectively, and the tips of the triangular WWCs are elevated by h_2.

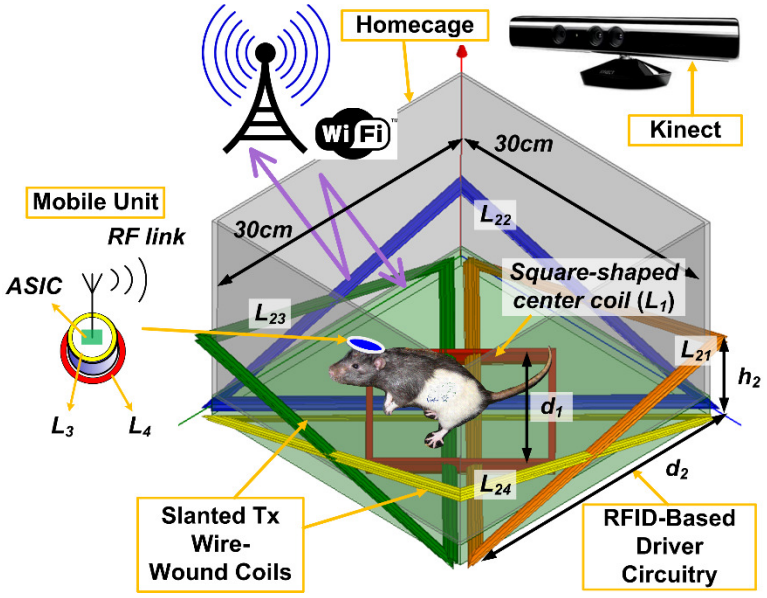

Fig. 4.1. 3D rendered view of the EnerCage-HC system with one square-shaped WWC at the bottom of the homecage and four overlapping slanted triangular WWCs on the corners. A custom ASIC receives power in the mobile unit and generates a stable supply for the sensing blocks and bidirectional RF data link. Animal position and orientation are tracked in real-time by a Microsoft Kinect.

In this system, multi-coil resonance-based inductive link not only increases the PTE compared to similar sized 2-coil links but also reduces the required number of power amplifiers (PA) to only one, which in turn reduces the system complexity, cost, and dissipated heat. Hence, only L_1 is driven by a class-C PA at f_p = 13.56 MHz, and L_{21}~L_{24} simply form high-Q LC-tanks. The PA is driven by an RFID reader (TR7960, Texas Instruments, Dallas, TX). The CPCL changes the PA supply voltage (V_{DD_Tx}) based on the information it receives about the mobile unit rectifier output voltage, V_{RECP} in Fig. 2, which is back telemetered via load shift keying (LSK) by shorting the L_4C_4-tank [37]. In this prototype, in order to monitor the system operation, V_{RECP} is also divided down, digitized, and wirelessly sent back to the central PC station by the mobile unit MCU and its built-in 2.4 GHz transceiver. This data is used for monitoring the mobile unit

operation and ensuring the EnerCage-HC system functionality. The central PC station is also responsible for processing the Kinect images to detect and report the animal position in each EnerCage-HC in real time. This information is then used to switch L_{21}~L_{24}.

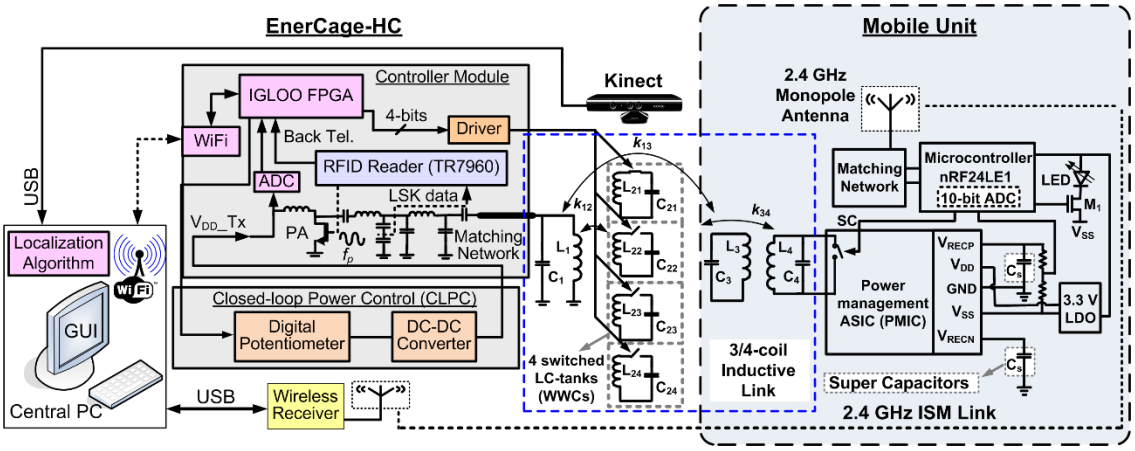

Fig. 4.2. Block diagram of the EnerCage-HC system for automated, high throughput, and long-term awake animal experiments in a standard homecage. The controller unit has an FPGA to process the position data from the PC and activate the WWCs in a way that they form 3- and 4-coil power transfer links based on the animal position. The PA output power is dynamically controlled in a closed loop based on the received power at the mobile unit. All the acquired information and system operating status are wirelessly transmitted to the PC station. The mobile unit on the animal body receives power inductively, generates a stable supply voltage through a power management ASIC, and communicates with the RFID reader via load shift keying (LSK). An LED blinking at 50 Hz with 4% duty cycle helps with 2D/3D Kinect localization and indicates both the animal location and orientation (i.e. where it is heading) inside the homecage.

Fig. 4.2 shows a detailed block diagram of the prototype EnerCage-HC system. The stationary unit is composed of a coil array (L_1, L_{21}~ L_{24}), a controller module, CPCL, a Microsoft Kinect® for optical tracking, and a central PC station with a graphical user interface (GUI). A field-programmable gate array (FPGA) receives the animal coordinates from the PC via a WiFi link, and use them to close- or open-circuit $L_{21}C_{21}$~$L_{24}C_{24}$ tank circuits. The RFID reader not only drives the class-C PA, but also recovers the back telemetry (BT) data from the PMIC. The V_{DD}_Tx is dynamically controlled by the CPCL from 4.5 V to 20 V in 256 steps based on the BT data to compensate for any coil coupling and loading variations [37]. In the EnerCage-HC system, 1-bit BT data is used to increase or decrease the V_{DD}_Tx. The received BT pulses

indicate that the received power in the mobile unit is sufficient, where the coupling between stationary and mobile unit is strong enough. The received BT pulses are oversampled by the FPGA to decrease the V_{DD}_Tx at the rate of 320 steps/s by controlling a digital potentiometer (AD5160) in the feedback loop of the DC-DC converter (LT1370). In the absence of BT pulses, the FPGA increases the V_{DD}_Tx at the same rate [37].

The mobile unit, shown on the right side of Fig. 4.2, is equipped with the PMIC, two super-capacitors, a 3.3 V low dropout regulator (LDO), an LED tracer, and an MCU (nRF24LE1, Nordic Semiconductor, Norway). The PMIC includes two active rectifiers to generate both positive V_{RECP} and negative V_{RECN} for bipolar stimulation [92], two LDOs to generate V_{DD} = 2 V and V_{SS} = -2 V, an automatic resonance tuning (ART) block, and LSK circuitry. An off-chip LDO is used to generate a separate 3.3 V supply voltage for the MCU. V_{RECP} is divided by two and digitized by the MCU built-in 10-bit ADC. When V_{RECP} is higher than 2.3V, the MCU sends narrow pulses to the PMIC at 3 kHz, which are sharpened (~0.4 μs) before shorting the L_4C_4-tank as briefly as possible to close the power control loop with minimal degradation of the PTE. The duty cycle of the BT short-circuit pulses is only 0.1% significantly minimize the power loss. The MCU also turns on/off transistor M_1 at 50 Hz with 4% duty cycle to blink a green LED for optical tracking of the mobile unit. Two 0.21 F super capacitors, following V_{RECP} and V_{RECN}, supply the mobile unit when the received power is interrupted by >80° tilting of the mobile unit or >18 cm coupling distance from the bottom of the homecage. These thresholds are experimentally determined when the PTE has reached a low level that even the maximum PA power in the EnerCage-HC system (7 W) is not sufficient to provide enough power to the mobile unit.

All acquired information, such as V_{RECP}, V_{DD}_Tx, and system operating status e.g. WiFi and MCU 2.4 GHz link connectivity, along with the Kinect images are collected by the central PC from each EnerCage-HC system to be used in the signal/image processing

algorithm and the GUI. The subject coordinates are sent from the PC to the FPGA using the User Datagram Protocol (UDP), while two-way communication through TCP/IP is used for monitoring the V_{DD}_Tx. The same link is used to reduce V_{DD}_Tx to 4.5 V when no mobile unit is detected in the homecage. The GUI displays a real time color video of the homecage, position of the animal and mobile unit in the cage, the total distance that the animal has traveled, the processed depth image, the active WWC, the connection status, V_{RECP}, and V_{DD}_Tx. The GUI can also save the acquired data in text and movie formats.

4.1.2 Multi-Coil Link Optimization for EnerCage-HC

Fig. 4.3 shows how utilizing 3/4-coil links eliminates the need to drive the triangular WWCs, while increasing the PTE by decoupling the loosely-coupled L_2-L_3 link from the source and load impedances [93]. When the mobile unit is in the center of the homecage, only L_1 is driven to form a 3-coil link, while the other WWCs are open-circuit. The PTE of a 3-coil link can be found from [22].

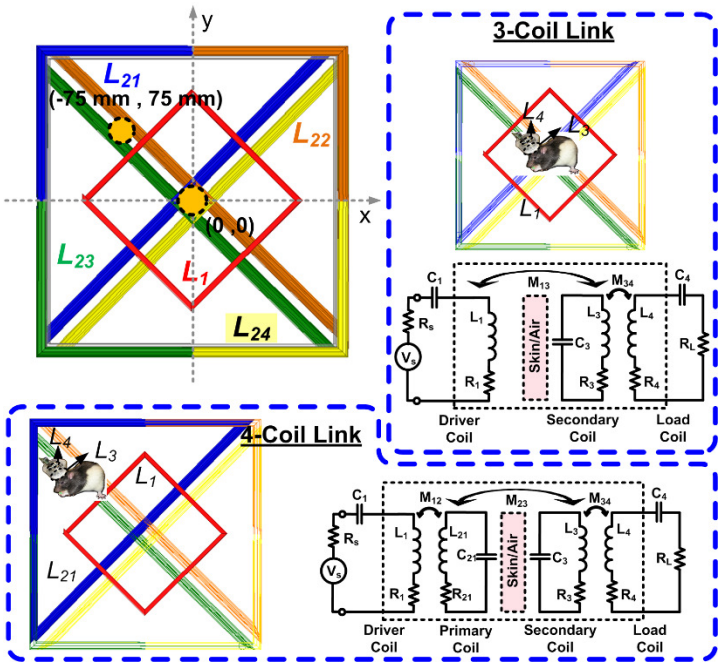

Fig. 4.3. WWC switching to form 3- and 4-coil inductive links with the mobile unit while only driving L_1 (inactive coils are light colored).

$$\eta_{3-coil} = \eta_{13} \cdot \eta_{34} = \frac{(k^2_{13} Q_1 Q_3) \cdot (k^2_{34} Q_3 Q_{4L})}{[(1 + k^2_{13} Q_1 Q_3 + k^2_{34} Q_3 Q_{4L}) \cdot (1 + k^2_{34} Q_3 Q_{4L})]}. \quad (4.1)$$

However, when the mobile unit is on the corners of the cage, the closest WWC (L_{21}~L_{24}) is shorted with a capacitor, which resonates at 13.56 MHz with the Tx, to form a 4-coil link. In a 4-coil link, the PTE can be written as [22].

$$\eta_{4-coil} = \eta_{12} \cdot \eta_{23} \cdot \eta_{34} \quad (4.2)$$
$$= \frac{(k^2_{12} Q_1 Q_2) \cdot (k^2_{23} Q_2 Q_3) \cdot (k^2_{34} Q_3 Q_{4L})}{[(1 + k^2_{12} Q_1 Q_2) \cdot (1 + k^2_{34} Q_3 Q_{4L}) + k^2_{23} Q_2 Q_3] \cdot [1 + k^2_{23} Q_2 Q_3 + k^2_{34} Q_3 Q_{4L}]}$$

The quantitative model and comprehensive circuit-based analysis describing the power transmission in 4-coil inductive links are described in [93] and [22]. The WWC geometries are optimized to provide homogeneous PTE in the worst case coil misalignments.

To reduce the size and weight of the mobile unit, which is carried in the headstage or a backpack, the diameter and width of L_3, i.e. D_{o3} and W_3, were limited to 2.5 cm and 0.64 mm, respectively, to be about the size of a U.S. quarter. Under the 300 Ω loading condition, which is corresponding to 24 mW of power consumption in the mobile unit, to maximize Q_3 for L_3, n_3 = 2 was chosen based on the HFSS simulations. The 24 mW power was chosen in this prototype as a level that is sufficient for the majority of state-of-art neural recording and stimulation devices [94]. The CPCL dynamically controls the V_{DD}_Tx to compensate for any load variations in the mobile unit. In order to embed the Tx coils inside the body of the homecage the width of the wire used in the Tx coils was limited to the thickness of the homecage. The AWG10 (W = 2.59 mm) wire was chosen for L_1 and L_{21}~L_{24} to achieve the highest Q. Fig. 4a shows the HFSS simulation results of Q_1 and Q_2 vs. f_p for $n_{1,2}$ = 1 turn and 2 turns. In these simulations, L_1 was square shaped

with an estimated d_1 = 19 cm, and L_2 had an isosceles triangular shape with d_2 = 30 cm and h_2 = 7 cm (see Fig. 4.1). L_1 has a square shape to increase its overlap area with L_{21}-L_{24}, which is directly proportional to their coupling coefficient. It is clear from these simulations that at f_p = 13.56 MHz in the industrial-scientific-medical (ISM) band, n_1 = $n_{21\text{-}24}$ = 1 provides higher Q_1 and Q_2.

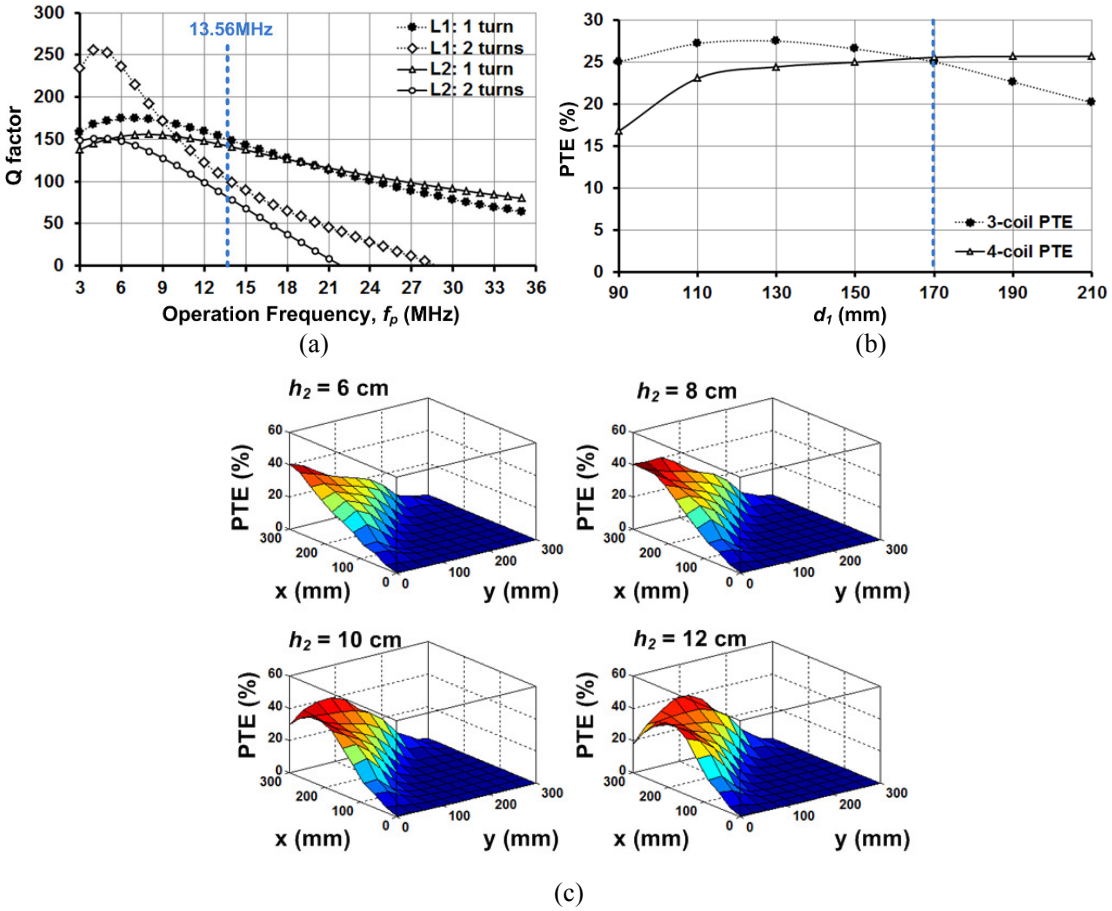

Fig. 4.4. Simulation results of 3/4-coil link optimization for the EnerCage-HC system: (a) Q-factor vs. f_p for different number of turns in L_1 and L_2, (b) optimal L_1 geometry for homogeneous 3/4-coil PTE, and (c) 4-coil PTE distribution on the corner of the homecage with h_2 = 6 cm, 8 cm, 10 cm, and 12 cm at a nominal height of d_{23} = 7 cm.

In optimizing d_1, we noticed that the common optimization algorithm in [22] leads to a smaller d_1 with higher PTE at the center of L_1 in the 3-coil arrangement. However, that will also reduce the overlap between L_1 and L_{21}~L_{24} coils, resulting in lower k_{12} and lower PTE in the 4-coil arrangement. Moreover, the powered area in the

center of the homecage is also reduced by decreasing d_1, negatively affecting the homogeneity of the PTE across the homecage. Fig. 4.4b shows the simulated 3- and 4-coil PTE vs. d_1 at L_2-L_3 nominal distance of d_{23} = 7 cm when the Rx coil was located at the center of the homecage (0, 0) for the 3-coil and in the center of a triangular WWC (-75 mm, 75 mm) for the 4-coil link (see orange spots Fig. 4.3). Starting from 9 cm, as d_1 becomes larger, k_{12} is increased and PTE for the 4-coil link also increases. However, if d_1 becomes much larger than its optimal size for the 3-coil link, its PTE decreases due to reduced k_{13}. To create a homogeneous PTE at the coils' switching points, d_1 was selected as 17 cm, based on the simulations in Fig 4b.

To determine the L_2 triangular geometry, d_2 was chosen 28 cm, slightly less than the length of each side of the homecage (30 cm), to offer maximum overlap with L_1 but avoid overlapping among four WWCs at the center of the homecage considering the thickness of the coil wires (see the top view in Fig. 4.3). h_2 is key in determining the distribution of the 4-coil PTE at the corners of the homecage, where the animal tends to stand up and create a worst case scenario for power transmission from a central WWC at the bottom of the cage. Fig. 4.4c shows the simulated distribution of the 4-coil PTE inside the homecage for the nominal height of d_{23} = 7 cm when h_2 is changed from 6 cm to 12 cm in the nominal loading condition of 300 Ω. It can be seen that by increasing h_2 the high PTE region tends to move toward the center of the cage, while PTE at the corners drop. Therefore, to achieve a homogeneous PTE distribution at the corners of the homecage, h_2 = 8 cm was chosen, the height at which the peak PTE starts to drop. The PTE distribution is affected by L_3 and L_4 geometries and orientations, but not by the loading condition. The PTE in the EnerCage-HC is reduced if the loading condition is out of the nominal condition. However, the CLPC dynamically adjusts the Tx power to ensure that the headstage receives sufficient power even in suboptimal loading or positioning conditions.

The geometry of L_4 was optimized as the last step for d_{23} = 7 cm, based on the coil optimization procedure in [22]. The nominal loading was considered to be 300 Ω, corresponding to ~24 mW power consumption in the mobile unit. L_3 and L_4 are concentric. The inductance values of L_3 and L_4 are decided by their number of turns and diameter. L_4 has a lower Q-factor compared to L_3 because the diameter of the litz wire in L_4 is much smaller than the solid wire used in L_3. Also L_4 has higher number of turns because according to our coil design, despite its smaller size, it should have a higher inductance [22]. The optimal EnerCage-HC coil geometries are summarized in Table 4.1. The coil design is optimized for the most common conditions, i.e. a horizontal mobile unit at a nominal height of 7 cm above the bottom of the cage. The other conditions will be taken care of by the CPCL, which dynamically adjusts the Tx power to ensure the mobile unit functionality.

TABLE 4.1. COIL SPECIFICATIONS FOR THE PROTOTYPE ENERCAGE-HC SYSTEM

Parameters	Value
Tx wire-wound coil (L_1)	Diameter = 17 cm Wire width = 2.59 mm (AWG10) Number of turns = 1 Inductance = 0.716 µH Quality factor = 150.3
Tx wire-wound coil (L_2)	d_2 = 28 cm, h_2 = 8 cm Wire width = 2.59 mm (AWG10) Number of turns = 1 Inductance = 0.890 µH Quality factor = 154
Rx wire-wound coil (L_3)	Diameter = 2.5 cm Wire width = 0.64 mm (AWG22) Number of turns = 2 Inductance = 0.48 µH Quality factor = 136
Rx Litz wire-wound coil (L_4)	Diameter = 1 cm Wire diameter = 0.25 mm Number of turns/strands = 6/44 Inductance = 5.8 µH Quality factor = 12
L_2-L_3 nominal distance (d_{23})	7 cm
Nominal load (R_L)	300 Ω (~24 mW)
Operation frequency (f_p)	13.56 MHz

Figs. 4.5a and 4.5b compare the simulated PTE distribution inside the homecage at a nominal height of 7 cm when a single large WWC encompasses the bottom of the cage (e.g. [7]) vs. our proposed 5-coil design, shown in Fig. 4.1, respectively. The conclusions from these simulations are: 1) The PTE in the corners of the EnerCage-HC is significantly higher than the single WWC design, thanks to the overlapping slanted WWCs (L_{21}~L_{24}), both when the mobile unit is held horizontally and vertically, which happen when the animal is walking on the bottom or climbing the walls of the homecage, respectively; 2) The average PTE in the EnerCage-HC is 27.8%, which is three times higher than the 9.2% average PTE of a single WWC; 3) The PTE distribution in the EnerCage-HC is considerably more homogeneous than the single WWC because the maximum PTE variation inside the homecage is 23.8% of the average PTE in the EnerCage-HC vs. 56.5% in the single WWC homecage.

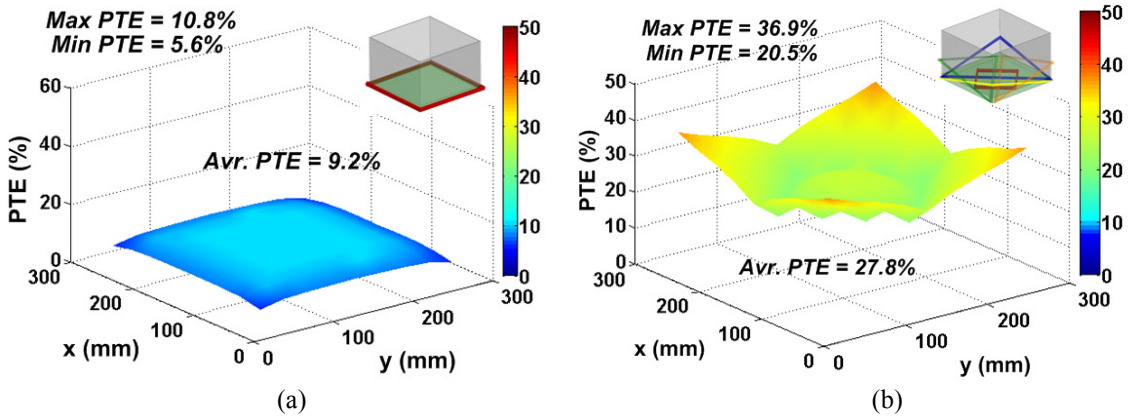

Fig. 4.5. Simulation results of the PTE distribution inside the homecage at the nominal height of d_{23} = 7 cm for, (a) a single WWC [12] and (b) the proposed EnerCage-HC system.

4.1.3 2D/3D Optical Animal Subject Tracking

Using Kinect provides a unique opportunity to utilize both the IR depth (3D) and RGB (2D) cameras for tracking the animal subject. Another advantage of an IR-based system is its ability to track subjects even in the dark environments, which is quite helpful when experimenting with nocturnal species that include the majority of rodents.

Moreover, utilizing both IR and RGB cameras in the EnerCage-HC, aided with an LED tracer on the headstage, enables recognition of the animal subject orientation (determining its head from tail), which is important in behavioral tracking [95][96].

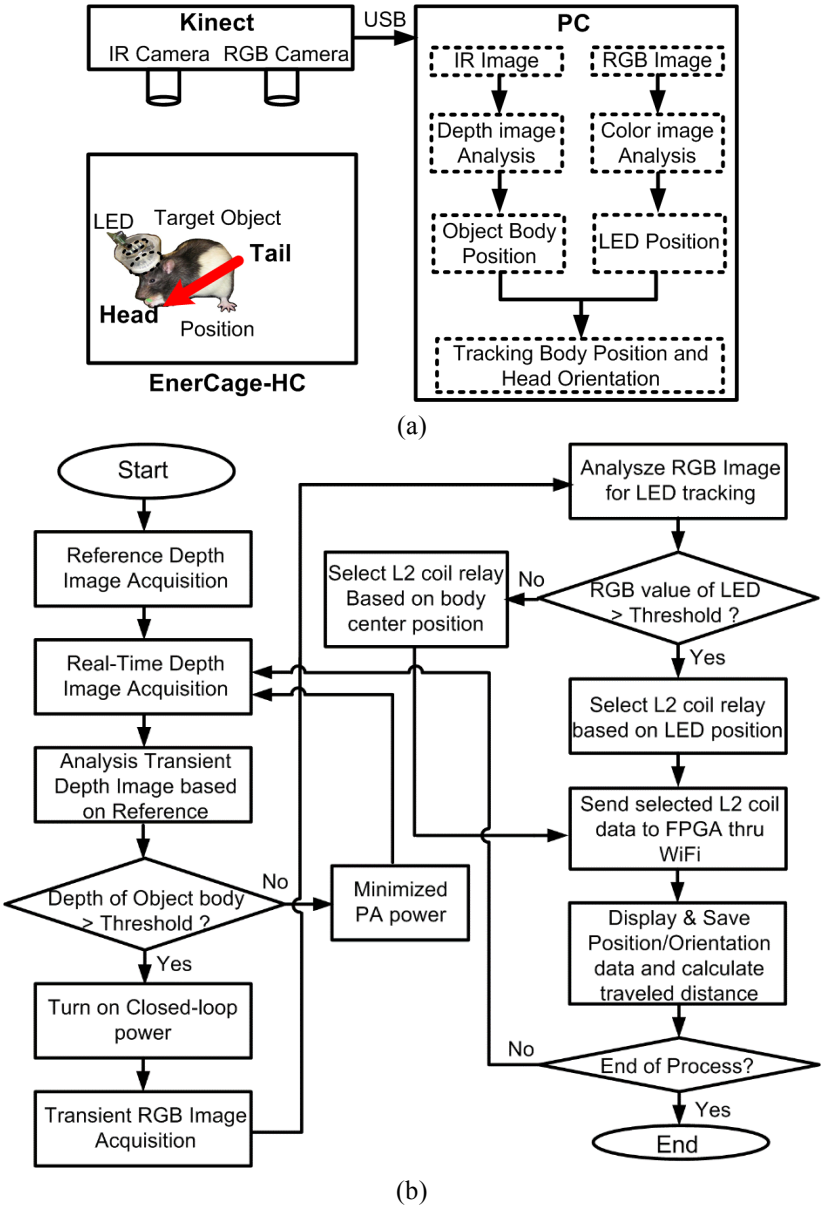

Fig. 4.6. Data flow diagram and flowchart of the tracking mechanism in EnerCage-HC. (a) EnerCage-HC system uses data from both RGB and IR images from the Kinect, and detects the head and body positions separately. (b) Flowchart of the software running on the PC shows how the RGB and IR images are used for real time animal tracking.

Fig. 4.6 shows the hardware and software diagrams of the tracking algorithm in the EnerCage-HC system. The Kinect was installed at ~90 cm above the homecage to easily cover the 30 × 30 cm^2 area of the homecage. The collected depth and RGB images from the Kinect were transferred to PC via USB, as shown in Fig. 4.6a. The real-time depth image from Kinect was compared to a reference depth image, taken when the animal subject was not present, to find the animal subject in the cage. The software algorithm projects the depth image voxels over a 2D plane, and indicates the areas that have higher value than a predefined detection threshold. Then, the center of the animal outline is found from the projected image to identify the center of the subject body. If the measured depth of the object is less than the threshold, the software concludes that the animal is not present in the cage, and reduces the PA power to its minimum by setting V_{DD}_Tx = 4.5 V to reduce the dissipated power.

When the algorithm finds the center of the subject body, it activates the CPCL to provide sufficient amount of power to the mobile unit. It then analyzes the RGB image to find the LED indicator. At startup, when the mobile unit is not powered and the LED is off, L_{21}~L_{24} are controlled based on the body position extracted from the depth image. When the LED indicator starts blinking, the position of the LED indicator is detected from the RGB image and combined with the center of the body to not only activate one of L_{21}~L_{24} coils but also indicate the subject orientation.

With more advanced image processing, we are trying to pinpoint the position of the rat head directly from Kinect the 3D image. When that algorithm is fully functional, there will be no need for an additional LED localization. By tracing the acquired positions, the accumulated distance that the subject has traveled can be calculated in real time. The process for automated tracking, shown in Fig. 4.6, takes ~50 ms, including the 30 Hz frame rate of the Kinect. It also depends on the performance of the central PC station. Considering relatively low speed of the animal subject movements within the homecage (30~70 cm/s) [97] and the presence of the super capacitors in the mobile unit,

the tracking mechanism in the EnerCage-HC is fast enough to provide the animal position for switching L_{21}-L_{24} to power the mobile unit. All of the acquired data during the experiment is displayed on the PC screen, and saved in the PC station for post processing.

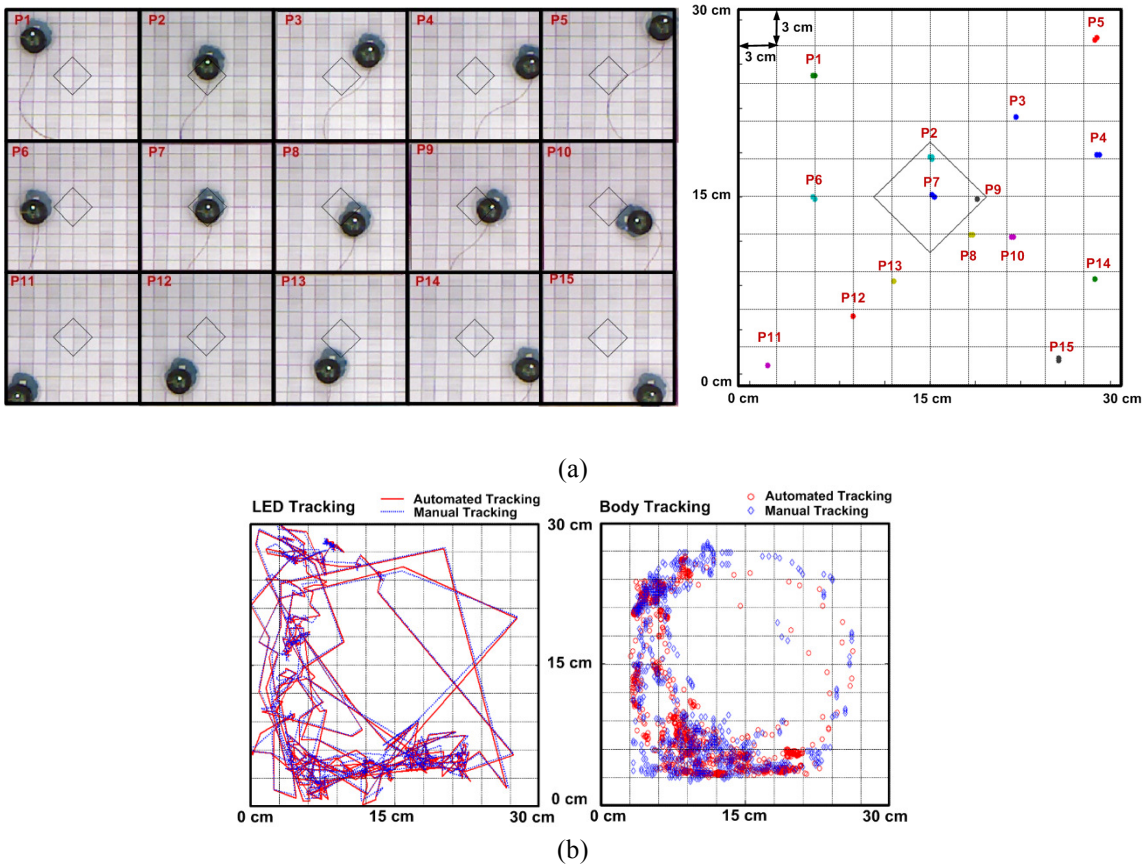

Fig. 4.7. Validation of the automated tracking in the EnerCage-HC system: (a) sample images of 15 random positions (P1-P15) for the LED tracking on the checker board during 3 min, and (b) automated tracking vs. manual tracking for a 20 min *in vivo* experiment (Left: LED and Right: body center tracking).

Fig. 4.7 compares the automated and manual tracking results within the EnerCage-HC. A checker board with 3 cm grid was used to manually place the mobile unit in a known position inside the homecage. Fig. 4.7a shows the images of 15 random mobile unit positions on the checker board compared with the automatic tracking data collected in 3 min at each position (P1 to P15). The maximum time jitter for the optical tracking was 20 ms in this test. The maximum position error was measured 1.6 cm near the corners, where the large viewing angle from the Kinect lens is the main source of

inaccuracy. Fig. 4.7b shows the comparison between automatic (red) and manual frame-by- frame (blue) tracking of a freely behaving rat (17 cm long) from the recorded video in an *in vivo* experiment, which details are presented in section 4.1.4. We randomly selected 20 min of the recorded experiment video, and manual tracking was performed by a human observer watching the recorded video to identify the position of the LED and center of body. It can be seen from Fig. 4.7b that the automated tracing of the LED indicator is in good agreement with manual tracking with maximum localization error of 1.3 cm. However, since determination of the manual body center is somewhat subjective, the automated and manual tracking results are not overlapping as well as the LED tracking. Nonetheless they show similar trends.

4.1.4 Measurement Results

To increase the overall power efficiency of the EnerCage- HC system and establish a communication link between mobile and stationary units for the CPCL, while maintaining small size and volume of the mobile unit, a custom PMIC was designed.

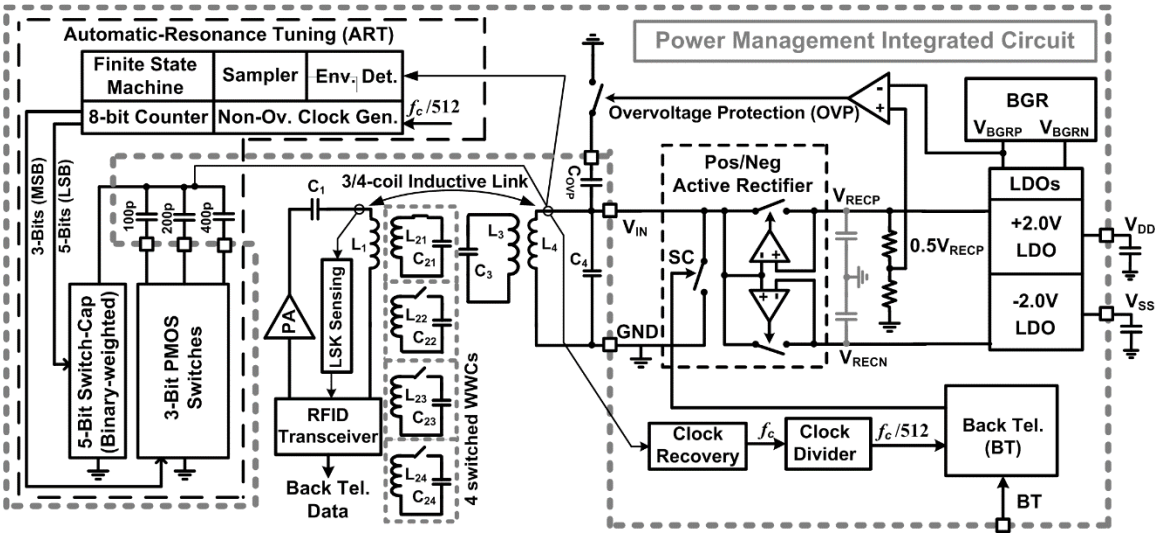

Fig. 4.8. Block diagram of the efficient power management integrated circuit (PMIC) in the mobile unit, which is equipped with automatic resonance tuning (ART) mechanism and back telemetry to dynamically tune the L_4C_4-tank at the 13.56 MHz carrier frequency and close the power control loop, respectively.

Fig. 4.8 shows the PMIC block diagram, along with its off-chip components that are presented outside the gray dashed box. The AC signal across the Rx L_4C_4-tank, which is tuned at f_p = 13.56 MHz, is rectified by the positive/negative rectifier. The rectifier outputs, V_{RECP} = 2.3 V and V_{RECN} = -2.3 V, are then applied to two LDOs, which create stable V_{DD} = 2 V and V_{SS} = -2 V. An automatic-resonance tuning (ART) block ensures that the L_4C_4- tank is always tuned at f_p = 13.56 MHz despite the effects of packaging, implantation, or animal proximity to large conductive objects, such as the transmitter coils.

Fig. 4.9 shows the mobile unit prototype including the PMIC, an nRF MCU, and an LED. The PMIC was fabricated in the TSMC 0.35-µm 4M2P standard CMOS process, and it occupies 3.5 mm^2 of silicon area. The mobile unit includes L_3 and L_4 coils, which specifications are given in Table I, at the bottom of the box, a small PCB with the PMIC wirebonded to a QFN package, and a separate PCB with nRF MCU, RF matching network, 2.4 GHz monopole antenna, and the LED indicator. The total weight of the mobile unit in this prototype was 16.2 g including the weight of the box, which was 9.1 g.

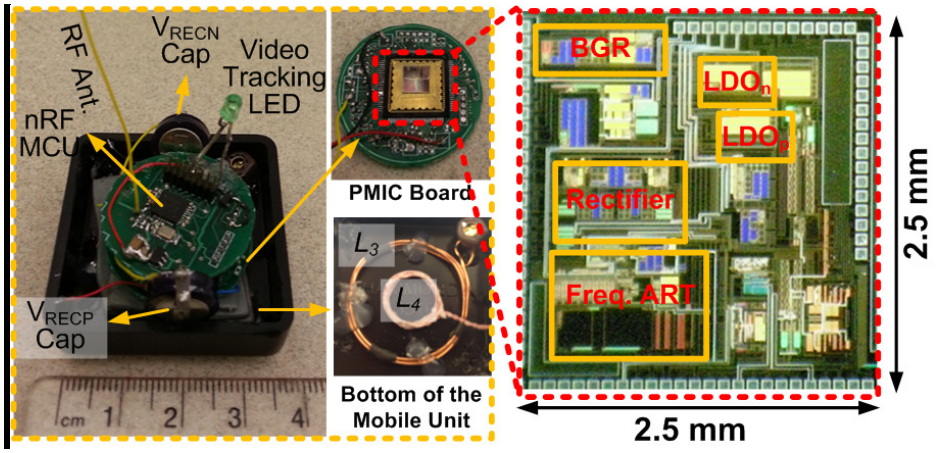

Fig. 4.9. The mobile unit prototype including the PMIC, an nRF MCU, and LED indicator. The PMIC was fabricated in TSMC 0.35-µm 4M2P standard CMOS process, occupying 3.5 mm^2.

Fig. 4.10 shows the measured PTE distribution between the Tx and Rx coils inside the EnerCage-HC at d_{23} = 7 cm based on the direct PTE measurement procedure in [22], using a network analyzer across the inductive links. The surface of homecage was

marked by a checker board with 3 cm resolution for the PTE measurements. At the corners, the maximum measured PTE was 36.3%, which matches very well with the simulated result in Fig. 5b. The lowest and average PTEs across the homecage were 16.1% and 21.9%, respectively. The efficiency of the PA was measured 81% at V_{DD}_Tx = 4.5 V, and gradually decreased to 63% at V_{DD}_Tx = 20 V, which is the maximum voltage in this prototype EnerCage-HC system.

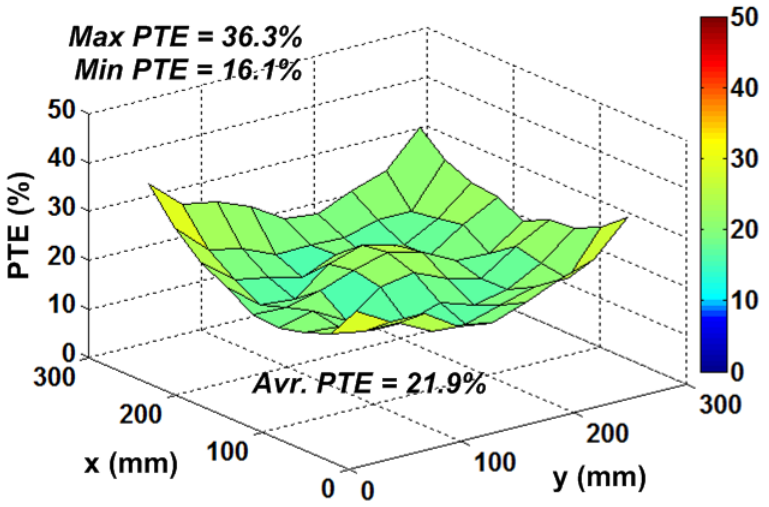

Fig. 4.10. Measured PTE distribution inside the EnerCage-HC

The maximum permissible exposure (MPE) to magnetic field strength based on the IEEE standard is $16.3/f_c$ (A/m), where f_c is in MHz, resulting in the equivalent maximum power density at 13.56 MHz to be 54.3 mW/cm^2 [98]. Since the WWC at the bottom of the EnerCage (L_1) has 17 cm × 17 cm = 289 cm^2 area, the maximum safe power transmission level would be 15.6 W. However, the maximum transmitted RF power in the current EnerCage-HC prototype is 4.4 W, and it only happens over a short period in the worst case scenario when the animal stands up. This is equivalent to a maximum power density of 15.2 mW/cm^2, which is well below the safety limit. Therefore, the EnerCage-HC system satisfies the IEEE standard with respect to safe level of human or animal exposure to radio frequency electromagnetic fields [46].

Fig. 4.11 shows the *in vivo* experimental setup for the EnerCage-HC prototype. The animal subject was a one-year- old rat weighting 300 g. The mobile unit was placed in the plastic box in Fig. 4.9 and attached to a special jacket, designed for rats. All experiments were conducted with the prior approval from the Institutional Animal Care and Use Committee (IACUC) at the Georgia Institute of Technology. During the experiment, the GUI reported the real-time video, V_{RECP}, $V_{DD\_}Tx$, and the LED/Body tracking information along with the rat body orientation and travelled distance. Water bottle and food dispenser were also placed in the homecage for the 7 hr and 20 min experiment, during which the rat was freely moving in the homecage.

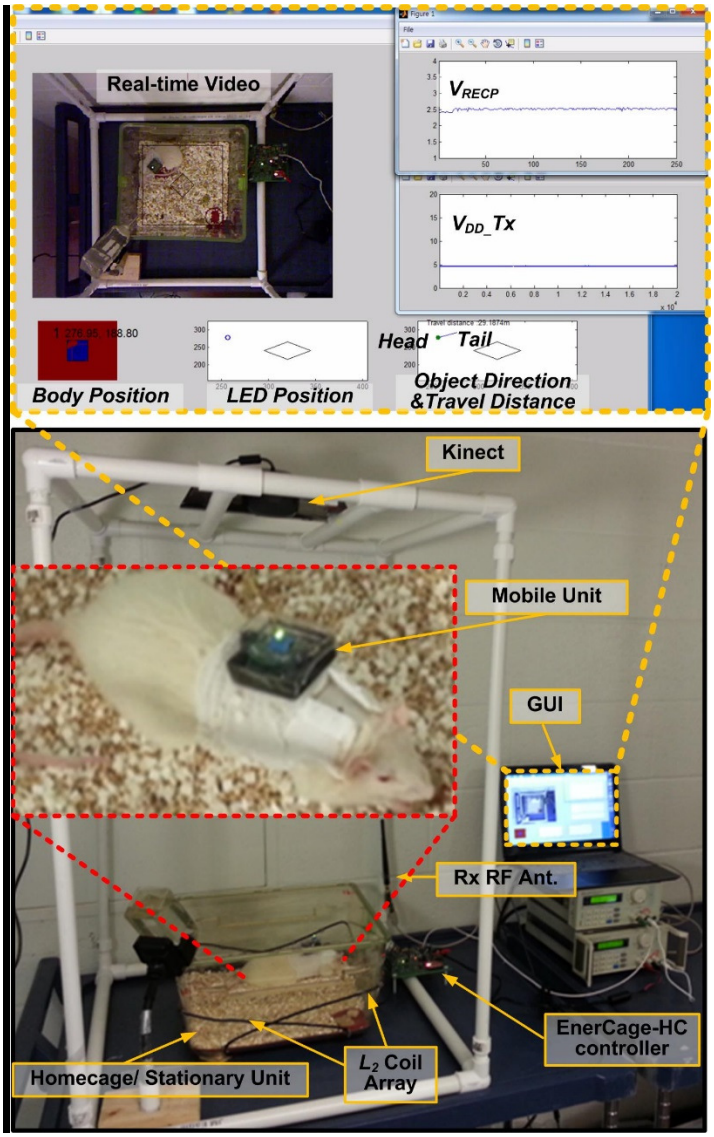

Fig. 4.11. *In vivo* experimental setup for the EnerCage-HC prototype. In this experiment, the rat was freely moving around the cage for 7 hour and 20 min.

Fig. 4.12 shows the measured V_{RECP} and V_{DD}_Tx during 7 hours and 20 min without any interruption. The EnerCage-HC continuously delivered 24 mW of regulated power to the mobile unit by maintaining V_{RECP} constant at 2.3 V, which was high enough for the LDO to generate a stable V_{DD} = 2 V, thanks to the CPCL module. The V_{DD}_Tx was dynamically adjusted by the CPCL module in the EnerCage-HC between 4.5 V and 20 V corresponding to the PA power consumption of 0.3 W to 7 W, depending on the coil separation, d_{23}. We should point out that the 7 W power consumption in the PA is the

worst case scenario of animal standing up, which is maximum coil separation or angular misalignment of the Rx coil. Fig. 4.12 inset shows that the CPCL increased V_{DD}_Tx, when the rat moved to low PTE areas or stood up on his hind limbs (t < 14817 s), and decreased V_{DD}_Tx when the mobile unit was close to the homecage surface or high PTE areas (t > 14817 s). The mobile unit received stable power inside the homecage during 7:20 hr of continuous operation regardless of the animal movements, proving the functionality of the EnerCage-HC.

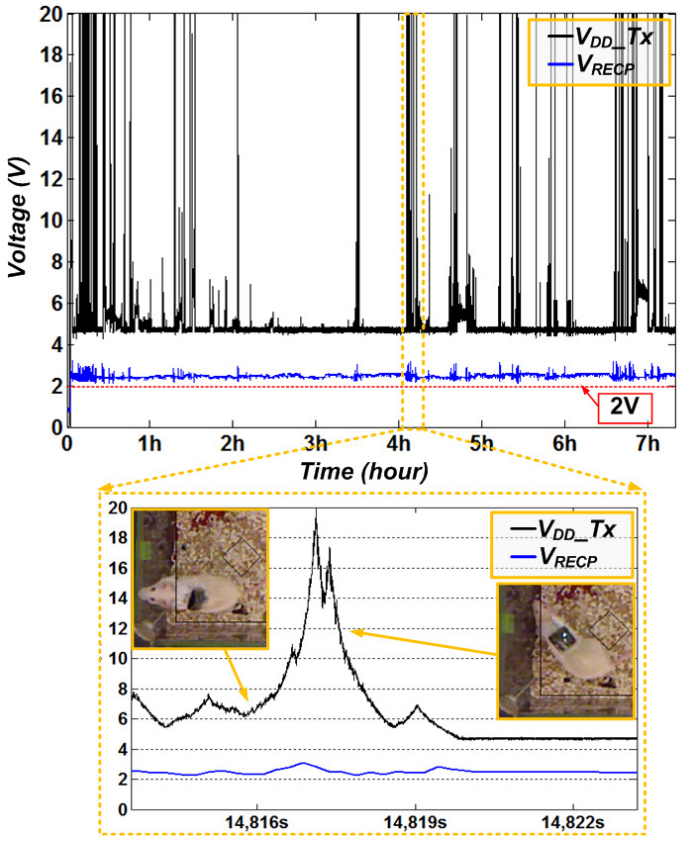

Fig. 4.12. *In vivo* experimental results showing the mobile unit positive rectifier voltage, V_{RECP}, and the transmitter PA supply voltage, V_{DD}_Tx, during ~7 hrs. The CLCP increased the transmitted power, which is in proportional to V_{DD}_Tx, when the rat moved to low PTE areas or stand up as shown in inset t < 14817 s, and decreased V_{DD}_Tx when the mobile unit was close to the homecage surface or high PTE areas as shown in the inset t > 14817 s.

Fig. 4.13 shows the measured tracking information including the position and orientation of the animal inside the homecage during the 7:20 hr *in vivo* experiment. Fig. 4.13a shows the automated position data for the LED indicator on the mobile unit. The heat map shows how long the animal spent in a certain location. The statistical result for

the rat's orientation based on the automated LED/body tracking data is shown in Fig. 4.13b. Since most of the time the rat moved across the left corners, marked A and B in Fig. 4.13a, the orientation of the rat shows peaks in those directions. The rat's travel distance based on the LED tracking data is shown in Fig. 4.13c, which indicates that the rat moved about 69.6 m in the homecage during the experiment.

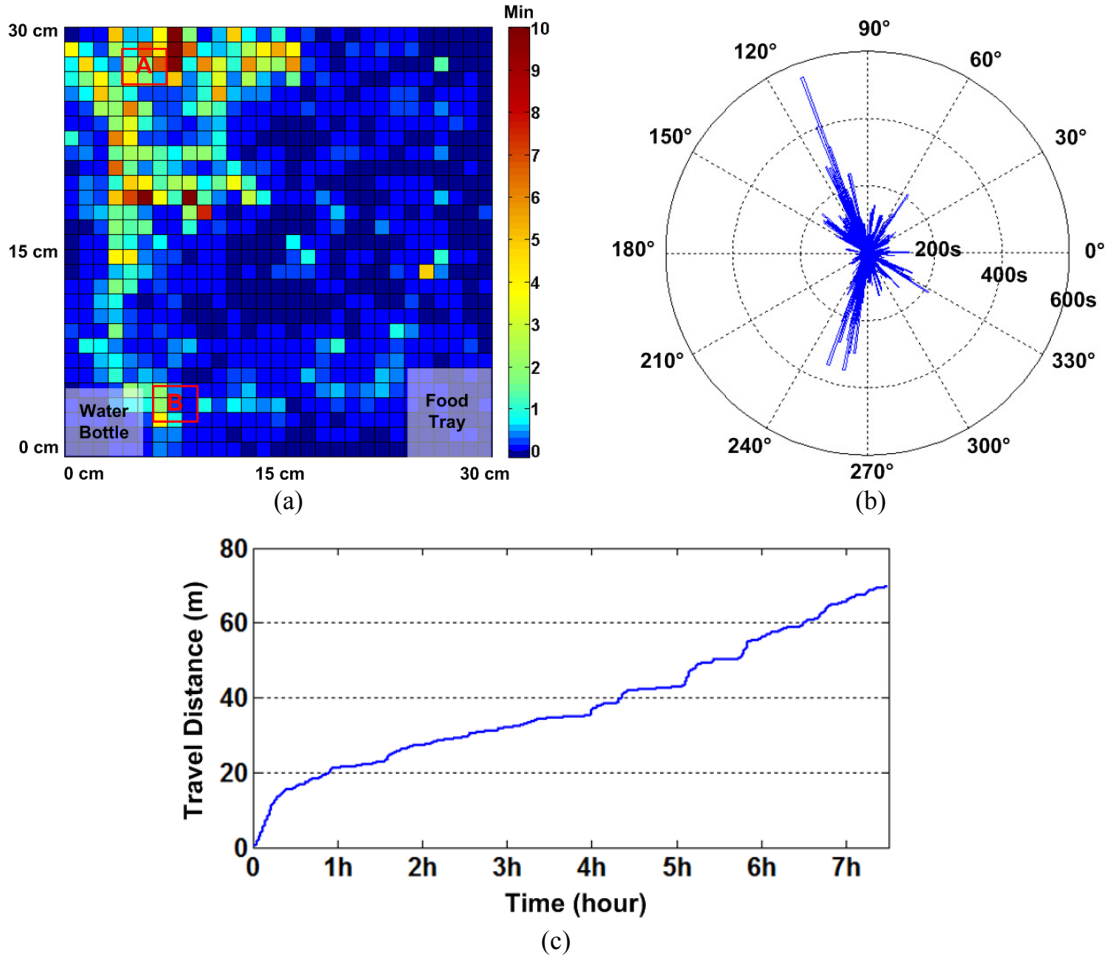

Fig. 4.13. *In vivo* experimental results showing the automated tracking for the LED/body during ~7 hrs of the experiment inside the homecage: (a) the position of the mobile unit based on the LED tracking, (b) the distributed time of the rat's orientation based on the LED/body tracking, and (c) the travel distance of the rat in the homecage.

Table 4.2 compares the EnerCage-HC system with the previous attempts at developing wirelessly-powered systems for behavioral experiments on small freely behaving animals. The presented EnerCage-HC, 1) provides the largest wirelessly-powered area per one PA with the proposed slanted multi-coil WWC arrangement, 2) is

the only system equipped with accurate 2D/3D animal subject tracking, not only for real time coil switching but also for the behavioral analysis of the subject, 3) compared to [85], the customized mobile unit provides higher average power efficiency with smaller Rx coils at 7 cm distance, thanks to its ART mechanism. It also ensures safe operation against frequent over voltage situations along with robust and smooth closed-loop control during long-term *in vivo* experiments, improving the quality of the collected bio-signal and behavioral data.

TABLE 4.2 BENCHMARKING WIRELESSLY-POWERED SYSTEMS FOR BEHAVIORAL EXPERIMENTS

Year of publication	2012 [40] 2014 [85]	2014 [43]	2013 [44]	2014 [99]	2014 [46]	**This work**
Frequency	13.56 MHz	13.56 MHz	1.55 MHz	2.457 MHz	13.56 MHz	**13.56 MHz**
Coil coupling	3-/4- coil	4 coil	2 coil	4 coil	2 coil	**3/4 coil**
Tx coil type	PSC array	PSC array	PSC array	WWC	PSC	**WWC**
Number of power amplifiers	27	1	16	1 or 2	1	**1**
Powered experimental area	51.5 × 45 cm^2	30 × 30 cm^2	45 × 26 cm^2	15 × 20 cm^2	18 × 34 cm^2	**30 × 30 cm^2**
Rx power	20 mW	*115 mW	~ 22 mW	N/A	1.7 mW	**24 mW**
Rx coil diameter (L_3, L_4)	4 cm, 2.5 cm	4.2 cm, 1.1 cm	4 cm	1.9 cm, 1.6 cm	1.2 cm	**2.5 cm, 1 cm**
Efficiency (Distance)	~ 21% (7cm)	*76% (4cm)	**7.2% (10 cm)	***10% (7 cm)	17% (3 cm)	**21.9% (7cm)**
Animal subject tracking (Resolution)	Position (N/A)	N/A	Position (N/A)	N/A	Position (1 cm)	**Position & Orientation (1.6 cm)**
Tracking Method	Magnetic	N/A	Impedance	N/A	Magnetic Field	**Infrared /RGB**
Closed loop control	Yes	N/A	N/A	Yes	Yes	**Yes**
Automatic resonance tuning	N/A	N/A	N/A	N/A	N/A	**Yes**
In vivo experiment (duration)	Yes (1 hr)	N/A	N/A	Yes (N/A)	N/A	**Yes (7 hr 20 min)**

** Source resistance is 1 Ω.* *** Estimated* **** Single PA is used*

4.2 EnerCage-HC System for Inductive Powered Wireless Implantable Neural Recording (WINeR-7) System

4.2.1 *In Vivo* Experimental Setup

The EnerCage-HC system is also demonstrated by the *in vivo* experiment for a local field potential (LFP) and peripheral nerve recording using a wireless implantable neural recording system (WINeR-7) as shown in Fig. 4.14. The WINeR-7 system equips 8-channel dual slope charge sampling (DSCS) analog front-end (AFE) architecture, which create a pseudo-digital pulse width modulation (PWM) pulse instead of the conventional analog-to-digital converter (ADC) [101], and consumed 51.4 mW from a 1.8 V/4.2 V supply [102].

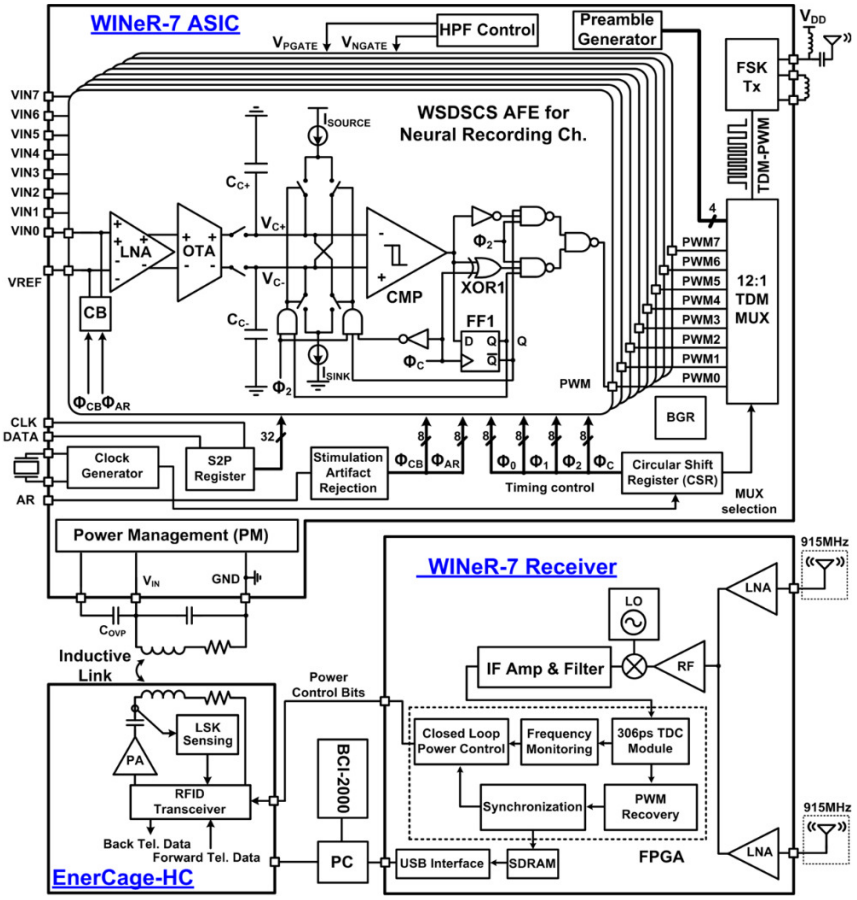

Fig. 4.14. Block diagram of the 8-channel DSCS-based wireless integrated neural recording (WINeR-7) system. Top: the transmitter unit with WINeR-7 ASIC and a few off-chip components, Bottom: the receiver unit and EnerCage-HC [102].

The *in vivo* experimental setup of WINeR-7 headstage for long-term LFP recording is shown in Fig. 4.15 along with the 2D/3D optical animal tracking. A custom designed 16-channel multi-electrode array (Tucker Davis Technologies; Alachua, FL) was stereotactically implanted in a male Sprague-Dawley rat (>350 g; Charles River Laboratories; Wilmington, MA) for chronic simultaneous recording the local field potentials (LFP) from the CA1 and CA3 areas of the hippocampus. All work was conducted in accordance with the National Institutes of Health *Guide for the Care and Use of Laboratory Animals* and approved by Emory University's Institutional Animal Care and Use Committee.

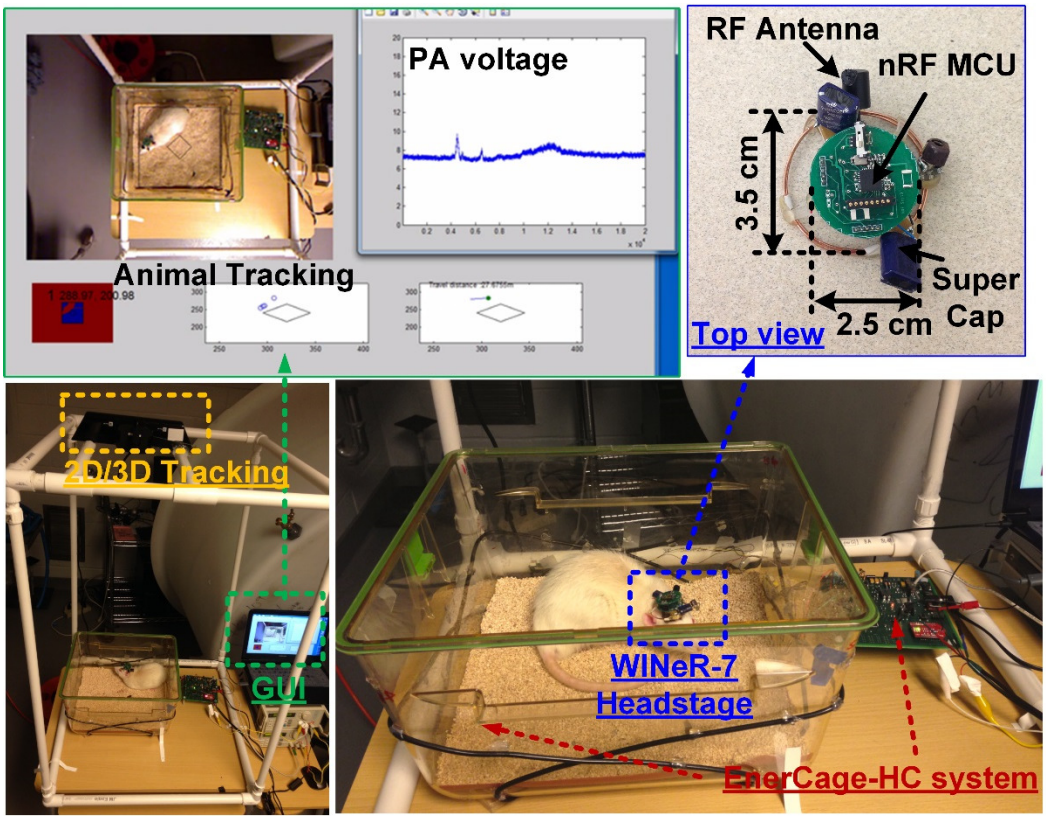

Fig. 4.15. In vivo test setup of WINeR-7 headstage for EnerCage-HC system.

The EnerCage-HC system successfully delivered the constant power of 51.4 mW for awake and freely moving animal while the neural recording was performed by the WINeR-7 headstage. In this system, the closed-loop inductive power control with optimal

coil design provides high PTE while maintaining the received power at the headstage constant despite animal movements.

Another *in-vivo* test is performed to verify the functionality of the EnerCage-HC system for implantable recording device inside the animal body. Fig. 4.16 shows the rendering view of the wirelessly-powered recording system for peripheral nerve and actual *in vivo* experimental setup of the implanted WINeR-7 inside the EnerCage-HC for peripheral nerve recording in University of Texas, Rio Grande Valley.

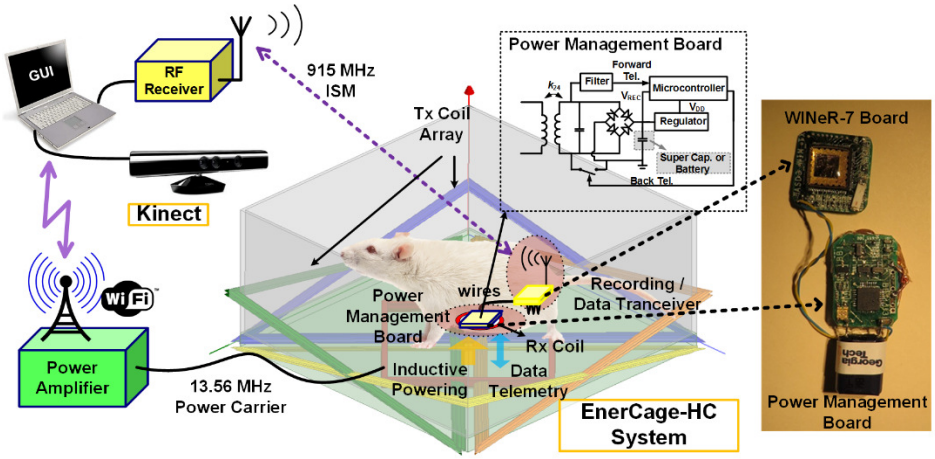

(a)

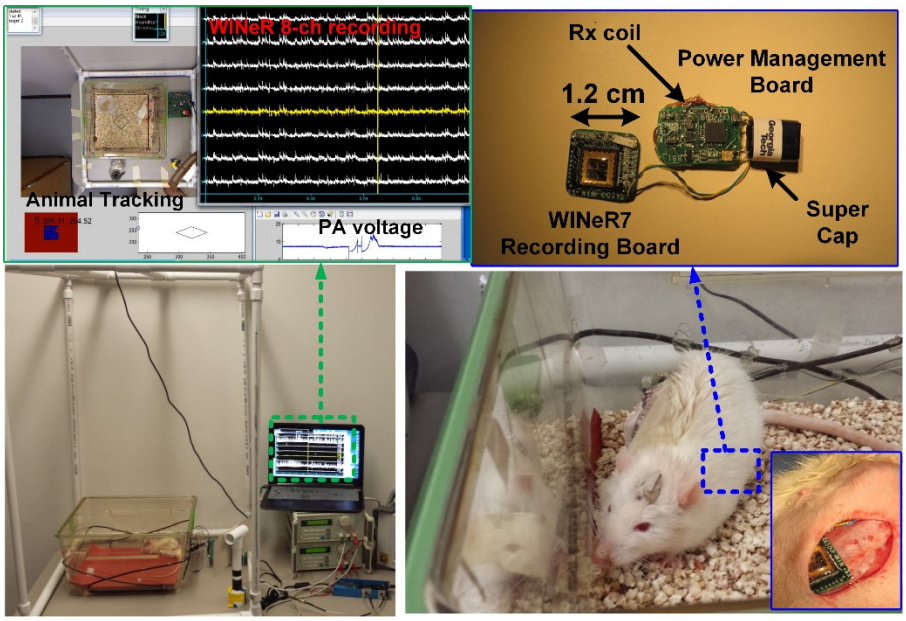

(b)

Fig. 4.16. (a) Rendering view of the wirelessly-powered recording system for peripheral nerve, and (b) in vivo experimental setup of the implanted WINeR-7 with EnerCage-HC system in UT RGV.

The implanted devices for wirelessly-powered recording system for peripheral nerve is divided into two parts, which are a power management board implanted near the belly of the animal subject and a recording/data transceiver board near the nerve of the animal subject. The power management board is equipped with an Rx coil, a rectifier, a regulator, a super capacitor/battery, a microcontroller for back telemetry communication as shown in Fig. 4.16(a). The microcontroller can send the back telemetry data using load-shift keying (LSK) technique. In this experiment, the V_{REC} information is sent to the EnerCage-HC to control the transmitted power for the closed-loop power control. All work was conducted in accordance with the National Institutes of Health *Guide for the Care and Use of Laboratory Animals* and approved by University of Texas, Rio Grande Valley's Institutional Animal Care and Use Committee. The power management board was implanted near the belly of the rat, and continuously received 51.4 mW of regulated power during the *in vivo* experiment, while a Kinect® installed 90 cm above the homecage tracked the animal position and orientation to create an automated enriched environment inside standard homecage for long-term electrophysiology experiments. The EnerCage-HC system combined with the WINeR-7 enables neuroscientists to eliminate cables from their electro-physiology experiments without adding the burden of carrying large battery payloads on the freely behaving animal subjects, or shortening the duration of the trial.

V. WIRELESS IMPANTABLE NEURAL RECORDING AND STIMULATION (WINERS-8) SYSTEM IN ENERCAGE-HC SYSTEM

In this chapter, a completed inductively-powered wireless implantable neural recording and stimulation system, called WINeRS-8, is presented in Fig. 5.1 for longitudinal electrophysiology and behavioral neuroscience experiments fully compatible with the EnerCage-HC system described in chapter IV. The WINeRS-8 system equips 32-channel adaptive averaging low noise analog front-end (AFE) with 10-bit successive approximation ADC (SAR-ADC), which is suitable for central and peripheral nerve recording applications. The amplified, filtered, and digitized bio-signal is transmitted through 433 MHz On-Off Keying (OOK) transmitter (Tx) with the data rate of 9.04 Mbps. The transmitted RF signal is detected by two individual software-defined ratio (SDR) receiver (Rx) to increase the directivity and coverage of the received RF signal over the experimental space, resulted in the reduced RF Tx power consumption in the mobile unit. The ASK/OOK modulation is adapted for near field data communication to send the control signal from the stationary unit to the headstage/implanted WINeRS system. The Bluetooth Low Energy (BLE) with 2.4 GHz RF data communication is optionally used for forward data communication to WINeRS-8 board equipped with MCU when the near field communication in the EnerCage-HC is not feasible. The WINeRS-8 also includes the 4-channel biphasic current controlled stimulator (CCS) with 5-bit digital-analog converter (DAC), which is necessary for the real-time closed-loop feedback control using the types of internal neurophysiological signals.

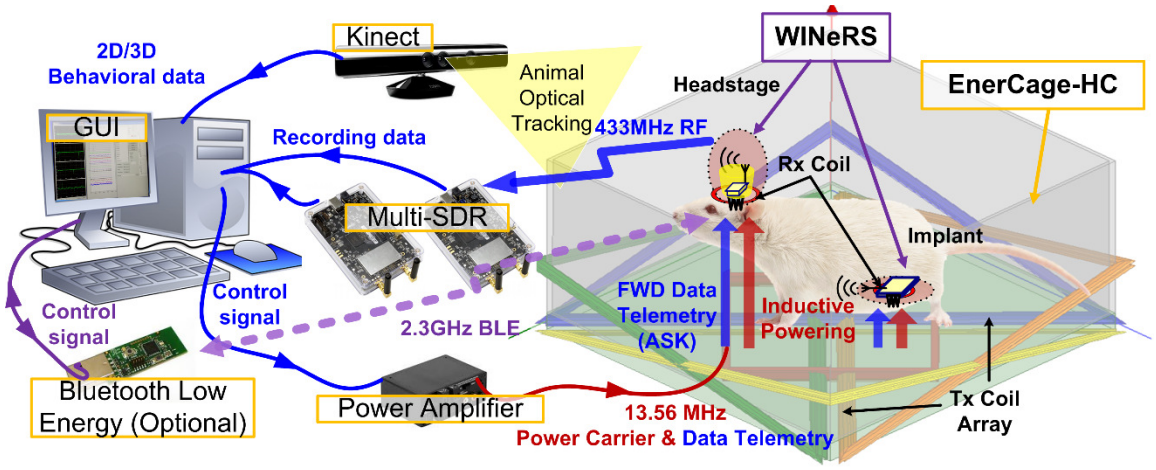

Fig. 5.1. A conceptual view of power and data flows for inductively-powered wireless implantable neural recording and stimulation (WINeRS-8) system in EnerCage-HC system for long-term neural recording/stimulation from small freely behaving animal.

5.1 Overview of Wirelessly Powered Implantable Central and Peripheral Nerve Recording and Stimulation System ASIC

A simplified block diagram of the WINeRS-8 ASIC compatible with EnerCage-HC system is shown in Fig. 5.2a, in which 32-channel adaptive averaging low noise front-end amplifies and filters central/peripheral signals as described in chapter 5.2. Each of 2-channel analog front-end (AFE) shares a 50 kS/s 10-bit SAR ADC for digitization depends on 'CH_sel' bit resulted in 25 kS/s for the individual channel. The digitized data packet, which includes 13-bit preambles from the preamble generator, is sent to 433 MHz On-off keying (OOK) transmitter to be transmitted, which carrier frequency is generated by the internal phase-locked loop (PLL) based on the reference clock of 13.56 MHz. The 13.56 MHz power carrier is rectified, and provides three regulated supply voltages, which are V_{DDA} = V_{DDL} = 1 V for analog and digital blocks, and V_{DDH} = 2 V for RF and stimulation blocks, respectively. The OOK and pulse-position modulation (PPM) demodulators convert the incoming OOK data stream through the inductive link into the forward telemetry data & clock to change the recording/RF control parameters or stimulation parameters with the stimulation flag signal. The preamble detector decides that the demodulated forward telemetry data in the PPM demodulator will be utilized for

recording/RF parameters or for stimulations. The 4-channel biphasic current controlled stimulator (CCS) is implemented for the positive (P) and negative (N) stimulations equipped with individual 4 MUXs. The stimulation flag signal is synchronized by the stimulus artifact rejection signal to prevent the saturation of AFE channels during the stimulation period. The WINeRS-8 ASIC was fabricated in a 5M2P 130 nm standard CMOS process, occupying 2.4 × 5 mm^2 excluding WINeRS-8 PMIC, which are the rectifier and OOK-PPM demodulator, and the nominal power consumption of the WINeRS-8 ASIC is 18.9 mW as shown in Fig. 5.2b.

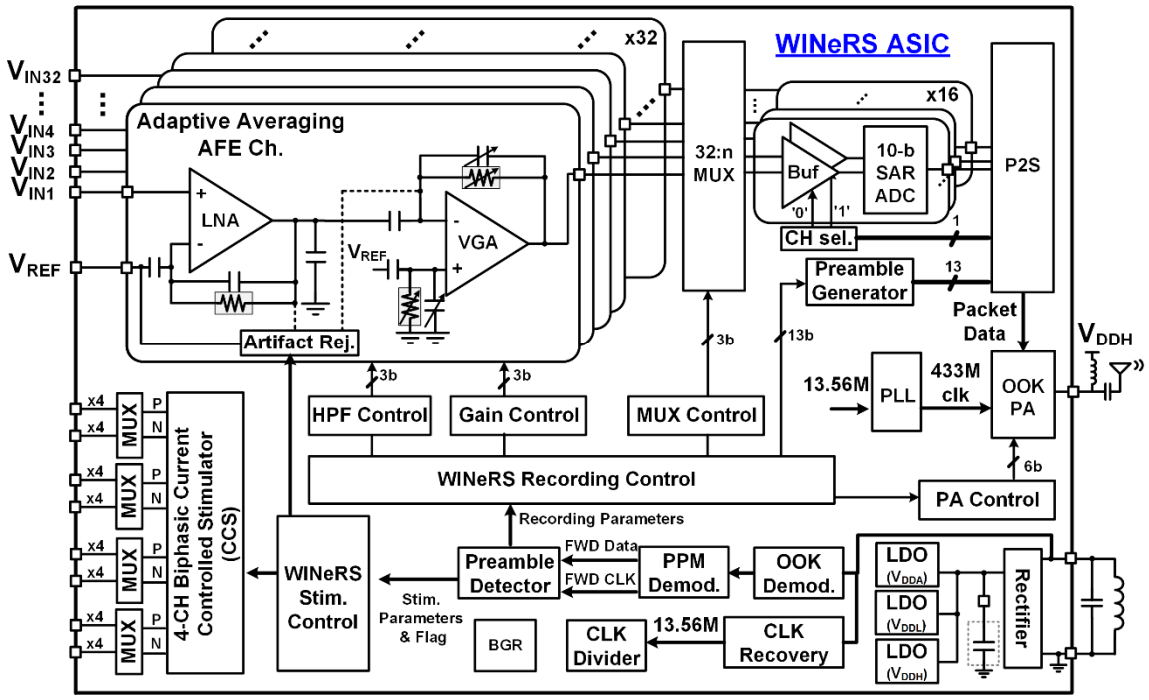

(a)

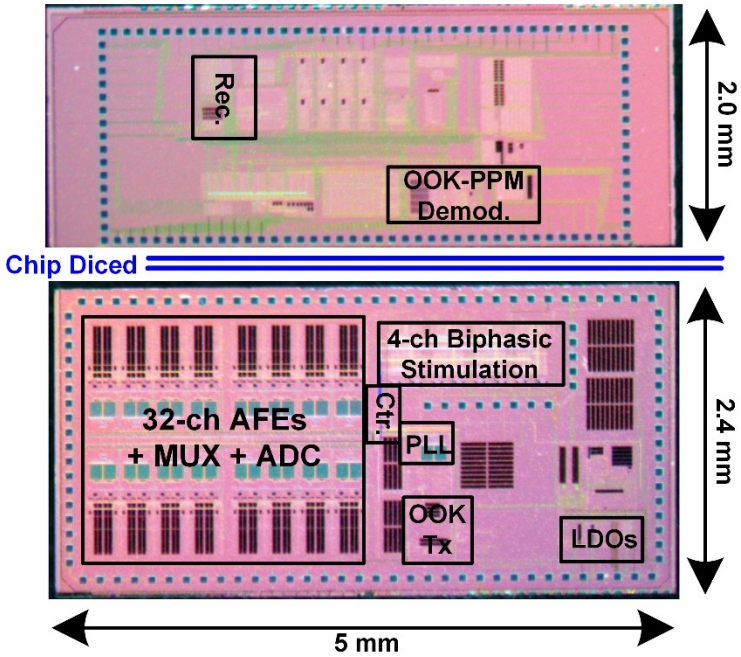

(b)

Fig. 5.2. (a) A simplified block diagram and (b) die photo of the inductively-powered wireless implantable neural recording and stimulation (WINeRS-8) ASIC

5.2 Adaptive Averaging Low Noise Front-End for Central and Peripheral Nerve Recording

Peripheral nerve interfacing technology has sought for in applications, such as the integrated visceral neural network (iVNN), for discovering and manipulating the patient's peripheral neural network to manage various disorders [103]. The iVNN observes both central and peripheral neuron activities, and the information acquired by neural network and peripheral nervous system (PNS) can be utilized for brain-machine interfacing (BMI), substitute pharmacological solutions, or used for functional electrical stimulation (FES).

Recording activities from central nervous system (CNS) and PNS have different characteristics in terms of electrodes, bandwidth, and signal strength. For example, the amplitude of the electroneurogram (ENG) recorded with cuff electrodes typically shows a few tens of μV in amplitude [104], while the action potentials (AP) in CNS are in the order of several hundred μV, with up to 10 kHz bandwidth [105]. Therefore, the analog front-end (AFE) to record the peripheral nerve activities should have much lower input referred noise than the AFE used in a conventional neural recording system.

Several techniques to reduce the input referred noise of the low noise amplifier (LNA) in the AFE have been proposed. The LNAs designed in the BiCMOS process show very low noise thanks to the bipolar transistor inputs [106]. However, this type of LNA cannot be used in the standard CMOS process with low supply voltage. Although the chopper modulation technique introduced in [107] can reduce the input referred noise, the input impedance is significantly reduced by the chopping function, which frequency needs to be proportional to the bandwidth of the input signal. Therefore, the signal-to-noise ratio (SNR) drops for higher chopping frequencies, and its application is limited to recording lower bandwidth signals up to a few 100 Hz, such as electroencephalogram (EEG) recording.

The complementary-input amplifier was presented to double the input transconductance (g_m) with a given bias current [108]. This technique can efficiently

improve the noise efficiency factor (NEF), however, it still degrades the input impedance with the doubled AC-coupling capacitors connected to the doubled input MOSFETs, which are needed to prevent DC offsets at the electrode-tissue interface. The idea of averaging low noise amplifier outputs in the hardware was first introduced in [109], using off-the-shelf components. Although this concept can achieve low input referred noise for the peripheral nerve recording, the discrete device was too bulky for implantation in the body, and it was not able to operate at low supply voltage, resulting in large power consumption at 1.63 mW/ch. In addition, the input impedance of ~10 MΩ for each LNA is insufficient for high impedance electrodes in the impedance range of 10s of kΩ up to MΩ [110], particularly because the input impedance of the LNA is inversely proportional to the number of channels being combined in parallel for hardware averaging. More recently, an LNA with sub-μV_{rms} noise level was designed with bias current control to provide different input-referred noise levels. However, the telescopic structure is not suitable for low supply voltage operation [111]. Also the input impedance for this implementation is inherently low due to its large input capacitance.

In this section, an adaptive averaging low noise amplifier for the recording of both CNS and PNS signals is presented, which equips the high input impedance structure with the doubled input g_m for improved NEF. The proposed AFE channels use an adaptive averaging structure to control the level of the input referred noise, depending on the biomedical signal strength. This also has a benefit in long term recording when the neural signal becomes weaker due to scar tissue formation, resulting in some electrodes completely lose their signals [112]. In this case, those AFE channels can be combined which have lost their input, and improve the SNR in the remaining channels that are still viable.

5.2.1 Adaptive Averaging Topology

Fig. 5.3 shows the schematic diagram of the multi-channel AFE implementation of the adaptive averaging technique. The 32-ch neural recording AFE, in each channel consists of an LNA, a variable-gain amplifier (VGA), and a buffer, which amplify and filter the neural signals with a designated output noise of $v^2_{no,AFE}$, as shown in Fig. 5.3. In this neural recording AFE, the input referred noise of the individual channel is enough to amplify CNS neural signals, which typically have ~100 μV amplitude. When the AFE requires lower input referred noise to record much smaller peripheral nerve signals, a number of AFE channels can be combined by a 32-to-*n* analog multiplexer (MUX) to reduce the input referred noise of the AFE. Considering the output noise of the individual AFE channels, including the LNA and VGA, $v^2_{no,AFE}$, the combined *m*-channel output noise, $v^2_{no,AFE,m}$, can be presented as,

$$v^2_{no,AFE,m} = v^2_{no,AFE(0)} + v^2_{no,AFE(1)} + \ldots + v^2_{no,AFE(m-1)} \tag{5.1}$$

Since the output noise for each AFE channel, $v^2_{no,AFE(0)}$, $v^2_{no,AFE(1)}$, …, $v^2_{no,AFE(m-1)}$, is identical and uncorrelated with each other, while the output signal is the same, the effective input referred noise for *m*-channel combination, $v_{ni\_rms,AFE,m}$, can be presented as,

$$v_{ni\_rms,AFE,m} = \frac{v_{ni\_rms,AFE,1}}{\sqrt{m}} \tag{5.2}$$

where *m* is *32/n*, *n = 2, 4...32*, for the 32-ch neural recording AFE, as shown in Fig. 5.3.

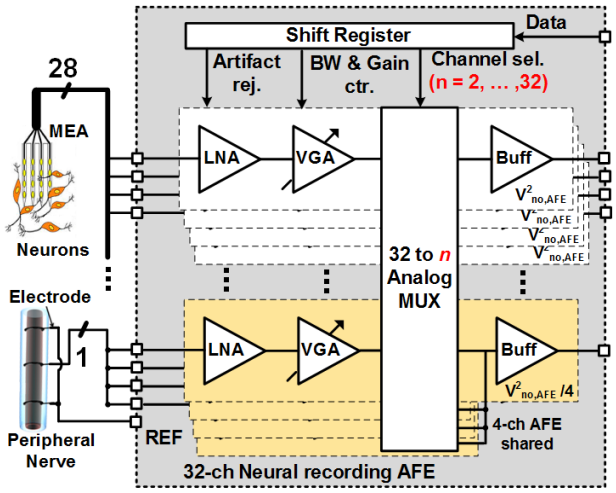

Fig. 5.3. Simplified schematic diagram of the multi-channel AFE with adaptive averaging technique for neural and peripheral nerve recordings.

The adaptive averaging topology has several advantages in terms of achieving low noise and flexibility in practical applications. Instead of the one ultra-low noise LNA, which either has large size or large power consumption, several LNAs, which overall size and power consumption is close to that of the large LNA, can be purposefully combined or divided by the MUX for the desired application at hand, such as CNS or PNS recording, which require specific low levels of input referred noise. In addition, input referred noise control of the AFE without any additional power consumption is beneficial for implanted devices that store or wirelessly receive a limited amount of power. It should be noted that this hardware averaging method still degrades the SNR because the input impedance of each LNA is reduced by a factor of *m*. Thus, starting with high input impedance LNA becomes important particularly when electrode and contact impedances are high.

5.2.2 DC-Coupled Input Offset Rejection LNA

As discussed in chapter 5.2.1, high LNA input impedance is desired to achieve high SNR considering the often high impedance small recording microelectrodes. Moreover, the LNA should be able to eliminate a DC offset of -100 mV to 100 mV at the

input, which results from electrode-electrolyte half-cell potentials [115]. In the conventional LNA structure with capacitive feedback [113], the DC blocking capacitor for removing this DC offset should be large to provide enough gain and minimize signal attenuation between the blocking capacitor and electrode impedance. This capacitor occupies large area on chip, and not suitable for todays' dense AFEs with high channel count [114]. Although some DC-coupled input offset rejection methods are developed to eliminate the DC blocking capacitors [115], [116], most of these circuits only offer open-loop gain, which result in gain inconsistency among different channels.

The proposed closed-loop DC-coupled doubled-g_m LNA schematic is shown in Fig. 5.4, with all the features needed for it to be used for the proposed adaptive averaging method towards a low noise AFE with fairly small footprint. The first stage consists of a complementary input stage LNA that doubles the input g_m for higher NEF and a large open-loop gain of A. The LNA output, V_{LNA}, is low pass filtered (LPF) in a feedback loop with transfer function of $\beta = (1+jwR_1C_2)/(1+jwR_1C_1+jwR_1C_2)$ and high cut-off frequency of $f_2 = 1/(2\pi R_1C_1)$. The feedback signal, V_{LPF}, is subtracted from the input signal, V_{IN}, after a capacitive attenuator to provide high pass filtering (HPF) and amplification with low cut-off frequency and mid-band gain of $f_3 = 1/(2\pi R_1C_2)$ and $A_{V,LNA} = A_0 = 1+C_1/C_2$, respectively. The closed-loop LNA transfer function can be expressed as,

$$A_{V,LNA} = \frac{V_{LNA}}{V_{IN}} = \frac{1}{\beta} = 1 + \frac{jwC_1R_1}{1+jwC_2R_1}. \tag{5.3}$$

Although the DC-coupled LNA can provide sufficient DC offsets rejection at the electrode-electrolyte interface, AC- coupling at the input of the following VGA is desired because the DC offset the LNA cannot be perfectly removed. The high pass -3dB bandwidth and the overall gain of the AFE can be digitally adjusted by R_2 and C_4, which follow by the LNA low cut-off frequency at f_3. The VGA transfer function can be expressed as,

$$A_{V,VGA} = \frac{V_{AFE}}{V_{LNA}} = \frac{jwC_3R_2}{1+jwC_4R_2}, \tag{5.4}$$

providing an overall midband AFE gain of $A_{AFE} = A_{V,LNA} \cdot A_{V,VGA}$.

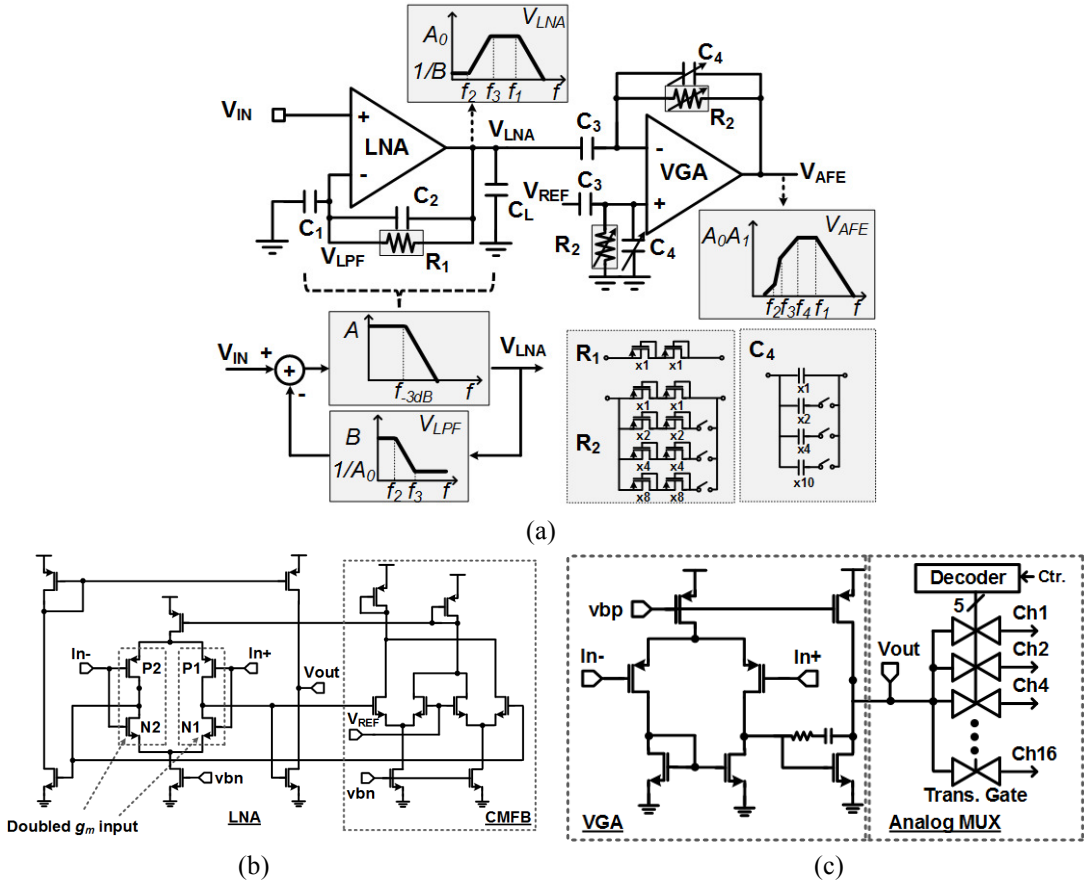

Fig. 5.4. (a) Schematic diagram of the DC-coupled neural recording AFE with input offset rejection, and bode plot of the AFE blocks and its feedback network. (b) Complementary input stage LNA that doubles the input g_m for higher NEF. (c) Variable-gain amplifier with closed-loop gain from A_1= 2.4 to 40 and analog multiplexer implemented by a transmission gate array.

Both R_1 and R_2 are implemented using pseudo-resistors to obtain ~GΩ resistance, with R_2 being 3-bit adjustable for digital control of the HPF. C_4 can change from 50 fF to 850 fF by 3-bit gain control according to C_3/C_4. The DC-coupled LNA structure can minimize the effects of neural signals DC drift without large DC blocking capacitors or chopper modulation, maintaining the high input impedance of the LNA, needed for the adaptive averaging, shown in Fig. 5.3.

5.2.3 Doubled-g_m Architecture

The high NEF of the LNA is desirable to achieve ultra-low noise without large power consumption. A disadvantage of the doubled input g_m technique, which is the doubled DC-coupling capacitors compared to the conventional LNA [108], [113], is overcame by the proposed topology in Fig. 5.4a by DC-coupled input offset rejection.

The schematics of the doubled input g_m LNA is shown in Fig. 5.4b. The complementary input stage with N1 and P1 doubles the amplifier's effective g_m compared to the conventional amplifier using the same amount of power. The effective input referred noise, $v^2_{ni,LNA}$, can be found from [108],

$$v^2_{ni,LNA} = \frac{16kT}{3(g_{mp} + g_{mn})} \cdot \Delta f \,, \tag{5.5}$$

where g_{mp} and g_{mn} are the transconductance of P1 and N1, respectively.

5.2.4 VGA and Analog Multiplexer

The schematic of the VGA followed by the analog multiplexer for adaptive averaging is shown in Fig. 5.4c. The VGA provides closed-loop gain that is adjustable from 2.4 to 40 and HPF from 1 Hz and 400 Hz, each with 3-bit digital control. The analog multiplexer is implemented by a transmission gate array to select a parallel combination of AFE channels. In this prototype, $m = 2^{k-1}$ ($k = 1:5$) VGA outputs can be combined with 5-bit digital control to adjust the AFE input referred noise.

5.2.5 Experimental Results

A 32-ch prototype of the proposed adaptive averaging low noise AFE was fabricated in a 5M2P 130-nm standard CMOS process with 1 V supply, occupying 2.4 × 2.5 μm^2 on chip including its control block. Table 5.1 summarizes the main AFE specifications and Fig. 5.5 shows the experimental setup, the die photo, and floorplan. The frequency responses of the LNA and VGA blocks are shown in Fig. 5.6a and 5.6b,

respectively. The AC response of the LNA is measured in the DC offset range from -200 mV to 100 mV. The mid-band gain is ~43.5 dB within 20 Hz to 15 kHz bandwidth. These measurement results show that the proposed LNA can provide a wider range of DC offset rejection than prior DC-coupled LNA in [112].

TABLE 5.1 DESIGN PARAMETERS OF ANALOG FRONT-END

P1, P2(W/L)	**N1, N2**(W/L)	C_1/C_2	C_3/C_4	C_L
175 µm/3 µm	400 µm/2 µm	30 pF /200 fF	2 pF /50 fF~850 fF	5 pF

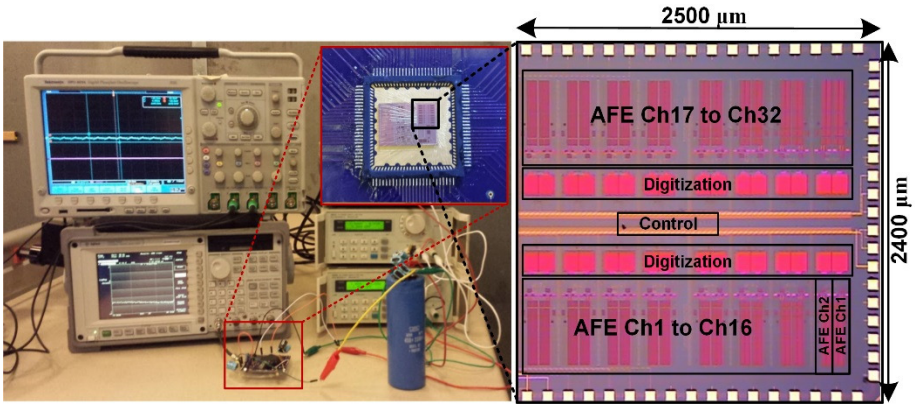

Fig. 5.5. The experimental setup, die micrograph, and floorplan of the 32-ch proof-of-concept prototype AFE, including the control block.

The VGA block can independently change the low cut-off frequency of the HPF from 1 Hz to 400 Hz (Digital bits: H000-H111) and the mid-band gain from 7.6 dB to 32 dB (Digital bit: G000-G111). The LNA and VGA consume 11 µA and 2.1 µA from 1 V supply, respectively. The power supply rejection ratio (PSRR) is measured 41 dB at 1 kHz, and the input impedance of each LNA is ~61 MΩ at 1 kHz.

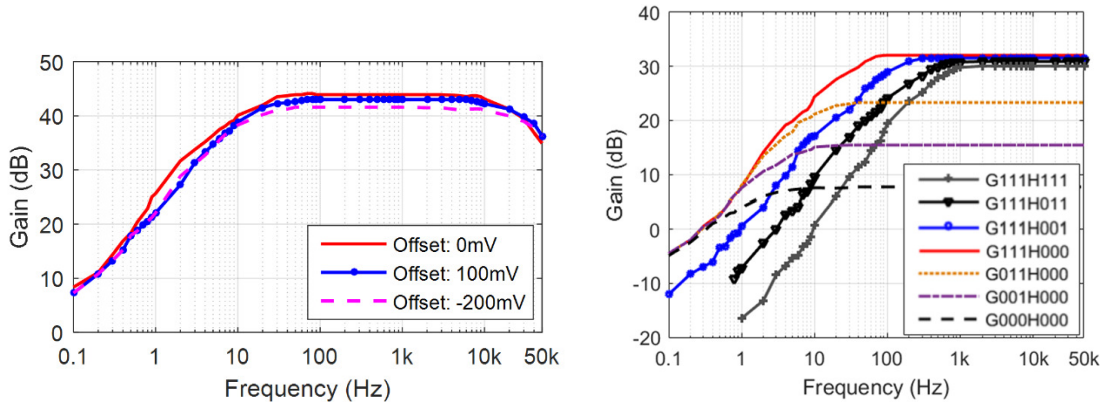

Fig. 5.6. The measured AC responses of (a) the LNA, and (b) the VGA.

The noise spectral densities of the AFE for m = 1, 4, and 16 are shown in Fig. 5.7a with their input referred transient background noise waveforms in Fig. 5.7b. The AFE RMS input- referred noise for 1, 4, and 16 channels in parallel are 3.0 μV_{rms}, 1.8 μV_{rms}, and 1.1 μV_{rms} in the 10 Hz to 17 kHz frequency range, respectively. According to (5.2), we anticipate the noise power to drop by a factor of 2 when increasing m by a factor of four. However, measurements indicate a lower factor of ~1.67. This could be because the noise in each AFE channel is not entirely random and uncorrelated, and common noise source, such as 60 Hz powerline interference or noise from the digital block, which appear on all AFE channels, cannot be reduced by averaging. Moreover, it should be noted that the input impedance at 1 kHz is inversely proportional to m, and decreases from 61 MΩ to 3.8 MΩ in 16-ch averaging, which results in slightly higher attenuation of the input signal, depending on the electrode-electrolyte impedance.

Table 5.2 benchmarks specifications of the proof-of-concept AFE prototype with adaptive averaging against recently reported state-of-art biomedical AFEs for CNS and PNS applications. The proposed AFE demonstrates superior input impedance (Z_{IN}) with very good input referred noise and NEF, while other parameters are still competitive. A key advantage of the proposed AFE is that it can flexibly disconnect channels with no

good input signal and combine their AFE electronics with other LNAs to improve the SNR of the channels with viable or more important recording capability.

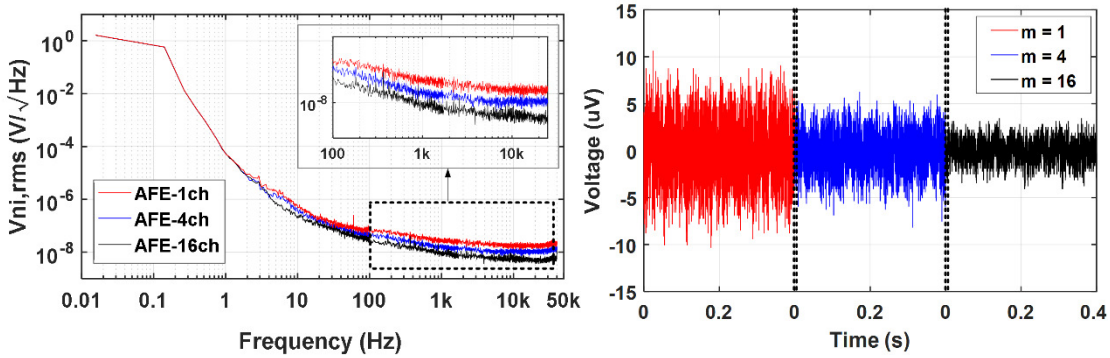

(a) (b)

Fig. 5.7. (a) The measured noise spectrums of the prototype AFE for *m = 1, 4,* and *16*. (b) Measured transient background input referred noise waveforms.

The functionality of the AFE prototype was verified by playing attenuated pre-recorded spike waveforms, which contained ~10 mV_{pp} spikes plus 4 Hz local field potential in the background. The signal was applied to the LNA input through -50 dB attenuation to generate spikes in tens of μV_{pp} range. Fig. 5.8 shows the AFE input and output transient waveforms, in which around t = 1.6 s, the control unit changes *m* from 16 to 1 in order to show the difference in SNR. The individual spikes are extracted in these waveforms based on a threshold-based algorithm, and the SNR is calculated as the average peak value of the spikes divided by three times of the standard deviation of the background noise [118],

$$SNR = \frac{\frac{1}{n}\sum_{i=1}^{n}|V_i|}{3\sigma}, \tag{5.6}$$

where V_i is the peak of an individual spike, and σ represents the standard deviation of the background noise. These measurements show that the average SNR is improved from 1.08 to 2.12 when *m* is changed from 1 to 16 thanks to the adaptive averaging technique.

TABLE 5.2 BENCHMARKING OF THE PROPOSED ADAPTIVE AVERAGING ANALOG FRONT-END

Parameter	This work	2012 [108]	2006 [106]	2012*** [115]	2016 [107]	2015 [117]	2016 [111]
VDD (V)	1	1	5	0.5	0.2/0.8	1	3.3**
I_{Amp} (µA)	11/44/176	12.1	260	60	1.6/0.25	2.8	271
LNA Gain (dB)	44	40	40.8*	32*	50	52.1	39.3 or 58.4
Bandwidth (Hz)	20-15k	0.025-7.2k	310-3.3k	300-10k	0.5-670	1-8.2k	0.1 – 20k
I.R. Noise (μV_{rms})	3.0/1.8/1.1 (m=1,4,16)	2.2	0.29	4.9	0.94	4.13	0.63 – 1.5
NEF	2.95/3.54/4.32	2.9	4.3	5.99	2.1	2.93	3.5
$NEF^2 \cdot VDD$	8.68/12.5/18.7	8.4	92.45	17.96	1.6	8.58	40.4
PSRR (dB)	41	85	42	64	74	78	NA
Z_{IN} @ 1 kHz (MΩ)	61/15/3.8	4	~0.015**	NA	NA	~20**	NA
Area (mm^2)	0.07/0.28/1.12	0.072	12	0.013	0.32**	0.042	0.51
DC rejection	DC-coupled (-0.2V ~ 0.1V)	AC-coupled	NA	DC-coupled (±0.05V)	AC-coupled	AC-coupled	AC-coupled
Application	CNS/PNS	CNS/PNS	PNS	CNS	EEG	CNS	CNS/PNS
Technology (nm)	130 CMOS	130 CMOS	800 BiCMOS	65 CMOS	180 CMOS	65 CMOS	350 CMOS

*Open-loop, **Estimated, ***Including digitization for offset rejection

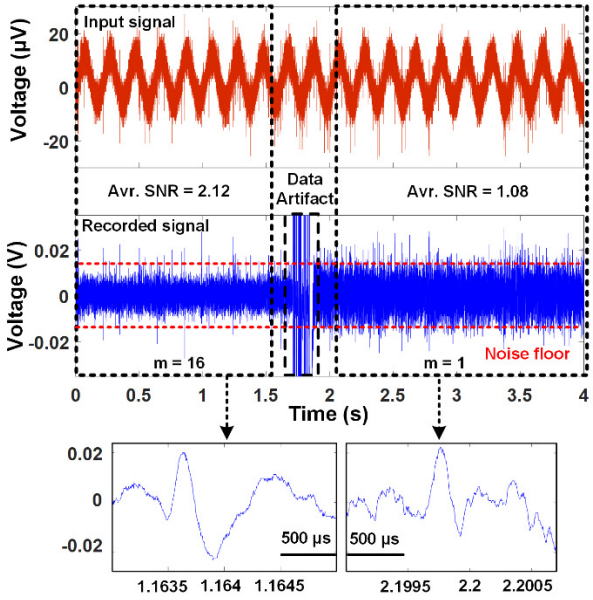

Fig. 5.8. The attenuated pre-recorded original spike signal (Top) and recorded transient AFE output signal (Bottom) with transient adaptive noise variation from m = 16 to 1 for SNR comparison.

5.3 4-Channel Biphasic Current Controlled Stimulator (CCS) with Stimulus Artifact Rejection

For closed-loop central and peripheral nerve interfacing, 4-channel biphasic current controlled stimulator (CCS) is implemented in the WINeRS-8 ASIC. Compared to the voltage controlled stimulation (VCS), CCS shows more reliability in terms of the charge balancing and accurate stimulation control although it provides lower efficiency due to the output voltage necessary to drive predetermined current through variable electrode and tissue impedances [119].

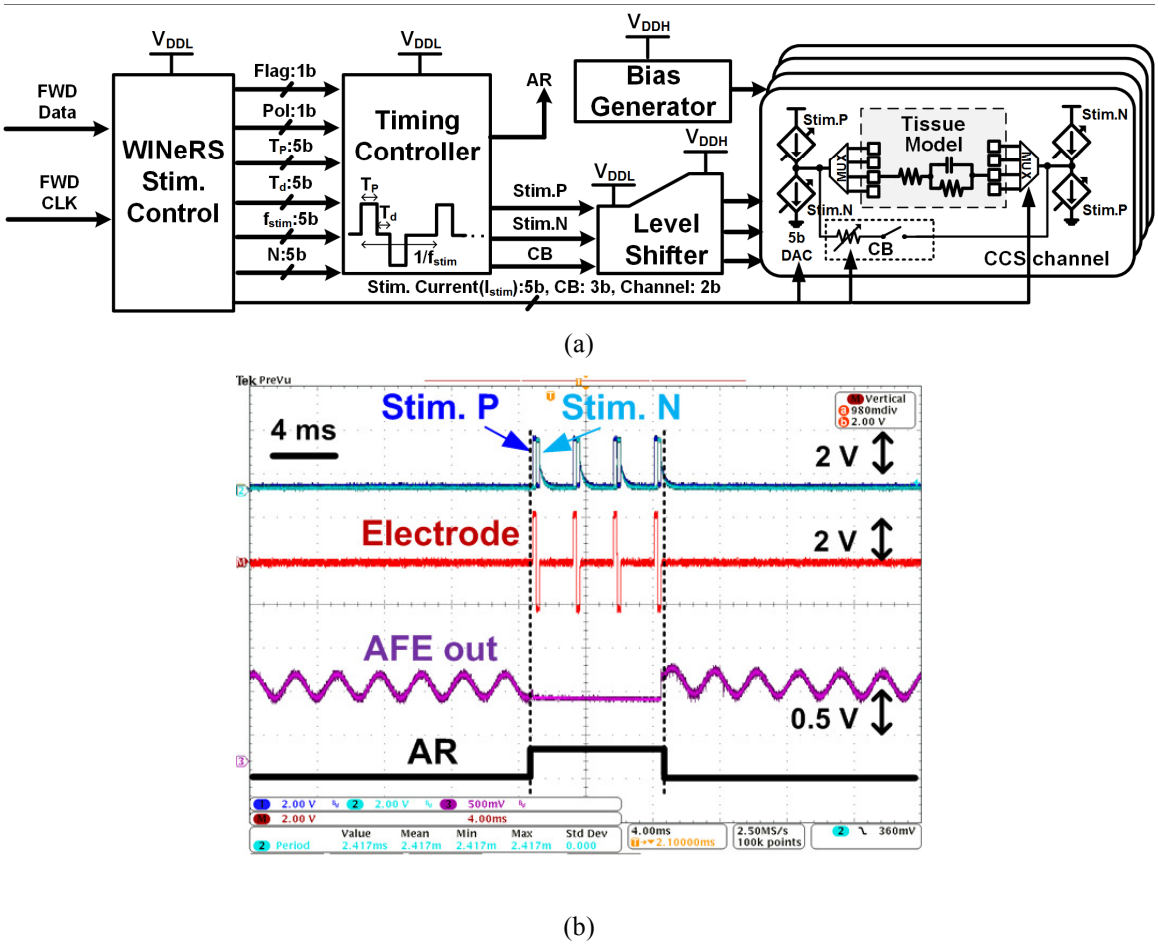

Fig. 5.9. (a) The block diagram of 4-channel biphasic CCS in WINeRS-8 ASIC for closed-loop recording and stimulation, and (b) measurement waveforms of *in-situ* experiment for biphasic stimulation and stimulus artifact rejection with Randles equivalent tissue model.

The block diagram of the 4-channel biphasic CCS in WINeRS-8 ASIC is shown in Fig. 5.9a for closed-loop recording and stimulation, which the stimulation parameters are summarized in Table 5.3. The WINeRS stimulation control block received the recovered forward telemetry data (FWD Data) and clock (FWD CLK) from the PPM demodulator followed by the preamble detector as described in Fig. 5.2. When incoming 13-bit preamble matches with the stimulation preamble, '101010101010011', the stimulation control block reads the stimulation parameters and send the recognized 30-bit stimulation parameters to the timing controller and CCS channel with the flag pulse. The timing controller, which includes the series of clock dividers and delay cells, generates the corresponding stimulation pulses, *Stim. P* and *Stim. N*, based on the 6 parameters, which are polarity (*Pol*: 1b), stimulation frequency (f_{stim}: 5b), stimulation pulse width (T_p: 5b), pulse delay between *Stim. P* and *Stim. N* (T_d: 5b), and number of stimulating pulse train (N: 4b). Since all of digital controllers are designed for 1 V digital supply voltage (V_{DDL}) to reduce the power dissipation mainly in the clock dividers, the level shifter is included to drive the CCS operating in high supply voltage (V_{DDH}). The charge balancing (CB) pulse removes the residual charge in the tissue if the positive and negative stimulation pulses are not perfectly balanced. The passive charge balancing method can be controlled by the 3-bit parameter. The stimulation current, I_{stim}, can be controlled by the 5-bit current digital-analog converter (DAC) from 60 µA to 1.86 mA. The 4-channel MUX at the output of the individual CCS can provide the active site selection through 2-bit control signals.

TABLE 5.3 SUMMARIZATION OF CCS PARAMETERS IN WINERS-8

Preamble	Polarity (Pol)	Stim freq. (f_{stim})	Stim width (T_p)	Stim delay (T_d)	Stim current (I_{stim})	Stim channel	# of stimulating (N)	Charge balancing (CB)
15b	1b	5b	5b	5b	5b	2b	4b	3b
'101010101010011'	Pos /Neg	13-414 Hz	9.5 – 304 µs	9.5 – 304 µs	60 – 1860 µA	Ch 1 ~ 4	1 - 16	-

The timing controller also generates the stimulus artifact pulse during the entire stimulation period to prevent the saturation of AFE channels due to the stimulating pulses. The *AR* pulse forces the LNA output and VGA in the AFE channels to stay at the reference voltage, $V_{DDA}/2$, through the buffer to enable the recording function of the AFE channels right after the stimulating pulse trains from the CCS. Fig. 5.9b shows the measurement waveforms of *in-situ* experiment for the stimulation and stimulus artifact rejection. The Randles equivalent circuit model in [120] is used for the tissue model in this experimental setup. When the stimulation parameters and flag signal are transmitted to the WINeRS stimulation control block, AR signal is generated by the timing controller in the CCS in order to prevent the saturation of the AFE output voltage from the large stimulus artifact and to enable the recording function after the stimulation.

5.4 Low-power Data Communication for Forward Data Telemetry

One of the most different features of WINeRS-8 system with the previous WINeR-7 system in [102] is the implementation of the stimulation functionality with the forward (downlink) data telemetry to control the implanted device in real time. Since the downlink data telemetry for control of the WINeRS-8 ASIC doesn't need a high data rate compared the backward (uplink) data telemetry, which needs to transmit the continuous digitized data stream of the recorded neural data with the data rate of 9 Mbps described in chapter 5.5, the near-field data communication is regarded as more suitable method for the downlink data telemetry within a few cm distance in the EnerCage-HC due to limited distance for the wireless power transmission.

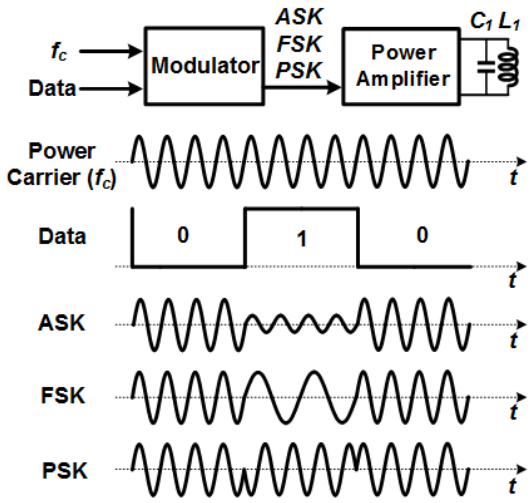

Fig. 5.10. Single-carrier data modulation techniques for downlink data telemetry.

Most popular data modulation techniques, widely used in the near-field data telemetry for single-carrier frequency are shown in Fig. 5.10. ASK is one of the most popular data modulation method for downlink data telemetry due to its simple modulation and demodulation circuitry with low power consumption [121]. However, the inaccurate synchronization between data and clock signal makes ASK more sensitive to the inductive coupling variations and noise component in the inductive powering. FSK and PSK are less susceptible to noise while FSK needs larger bandwidth per bit than ASK, which is not available in high-Q inductive links, and PSK requires the synchronization in frequency and phase resulted in the complicated circuitries of Rx and Tx. Therefore, the pulse position modulation (PPM) to recover the clock and synchronized data in [92] was employed with ASK modulation between the WINeRS-8 ASIC and the EnerCage-HC system to establish the robust data communication as shown in Fig. 5.11a. The conceptual waveforms of the downlink data flow to control Rec & RF parameters are shown in Fig. 5.11b.

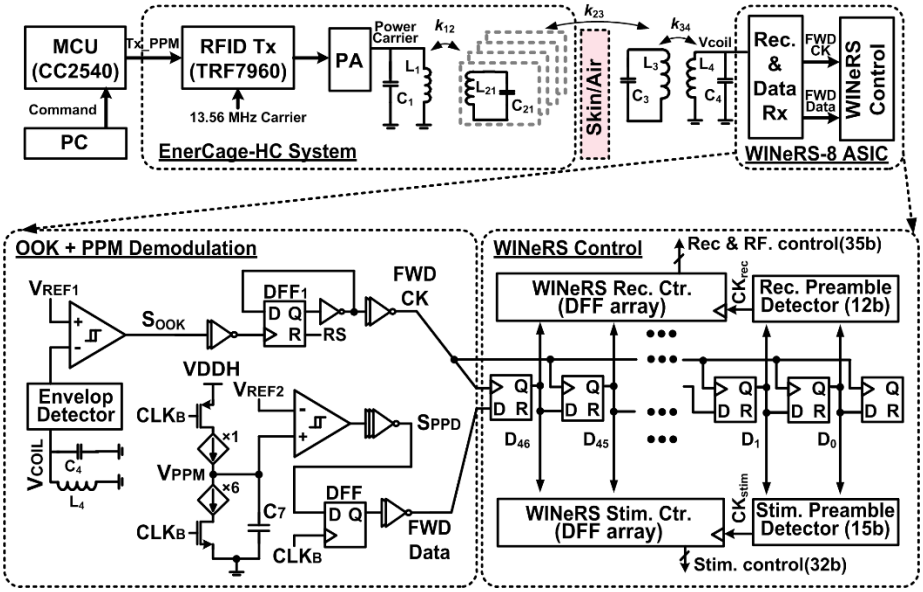

(a)

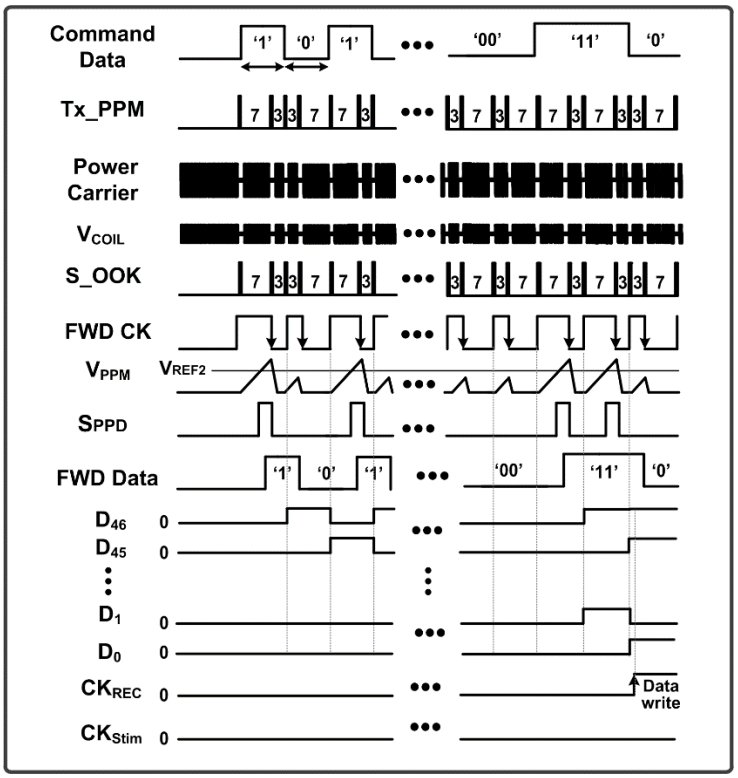

(b)

Fig. 5.11. (a) A block diagram of PPM downlink data modulation between EnerCage-HC (Tx) and WINeRS-8 (Rx) system via 4-coil inductive link and the downlink data buffer in WINeRS-8 control block, and (b) its conceptual waveforms of the downlink data flow for Rec. & RF parameter control.

The control commands in the PC are converted into the corresponding PPM pulses (Tx_PPM) via Microcontroller (CC2540) and applied to the RFID Tx (TRF7960)

to generate the modulated power carrier signal, f_p = 13.56 MHz, for wireless powering and downlink data transmission. The power carrier in V_{coil} in the Rx coil, L_4, is filtered by the envelop detector, and OOK pulses are recovered by the threshold detection, V_{REF1}. The recovered OOK pulses at S_OOK repeatedly charges and discharges the integration capacitor, C_7, depending on the delay between the individual OOK pulses while the data telemetry clock, FWD CK, is acquired by the edge of OOK pulses. When V_{PPM} at C_7 becomes higher than V_{REF2}, the comparator output, S_{PPD}, is triggered to '1' and the recovered data, FWD Data, becomes '1' while FWD data is synchronized by FWD CK as shown in Fig. 5.11b.

FWD Data are shifted by FWD CK in the data buffer, which consists of 47 DFFs, to detect the Rec. & RF preamble or the Stimulation preamble in two preamble detectors. These preamble detectors are composed of the simple digital logic to compare the pre-assigned preambles to incoming FWD Data. For example, if 12-bit of incoming FWD Data (D_0-D_{11}) are matched with pre-assigned 12-bit Rec. & RF preamble, CK_{REC} is triggered and the following data (D_{12}-D_{46}) is immediately read for control of recording and RF blocks. When D_0-D_{14} are matched with pre-assigned 15-bit stimulation preamble, CK_{Stim} is triggered instead of CK_{REC} to activate the stimulation with the given stimulation parameters as summarized in Table 5.3. Fig. 5.12a shows the measured transient waveforms of *Vcoil*, S_OOK, FWD Data, and V_{PPM} for 10 kbps near-field downlink data telemetry between WINeRS-8 and EnerCage-HC system as described in Fig. 5.11b. When the inputted preamble of FWD Data is matched with one of the pre-assigned preambles in WINeRS-8 system, Tx_PPM data is uploaded in the WINeRS-8 system with the flag signal, CK_{REC}, as shown in Fig. 5.12b.

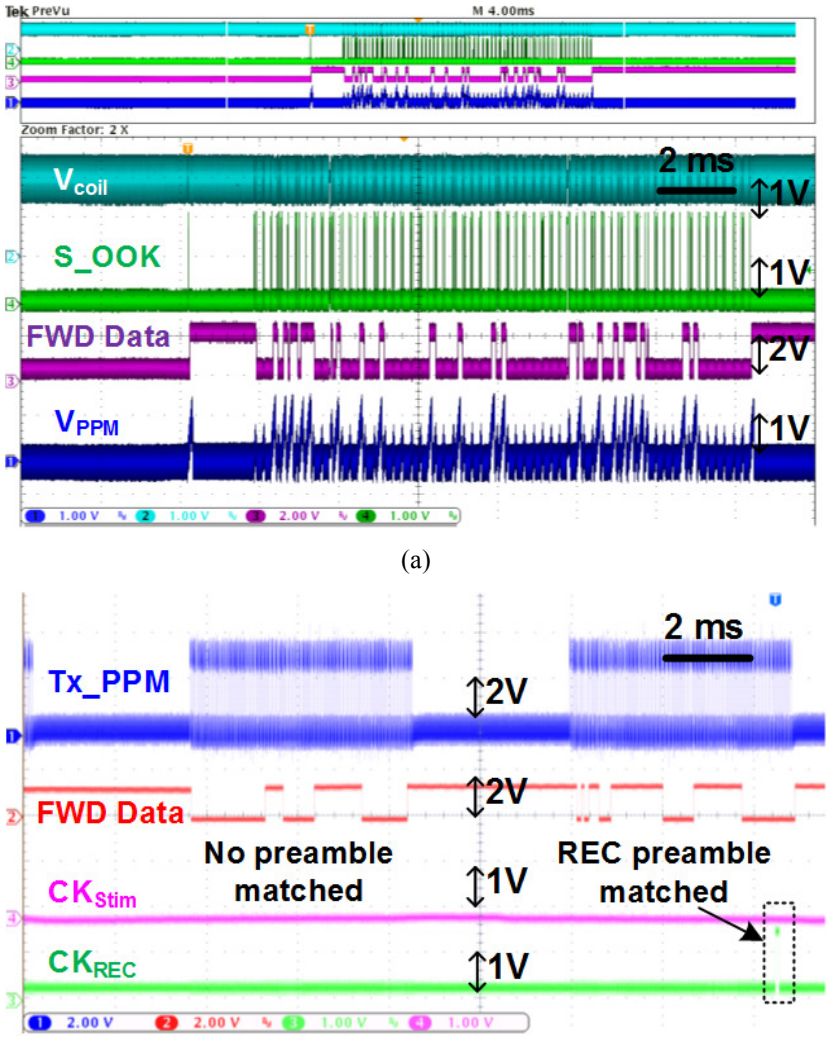

Fig. 5.12. The measurement waveforms of near-field downlink data telemetry between WINeRS-8 ASIC and EnerCage-HC system. (a) V_{coil}, S_OOK, FWD Data, and V_{PPM} in WINeR-8 ASIC, and (b) Tx_PPM from EnerCage-HC system to trigger CK_{REC} in WINeR-8 ASIC with matched preamble.

5.5 Robust Wideband RF Data Transmission between WINeRS-8 ASIC and Software Defined Radio (SDR) Receiver

A key objective of this chapter has been to design and develop a robust RF data transmission for high channel count wireless neural recording system in WINeRS-8 ASIC with potential clinical applications such as brain-computer interfacing (BCI). The challenges for high performance RF data transmission has been mainly researched on Tx side of the system because Tx side will eventually be implanted in the animal or human

body. However, a complete wireless data acquisition system including antennas, external Rx, computer interface, post processing, and graphical user interface (GUI) is important for the robust wireless data transmission system to guarantee the safety and reliability of the biomedical devices. Although there has been a wideband dual-antenna Rx to enlarge the RF coverage of the WINeR-7 Tx [94], the WINeR Rx unit has huge complexity in the hardware components for the duplication, and the FPGA-based time-to-digital converter (TDC) using a delay cell chain in WINeR Rx unit cannot ensure the stability of the data recovery due to the delay variation in the FPGA, which requires the compensation [122]. Moreover, VCO tunings method using external off-chip inductor and capacitor in WINeR-7 Tx degrades the uniformity of the wideband RF data transmission, influenced by the variations of the process, bonding wires, PCB lines, and time-varied environment of the implantable device in the animal or human body. Therefore, PLL-based OOK transmitter and commercial software defined radio (SDR) multi-receivers are considered in this chapter to achieve the robust wideband RF data transmission system for high channel count wireless neural recording data transmission in WINeRS-8.

5.5.1 Overview of WINeRS-8 RF Data Transmission with Multi-SDRs

Fig. 5.13 shows the block diagram of the recording data transmission from 32-ch electrode array to PC via 433 MHz OOK RF transceiver in WINeRS-8 ASIC. The neural spike signals typically have the bandwidth of 20 Hz – 10 kHz, and amplified in the 32-ch AFE. The implemented 2-to-1 MUX allows that each of two AFEs shares one 50 kS/s 10 bit resolution SAR ADC depending on the indicator, ‘0’ for even and ‘1’ for odd channel, respectively. The rectifier voltage is also sampled by 5 kS/s SAR ADC to monitor the status of the inductive powering, and eventually to operate the closed-loop inductive powering inside the EnerCage-HC system. The 176-bit packet buffer is composed of 13-bit preambles, 2-bit digitized rectifier voltage, 1-bit indicator of even or odd channel sampling (‘0’ or ‘1’), and individual channel data from 16-ch AFE depending on even or

odd indicator. The packet buffer is driven to the OOK power amplifier (PA) by 9.04 MHz clock to modulate 433 MHz carrier frequency generated by the internal PLL. The rectifier voltage information is divided into 10 packets, which starts with '11' or '10' for MSB, due to its lower sampling rate compared to the neural data.

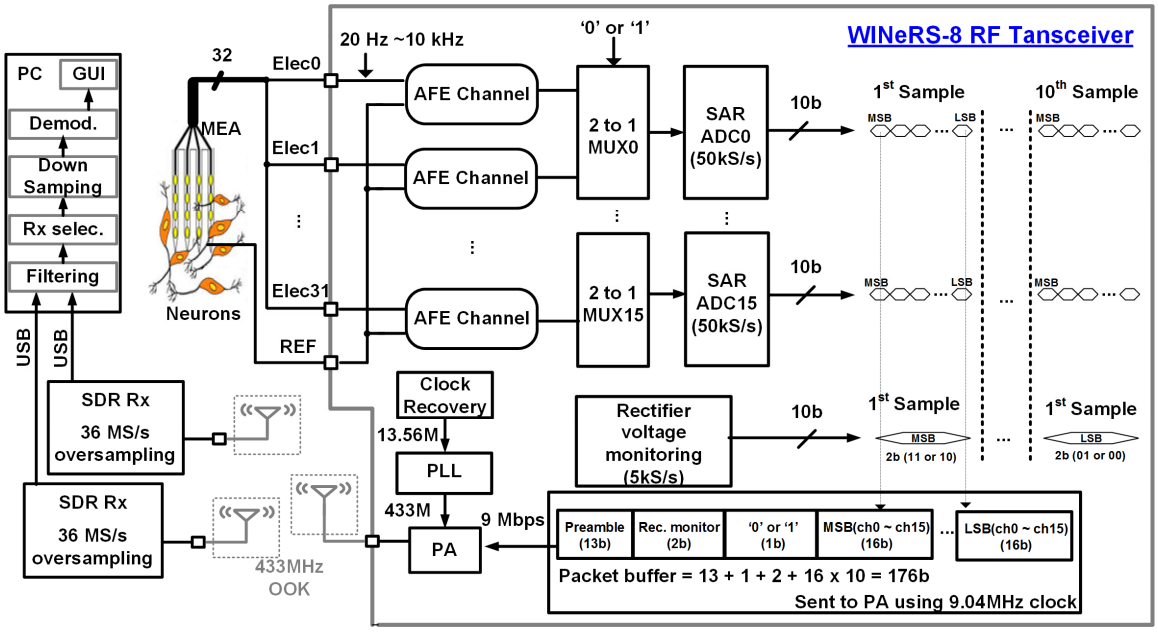

Fig. 5.13. A block diagram of the recorded data transmission from 32-ch electrode array to PC station via 433 MHz OOK RF transceiver in WINeRS-8 ASIC.

The RF signal from the WINeRS-8 Tx is picked up by each antenna, and amplified/filtered independently through the parallel SDR RF front end. The SDRs send the amplified/filtered/digitized RF information to PC via individual USB cables, and the PC performs the post processing and demodulation of the incoming RF data stream from the SDRs to display the recovered neural data on the screen in real time.

5.5.2 433 MHz OOK RF Transmitter in WINeRS-8 ASIC

The OOK RF transmitter in WINeRS-8 is composed of the PLL and OOK power amplifier as shown in Fig. 5.14. A three-stage current-starved ring oscillator is adapted to reduce the supply and temperature sensitivity [123]. The ring oscillator structure also has advantages in terms of smaller area and wide tuning range compared to the LC oscillator

in WINeR-7 Tx. The implemented ring oscillator operates up to 1.6 GHz based on the simulated result. The generated clock from the ring oscillator is divided into 5-stage DFFs and compared to *Ref. CK*, recovered from the power carrier, f_p = 13.56 MHz. The charge pump charges/discharges the integration capacitor, C_{ctr}, to control the bias current of the ring oscillator based on 'Up'/'Down' pulses from the phase detector, followed by the RC filter for loop stabilization. When the loop is stabilized, the frequency of ring oscillator, f_{PLL}, becomes 32×f_p, which is 433.9 MHz. Fig. 5.15 shows the measurement waveforms of the reference clock, f_P = 13.56 MHz, and the PLL frequency divided by the 5-stage frequency divider, f_{PLL}/32, in WINeRS-8 ASIC. The power consumption in the PLL block is 108 µW with 1 V supply voltage.

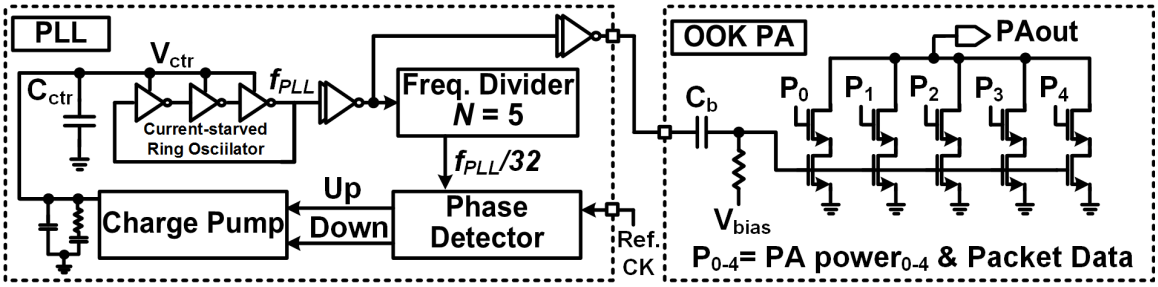

Fig. 5.14. A block diagram of PLL and OOK PA in WINeRS-8 ASIC for 433 MHz RF data transmission.

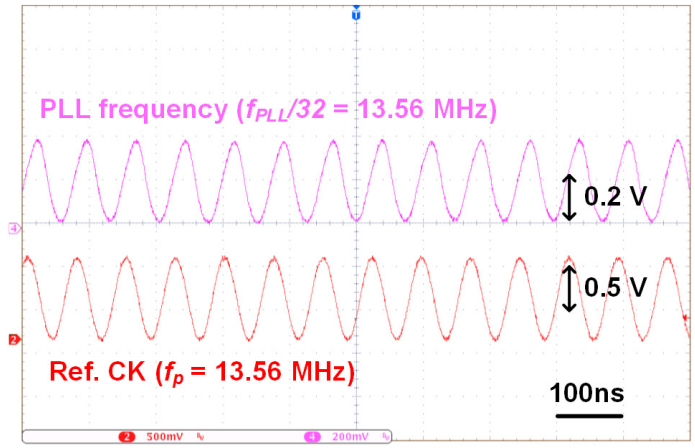

Fig. 5.15. Measured waveforms of the reference clock, f_p = 13.56 MHz, and the divided PLL output frequency by a factor of 32, f_{PLL}/32 = 13.56 MHz.

The output power of the OOK PA can be adjustable by 5-bit digital control, PA power$_{0\text{-}4}$. Digital pulses of P_0 - P_4 are generated by AND-gate operation between the

packet digital data in Fig. 5.13, and PA power$_{0\text{-}4}$ provided by the WINeRS Rec. control block in Fig. 5.11a. The maximum output power of the PA is 0.2 dBm with the data rate of 9 Mbps. The measured transient waveforms of the packet data stream with 9 Mbps and 433 MHz OOK PA output voltage matched with 50 Ω impedance are shown in Fig. 5.16.

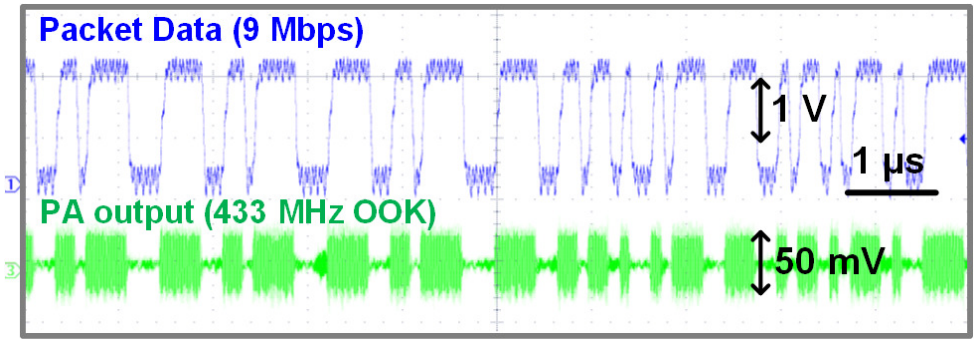

Fig. 5.16. Measured transient waveforms of the packet data stream with 9 Mbps and 433 MHz OOK PA output voltage matched with 50 Ω impedance.

5.5.3 Software Defined Radio (SDR) Multi Receiver for WINeRS-8

Software defined radio (SDR) is a radio communication system, which typically implements the amplifiers, filters, mixers, modulators/demodulators, ADC, control unit and computer interfaces for RF front end. The SDR provides the software defined wireless communication instead on replacement of the hardwired implementation. Since the re-programmed or reconfigured capability of the SDR, which provides the flexibility in carrier frequency, bandwidth, gain, and modulation method, the SDR has recently drawn the academic interest and increasingly also industrial interest [124].

Several commercial SDRs are available in the market such as HackRF, BladeRF, and USRP. The WINeRS-8 OOK receiver is developed by BladeRF due to its larger bandwidth, higher sampling rate of ADC/DAC, and relatively cheap price. BladeRF has 300 MHz – 3.8 GHz radio spectrum with full duplex, 12 bit ADC/DAC with 40 MS/s sampling rate, 40k/115k FPGA logic elements [125].

The GNU radio is one of the SDR development tools, and widely used for research, education, and proof-of-concept prototype due to its free open sources of many

signal processing modules [126]. The GNU radio applications are generally written in the Python programming language although the high-speed signal processing is performed by C++ language. In the WINeRS-8 OOK SDR receiver design, the GNU radio is utilized for RF signal processing while C++ language is used for unpacking the recovered packet data and displaying acquired real-time data as shown in Fig. 5.17.

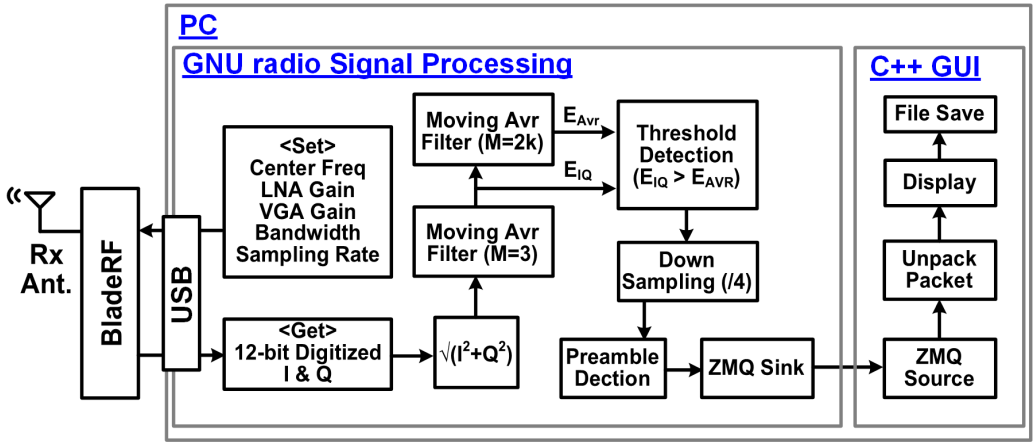

Fig. 5.17. Software subsystem of single WINeRS-8 receiver for RF signal processing and GUI

GNU radio can set the parameters of center frequency, LNA gain, VGA gain, bandwidth, and sampling rate of ADC in the BladeRF. The incoming 12-bit digitized I & Q signals, oversampled by 4 times, are converted to the magnitude, and 1st moving average filter of M = 3 is applied. This moving average filter reduces the noise as the number of points, M, in the filter increases while the edges becomes less sharp. 2nd moving average filter of M = 2k is utilized for the adaptive threshold for the OOK demodulation, which also indicates the average power of the Rx. The number of points in 2nd moving average filter can be optimized based on the variation of the received RF power, mainly affected by the distance or antenna directivity between Tx and Rx antennas. Fig. 5.18 shows the received RF spectrums at 1 m distance from the WINeRS-8 Tx, which has the center frequency of 433.5 MHz with 14 MHz bandwidth, and the 36 MHz over-sampled transient RF signals, which are applied by 1st and 2nd moving average filters, respectively. The 1st moving average (green) shows the less noise compared to the

original signal (blue) while the adaptive threshold for OOK demodulation is decided by 2nd moving average (red).

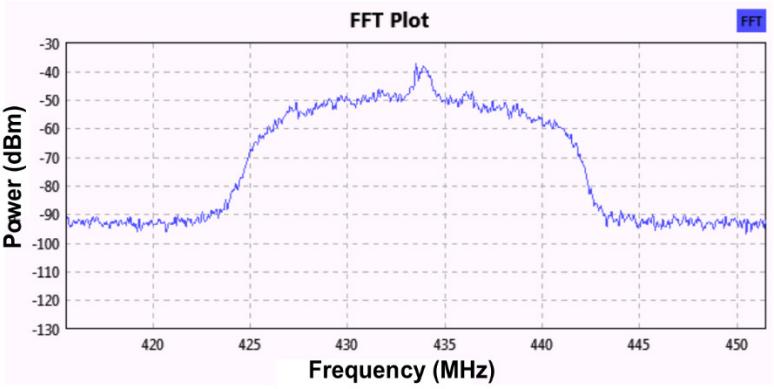

(a)

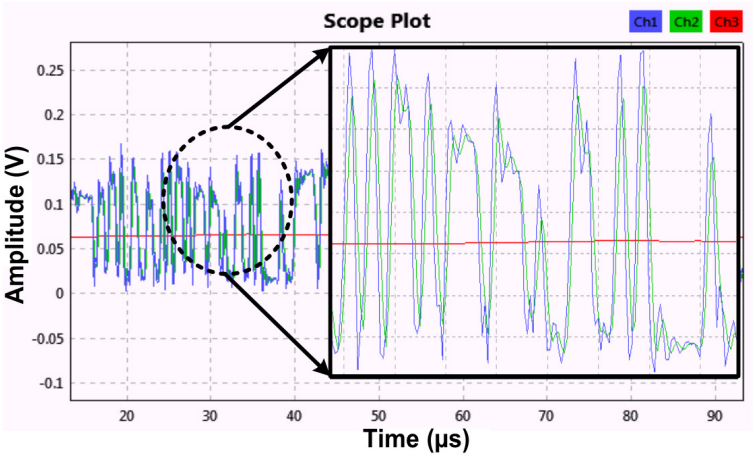

(b)

(c)

Fig. 5.18. (a) Received RF spectrums from WINeRS-8 Tx, which has center frequency of 433.5 MHz with 14 MHz bandwidth, (b) 36 MHz over-sampled transient RF signals after 1st and 2nd moving average filters, respectively. The 1st moving average (green) shows the less noise compared to the original signal (blue) while the adaptive threshold for OOK demodulation is decided by 2nd moving average (red), (c) Recorded signals at Ch. 1 in real-time GUI.

After OOK demodulation based on the adaptive threshold as shown in Fig. 5.17, the recovered packet data is sent to GUI designed by C++ language via ZeroMQ protocol [127] for unpacking packets, which extracts the individual 32-channel data from the packet data in Fig. 5.13. All of the acquired data during the experiment is displayed on the PC screen, and saved in the PC station for post processing. Fig. 5.18c shows the time domain representation of Ch. 1 recorded signal in real time using GUI.

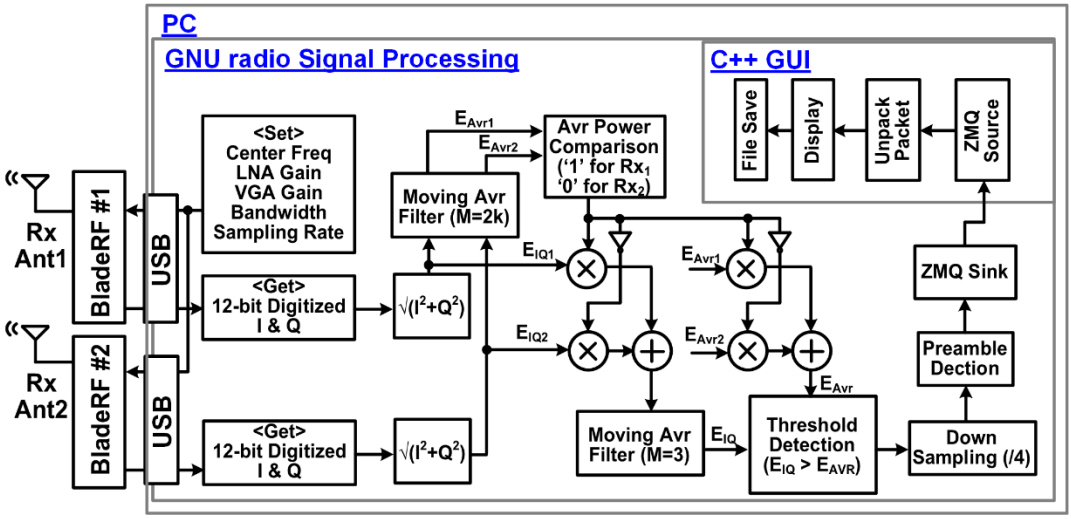

Fig. 5.19. Software subsystem of dual WINeRS-8 receivers for extended coverage of experimental arena without blind spots.

One of the advantages of a SDR receiver compared to a custom-designed receiver is that multiple receivers for providing extended coverage can be easily achieved by adding multiple SDRs including software design without any complex connection between hardware in [94]. Fig. 5.19 shows the software subsystem of the dual WINeRS-8 receiver to increase the wireless coverage of the experimental arena and eliminate blind spots caused by antenna directivity. Moving average of M = 2k compares the average Rx power from Rx antenna #1 and #2, and decides in real time which SDR receiver shows higher signal to noise ratio (SNR) for same transmitted RF signal. Then, one of SDR Rx data, which has higher SNR is demodulated and sent to the GUI. This method can be easily extended to multiple SDR receivers to achieve the robust wideband RF data transmission system over the large experimental arena without blind spots as shown in

Fig. 5.20a while the recovered pre-recorded spike signals filtered by 20 Hz analog HPF in AFE are shown in Fig. 5.21b.

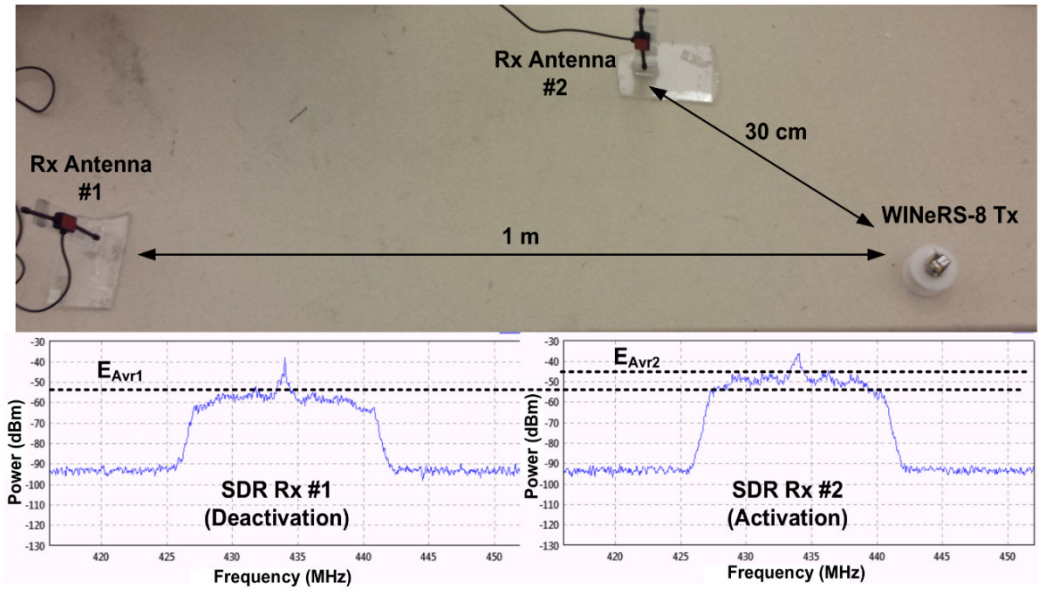

(a)

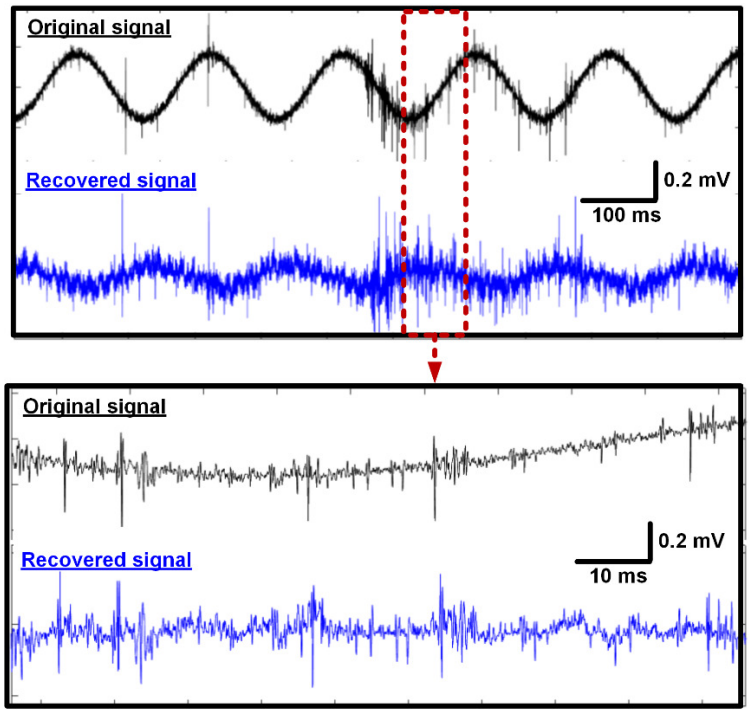

(b)

Fig. 5.20. (a) Test bench of dual SDR receivers with WINeRS-8 transmitter, and (b) recovered pre-recorded spike signals compared to the original signal.

VI. ANIMAL EXPERIMENTS WITH WINERS-8 SYSTEM IN ENERCAGE-HC2 SYSTEM

6.1 *In Vivo* Experiment of WINeRS-8 system for Neural Recording from Freely-Behaving Animal Subject

In order to demonstrate the functionality of the proposed WINeRS-8 system in a real-world experiment, compact WINeRS-8 mobile units for battery-powered and inductively-powered animal experiments were designed as shown in Fig. 6. 1 and 6.2. The battery in the battery-powered headstage can be replaced with one 0.21 F super capacitor in the inductively-powered headstage to supply the WINeRS-8 system when the recovered power is interrupted by >80° tilting of the headstage unit or >18 cm coupling distance from the bottom of the homecage. The L_3 and L_4 coils are optimized for maximizing PTE inside the EnerCage-HC2 [128]. In the experiment setup, the off-the-shelf rectifier (BAS4002, Infineon Tech., German), 2.5 V LDO (MCT1703T, Microchip Tech. Inc., AZ), and MCU (CC2541, Texas Instruments, TX) are included in the headstage to replace the downlink data telemetry in chapter 5.4 with the 2.4-GHz Bluetooth Low Energy (BLE), which is compatible with EnerCage-HC2 system as described in [128]. The weight of the prototype headstage (1.9 cm × 1.9 cm × 3cm) is 5.7g including the package. All experiments were conducted with prior approval from the Institutional Animal Care and Use Committee (IACUC) at Georgia Institute of Technology and Emory University.

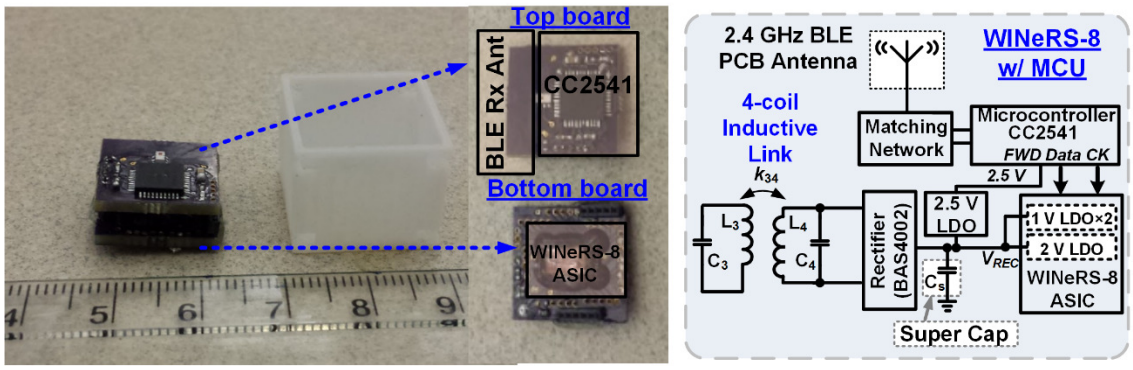

Fig. 6.1. WINeRS-8 headstage equipped with Microcontroller for 2.4 GHz Bluetooth Low Energy for downlink data communication.

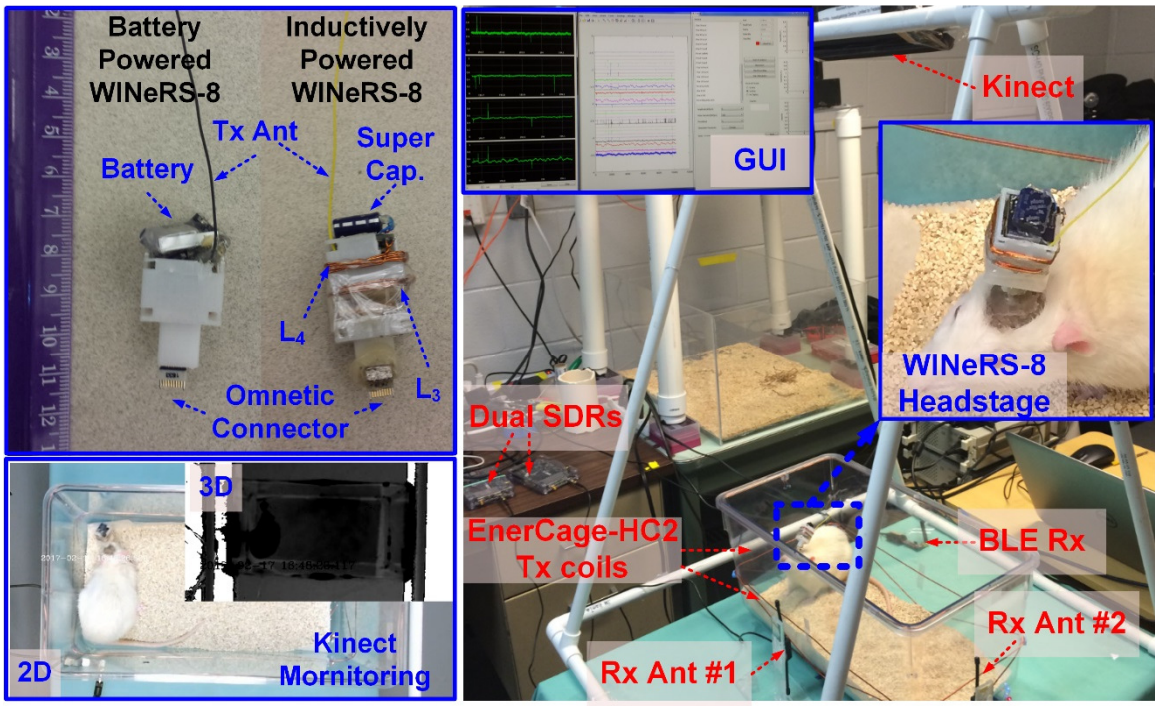

Fig. 6.2. *In vivo* experimental setup for the WINeRS-8 headstage prototype inside the EnerCage-HC2. In this experiment, hippocampal multi-electrode array recording was conducted in CA1 and CA3.

In the *in vivo* experiment, 8 recording electrodes and 8 stimulation electrodes were implanted in the hippocampus of a Sprague-Dawley rat while the 8 recording and 2 stimulation electrodes were connected to WINeRS-8 system to record local field potentials (LFPs). The battery-powered and inductively-powered recordings were compared with the recordings from a commercial hard wired system [129] to verify the functionality of inductively-powered WINeRS-8 system. Fig. 6.2 shows *in vivo* experimental setup for the WINeRS-8 headstage prototype inside the EnerCage-HC2 system for hippocampal multi-electrode array recording in CA1 and CA3 regions. During the experiment, the Kinect performed the automated animal tracking and behavior recognition using 2D color and 3D depth images in real time [130].

The recorded neural waveforms at different times are compared in Fig. 6.3 which has the same range of offline filtering from 20 Hz to 5 kHz for comparison. The hard-wired recording, battery-powered WINeRS-8 recording in standard homecage, and inductively-powered WINeRS-8 recording in the EnerCage-HC2 system from same 8-

channel electrode are shown in Fig. 6.3a, b, and c, respectively. One of the characteristics of this hippocampal multi-electrode array recordings is that the signals from different channels are highly correlated. The spectrograms of the part of recorded signal for ~4 min from selected CA1 and CA3 electrodes, electrode #1 and #2, are shown in Fig. 6.4a for hard-wired recording, Fig. 6.4b for battery-powered WINeRS-8 recording, and Fig. 6.4c for inductively-powered WINeRS-8 recording in the EnerCage-HC2 system, respectively. The processed spectrograms from 20 Hz to 200 Hz shows the similar spectrums of CA1 and CA3 region in the hard-wired recording and battery-/inductively-powered WINeRS-8 recording, demonstrating that the inductively-powered WINeRS-8 system with the EnerCage-HC2 system can replace the conventional hard-wired or battery-powered recording system, which creates an automated enriched environment inside standard homecage for longitudinal electrophysiology and behavioral neuroscience experiments.

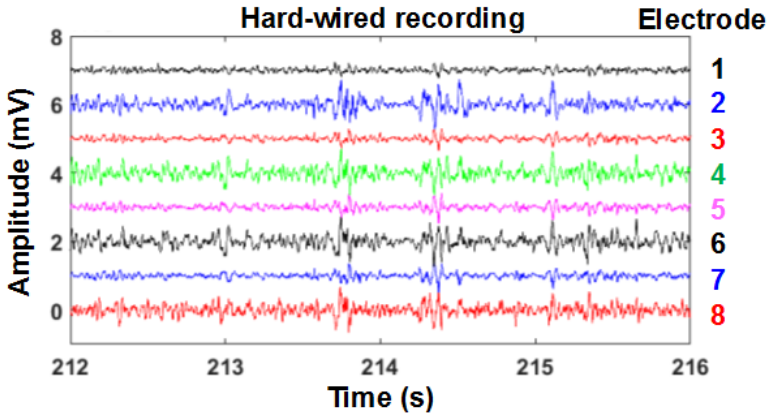

(a)

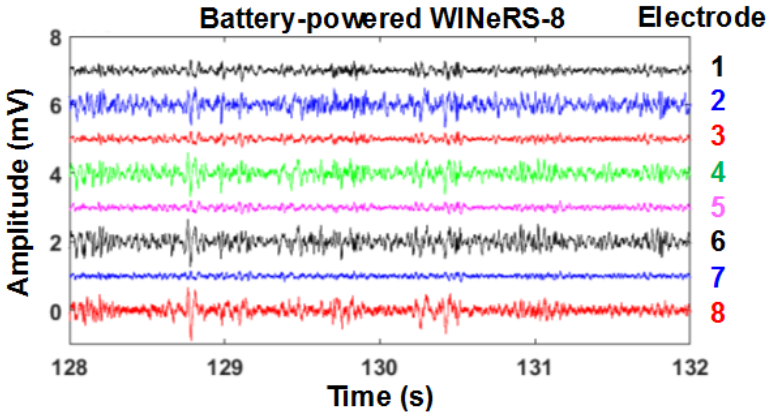

(b)

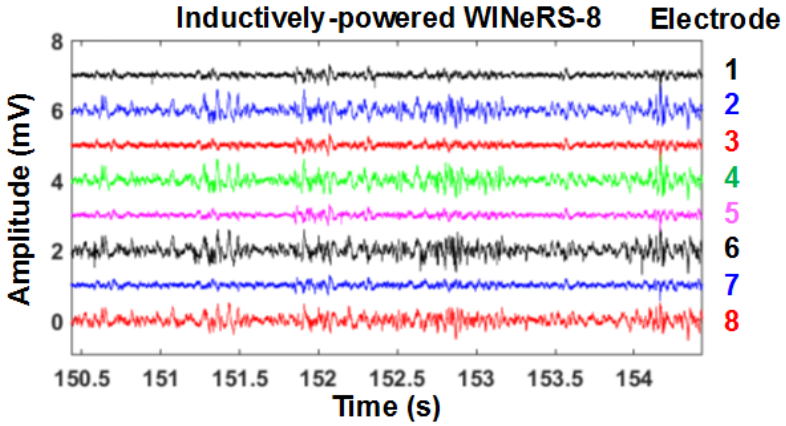

(c)

Fig. 6.3. LFP recording from (a) the hard-wired system, (b) battery-powered WINeRS-8 system, and (c) inductively-powered WINeRS-8 system with a bandwidth from 20 Hz to 10 kHz (The author acknowledges Dr. B. Mahmoudi for helping this animal experiment).

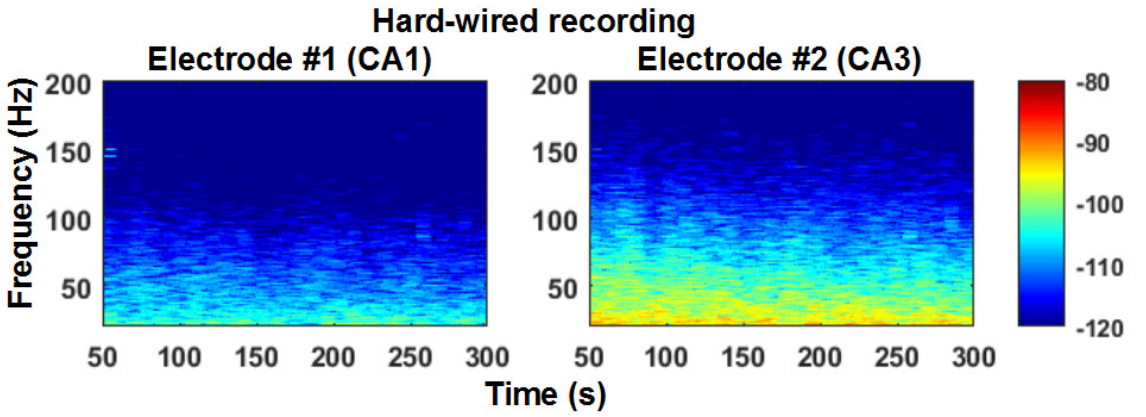

(a)

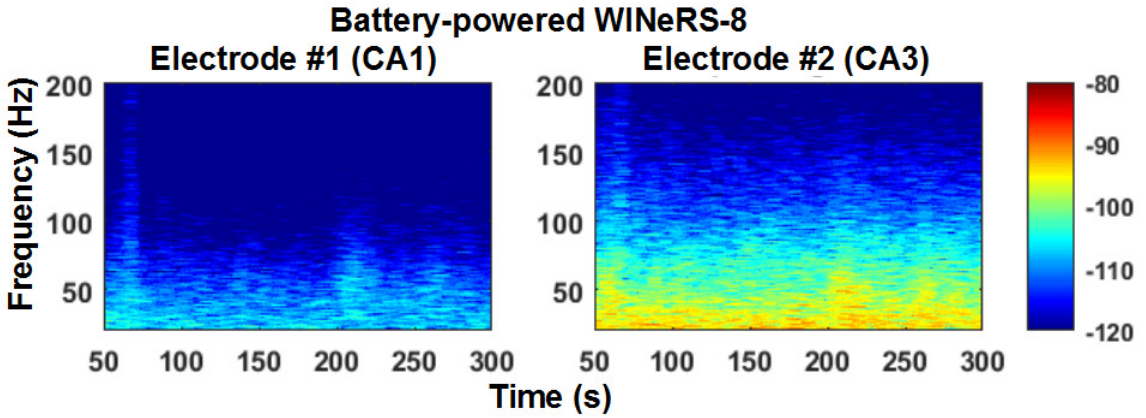

(b)

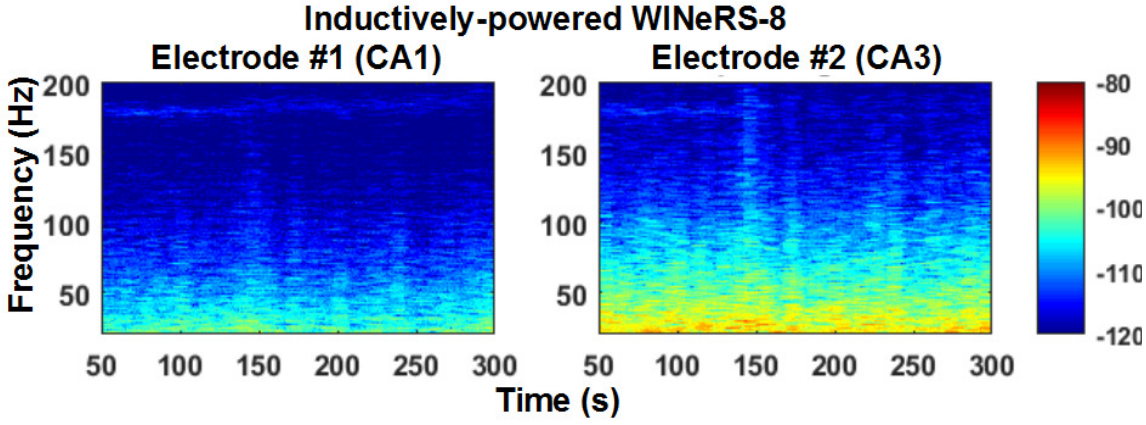

(c)

Fig. 6.4. Spectrograms of the recorded signal between 20 Hz and 200 Hz for ~4 min recording from selected CA1 and CA3 electrodes, electrode #1 and #2 in Fig. 5.22 for (a) hard-wired recording, (b) battery-powered WINeRS-8 recording, and (c) inductively-powered WINeRS-8 recording in the EnerCage-HC2 system.

6.2 *In Vivo* Experiment of WINeRS-8 system for Peripheral Nerve Recording and Stimulation from Freely-Behaving Animal Subject

A neural interface system combined with the peripheral nervous system has benefited from recent advance in a direct communication pathway between the peripheral nervous system and external technologies. The acquired data from efferent and motor potentials is interpreted to provide the meaningful behavior patterns or a variety of sensing feedbacks [131] or to monitor the restoring motor and sensory functions in patients with spinal cord injuries [138].

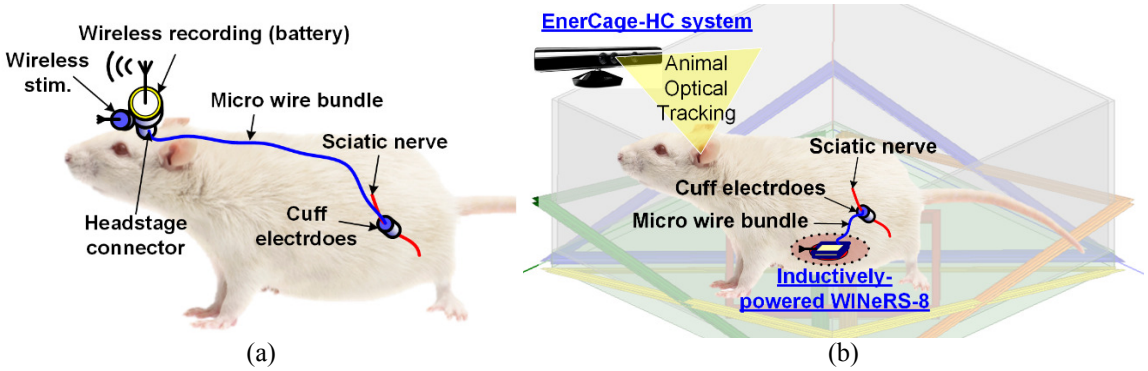

Fig. 6.5. Schematic representation of an animal study using a sciatic nerve model for the peripheral nerve interface using (a) battery-powered recording/stimulation headstages [131][139], and (b) inductively-powered WINeRS-8 system inside the EnerCage-HC system.

Although some selective recording and stimulation from the peripheral nervous system has been performed by the prior works, these devices provide only recording or stimulation capability [106][133][134], need the hard-wired connections [131][135][136], which limits the freely movement of an animal subject, or require the external rendezvous device including the external battery, which should be carried by the rat during the limited time of the experiment [137]. The battery-powered wireless recording and stimulation headstages [139] equipped with implanted micro electrodes have been used to capture the electrophysiological signals of the peripheral nervous system from the freely-moving animal subject as shown in Fig. 6.5a [140]. However, the headstage connector attached to the skull and the implanted long distance of the microwire bundle from the

target peripheral nerves to headstage increase the surgery time as well as difficulties, and eventually exposes the animal subject to the potential infections.

The schematic view of an animal study using a sciatic nerve model for the peripheral nerve interface using the inductively-powered WINeRS-8 system inside the EnerCage-HC system is suggested in Fig. 6.5b. In this *in vivo* test, evoked compound action potential was recorded to verify the stimulation and recording capability of the WINeRS-8 system for the short-term experiment considering the condition of the animal subject. Two different electrode arrays are utilized, which are cuff electrode array for stimulation and penetrating electrode array for recording as shown in Fig. 6.6. Although microchannel scaffold technique in [136] shows much higher quality of the recording than the conventional cuff electrode, it requires at least 4 weeks for regeneration of the nerve. Therefore, the penetrating electrode is utilized in the *in vivo* test to record the stronger evoked action potential compared to the conventional cuff electrode.

The schematic representation of the peripheral neural interface and stimulation/recording electrodes are illustrated in Fig. 6.6a with the sciatic nerve model. The cuff electrodes for 2-ch biphasic stimulation are located at 1 – 2 cm distance from the penetrating recording electrode at lower side of the sciatic nerve on a leg. The penetrating electrodes are composed of three layers, which are 0.2 mm, 0.7 mm, and 1.2 mm depth, respectively, considering the typical thickness of Epineurium and Perineurium in the nerve. However, since these recording electrodes still have contact with the penetrated axons, these recording electrodes become highly correlated. Fig. 6.6b shows the 32-ch penetrating recording electrode array and 2-ch biphasic cuff electrode array at the sciatic nerve, where the electrodes are connected to 75 μm thick micro wire bundles (Stablohm 800A, California fine wire). The empty tube was removed after surgery.

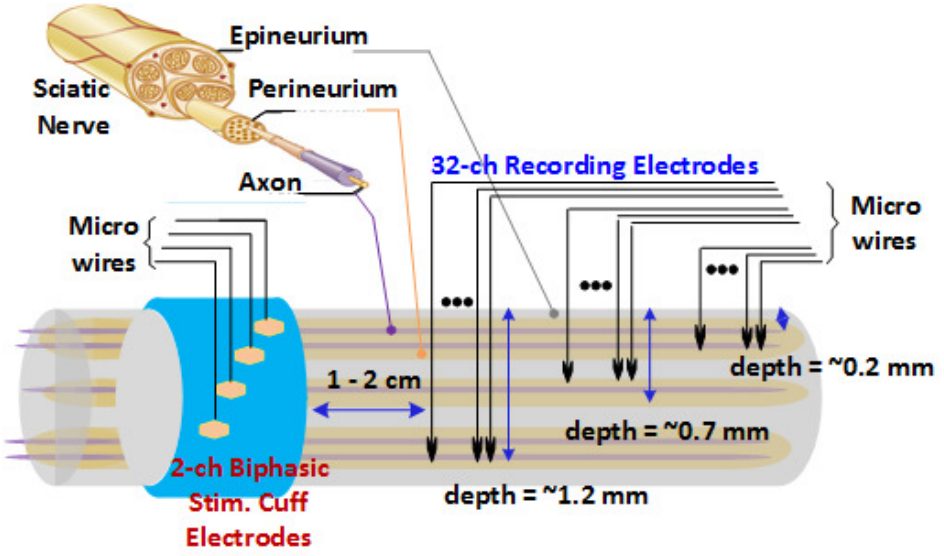

(a)

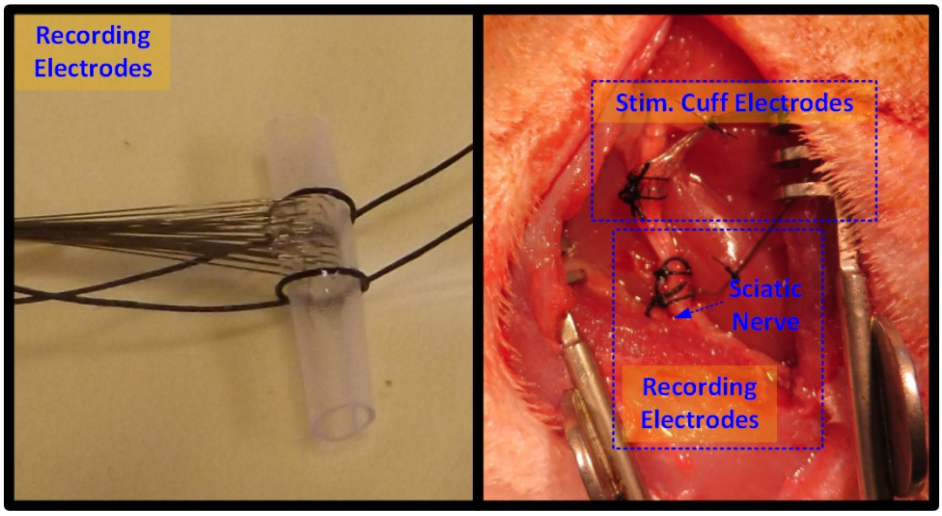

(b)

Fig. 6.6. (a) the schematic representation of the peripheral neural interface and stimulation/recording electrodes with the sciatic nerve model and (b) 32-ch penetrating recording electrode array and 2-ch biphasic cuff electrode array at the sciatic nerve of the rat (Empty tube was removed after surgery).

The following steps of *in vivo* experiment procedures are conducted to fully verify the system-on-chip inductively-powered WINeR-8 ASIC for the suggested peripheral nerve interface in Fig. 6.5b. All experiments were conducted with prior approval from the Institutional Animal Care and Use Committee (IACUC) at Georgia Institute of Technology and University of Texas Rio Grande Valley.

1. Recording/stimulation using two commercial headstages (TBSI w-32 wireless recording & TBSI S2W stimulator, TBSI, Durham, NC).
2. Recording/stimulation using a battery-powered WINeRS-8 headstage with MCU implementation (type-I) as shown in Fig. 6.2.
3. Recording/stimulation inside the EnerCage-HC using an inductively-powered WINeRS-8 headstage with MCU implementation (type-II) as shown in Fig. 6.2 and 6.7a.
4. Recording/stimulation inside the EnerCage-HC using an inductively-powered WINeRS-8 headstage equipped with system-on-chip WINeRS-8 ASIC (type-III) as shown in Fig. 5.2 and 6.7b.
5. Recording/stimulation inside the EnerCage-HC using an inductively-powered implanted WINeRS-8 with MCU implementation (type-IV) as shown in Fig. 6.7c.
6. Recording/stimulation inside the EnerCage-HC using an inductively-powered implanted WINeRS-8 equipped with system-on-chip WINeRS-8 ASIC (type-V) as shown in Fig. 6.7d.

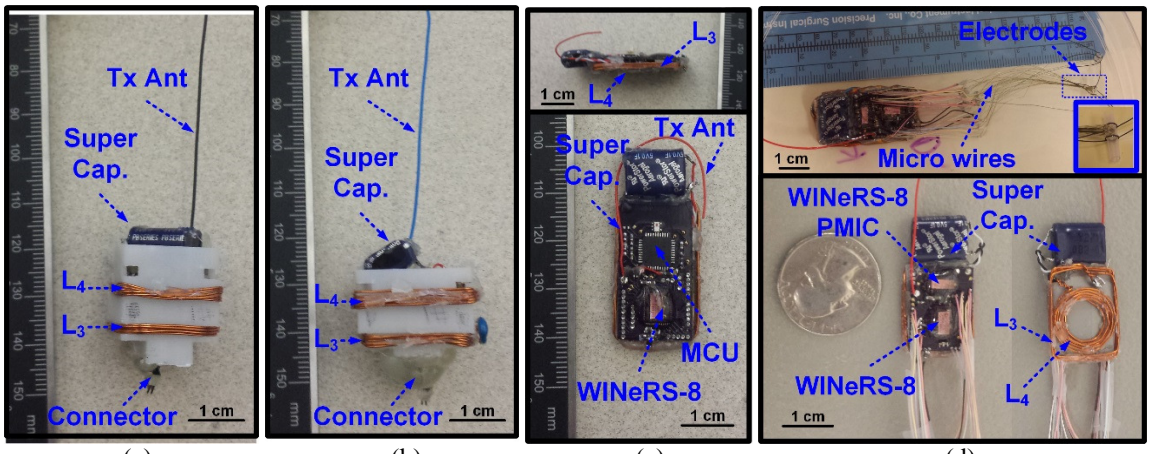

Fig. 6.7. Inductively-powered WINeRS-8 prototypes for 32-ch peripheral nerve recording and 4-ch stimulation: (a) headstage with MCU/external rectifier (type-II), (b) headstage system-on-chip (type-III), (c) implantable WINeRS-8 with MCU/external rectifier (type-IV), and (d) implantable system-on-chip WINeRS-8 without any external active components (type-V).

Fig. 6.7 shows the different type of the WINeRS-8 headstage and implant prototypes used in the *in vivo* test of the peripheral nerve interface. The type-I headstage prototype equips a battery instead of the super capacitor to test the functionality without the EnerCage-HC system. Since the overall board size becomes too large for the implantable PCB board due to the pad connections, the part of WINeRS-8 rectifier with the forward telemetry recovery block is diced (see Fig. 5.2b) and connected to main WINeRS-8 block via the external PCB connections as shown in Fig. 6.7d for type-III and IV. The rectifier with the forward telemetry block in WINeRS-8 ASIC is replaced with the commercial rectifier to operate the MCU in type-II and IV, which has higher voltage rating than WINeRS-8 rectifier. The schematic of WINeRS-8 type-II and IV is already shown in Fig. 6.1. The weight of type-IV prototype (4 cm × 1.5 cm × 0.5 cm) is 3.7 g, and the weight of type-V prototype (3 cm × 1.5 cm × 0.5 cm) with 2.8 g weight including the super capacitor (0.21 F) and Rx coils (L_3, L_4). The power dissipation of WINeRS-8 ASIC is 18.9 mW while the implemented MCU consumes separate power of 16.1 mW for BLE interface with 2.5 V supply voltage.

In vivo experimental setup and the recorded waveforms for the WINeRS-8 type-I prototype on the treadmill is shown in Fig. 6.8a. In this experiment, the stimulation is performed periodically to encourage the treadmill locomotion of the rat for the peripheral nerve recording. The measurement waveforms were synchronized to video records, which temporarily replaced the function of the Kinect equipped in the EnerCage-HC system. The acquired compound evoked action potential from the WINeRS-8 headstage is compared to the recording result from the commercial headstage (TBSI w-32 wireless recording & TBSI S2W stimulator) is shown in Fig. 6.8b. The compound evoked signal from the peripheral nerves can be observed in 5 ms ~ 10 ms after the stimulus artifact in both commercial and WINeR-8 headstage considering that velocity of the action potential for sciatic nerve in the injured condition (~2 m/s to ~30 m/s). Thanks to the stimulus artifact rejection described in chapter 5.3, the stimulus artifact in WINeRS-8 in Fig. 6.8a

shows the smaller amplitude than the stimulus artifact in the commercial recording/stimulation headstage (Fig. 6.8b).

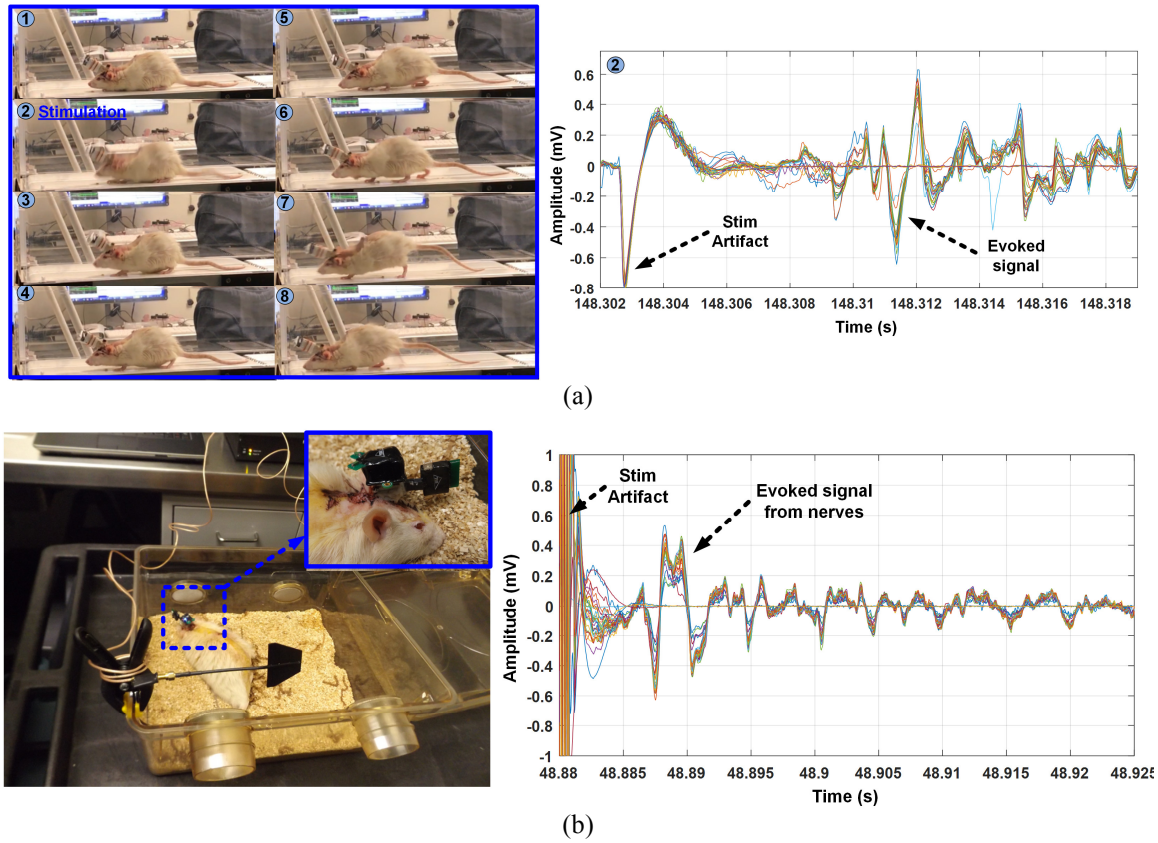

Fig. 6.8. *In vivo* experimental setup of (a) the battery-powered WINeRS-8 headstage prototype (type-I) for treadmill locomotion with the acquired evoked signal from the peripheral nerve, and (b) the commercial recording/stimulation with the resulted evoked signal (The author acknowledges Dr. Y. Choi for helping this animal experiment).

The experimental setup for the inductively-powered WINeRS-8 headstage (type-II & III) inside the EnerCage-HC2 system is shown in Fig. 6.9a and the 32-ch recorded evoked signal after the biphasic stimulation from the freely-moving rat is shown in Fig. 6.9b. In this stimulation and recording experiment, the stimulation parameters are changed to observe the behavioral change of the rat. When the rat showed the distinguishable behavioral response from each stimulation trial, we recorded the compound evoked signal from the peripheral nerves as shown in Fig. 5.26b.

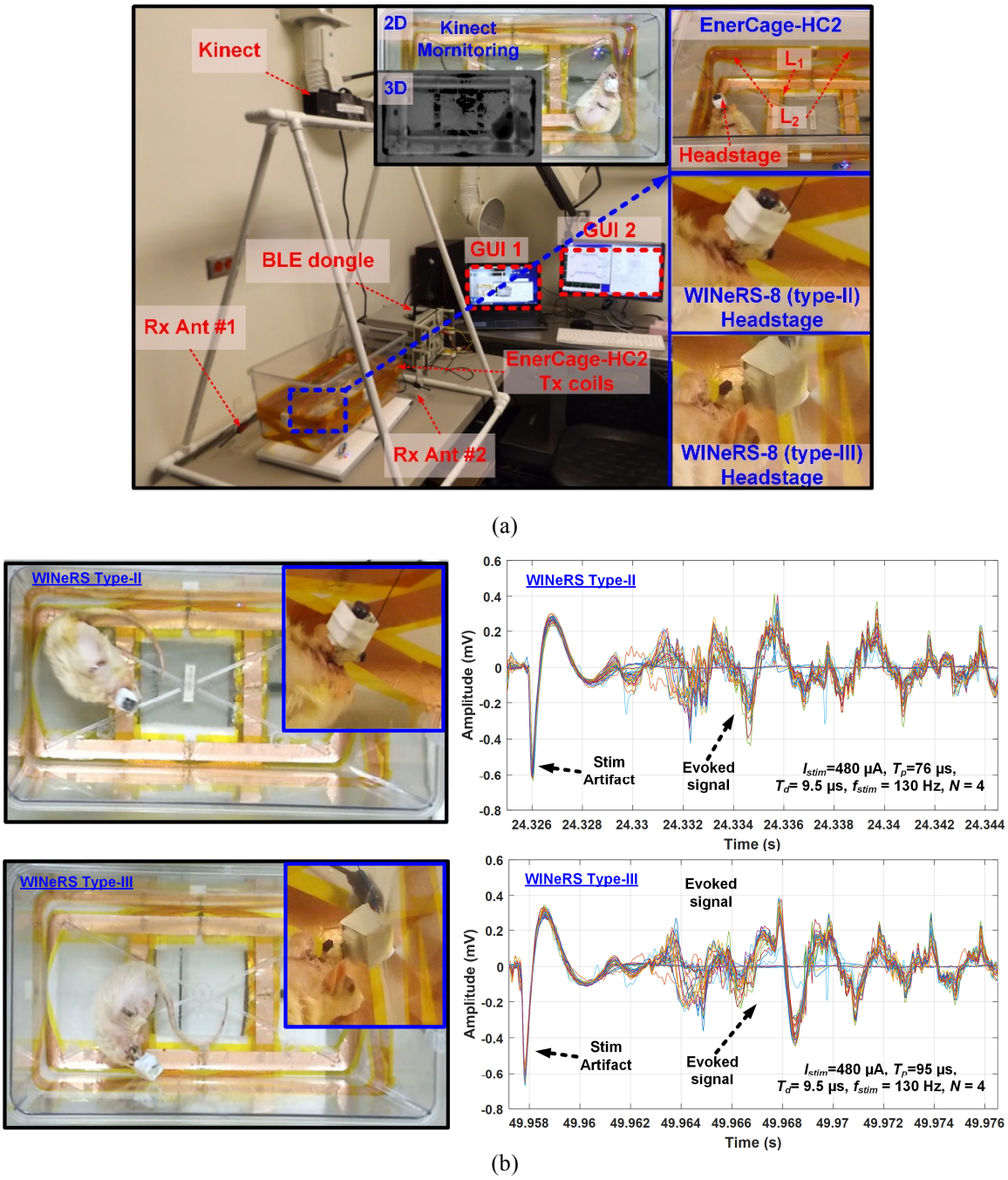

Fig. 6.9. (a) *In vivo* experimental setup of the inductively-powered WINeRS-8 headstage prototype (type-II and III) for recording/stimulation from the freely-moving rat in the EnerCage-HC2 system, and (b) recorded evoked signal after biphasic stimulation from type-II and III headstage, respectively.

Since the functionality differences in WINeRS-8 type-I to V are PCB board configuration for headstage or implant device (type-I, II, III vs. type-IV, V) and the external MCU/rectifier or system-on-chip rectifier with the near field data

communication block (type-I, II, IV vs. type-III, V), the stimulation and recording functionality in all types of WINeRS-8 board shows the same property. The experiment result in Fig. 6.9b also proves that the proposed near-field data communication between EnerCage-HC2 and WINeRS-8 system described in chapter 5.4 can replace the commercial BLE communication, resulted in the power saving of 16.1 mW in the MCU.

The implanted WINeRS-8 system were also tested under the same experimental setup as shown in Fig. 6.10a. The WINeRS-8 prototypes (type-IV, V) in Fig. 6.7c and d were implemented near the belly of the rat, and the stimulation/recording electrodes are directly connected to the board using the micro wire bundle as described in Fig. 6.5b. The experimental results in Fig. 6.10a, which shows similar pattern of compound evoked spike after the stimulation compared to the previous experiments, demonstrate that the WINeRS-8 system implanted near the belly of the rat is fully functional inside the EnerCage-HC2 system, providing continuous inductive-powered recording and stimulation with the real-time animal tracking by Kinect as shown in Fig. 6.10b.

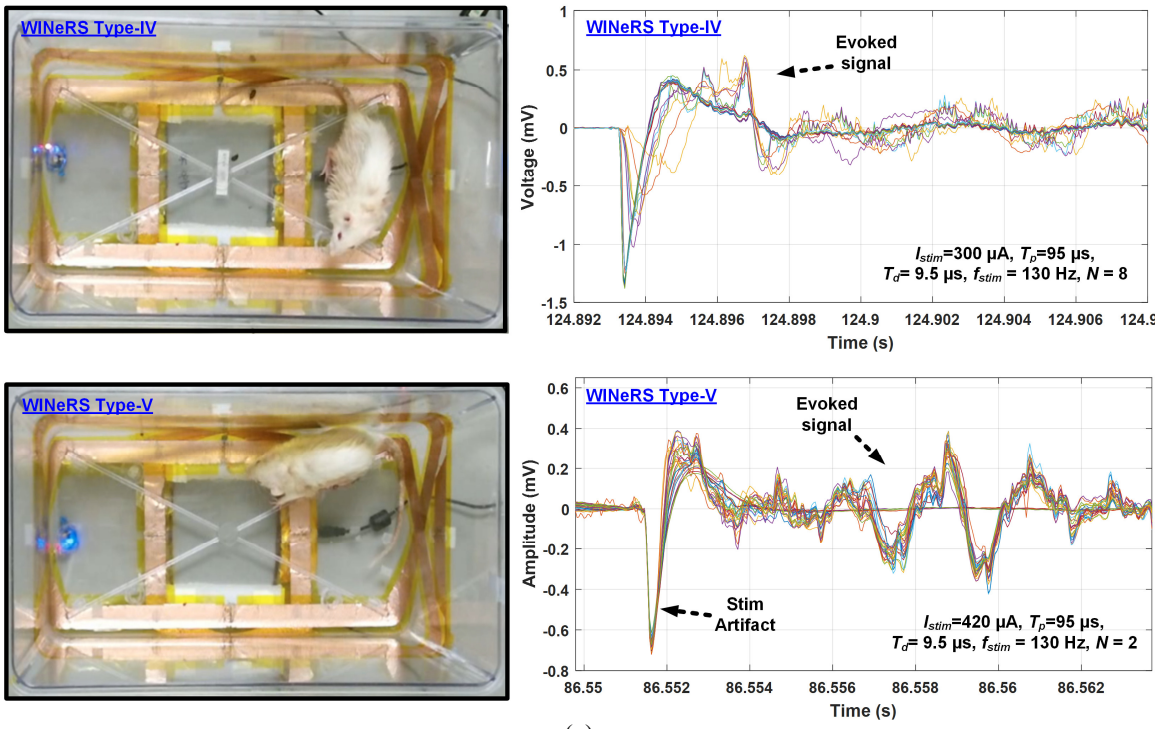

(a)

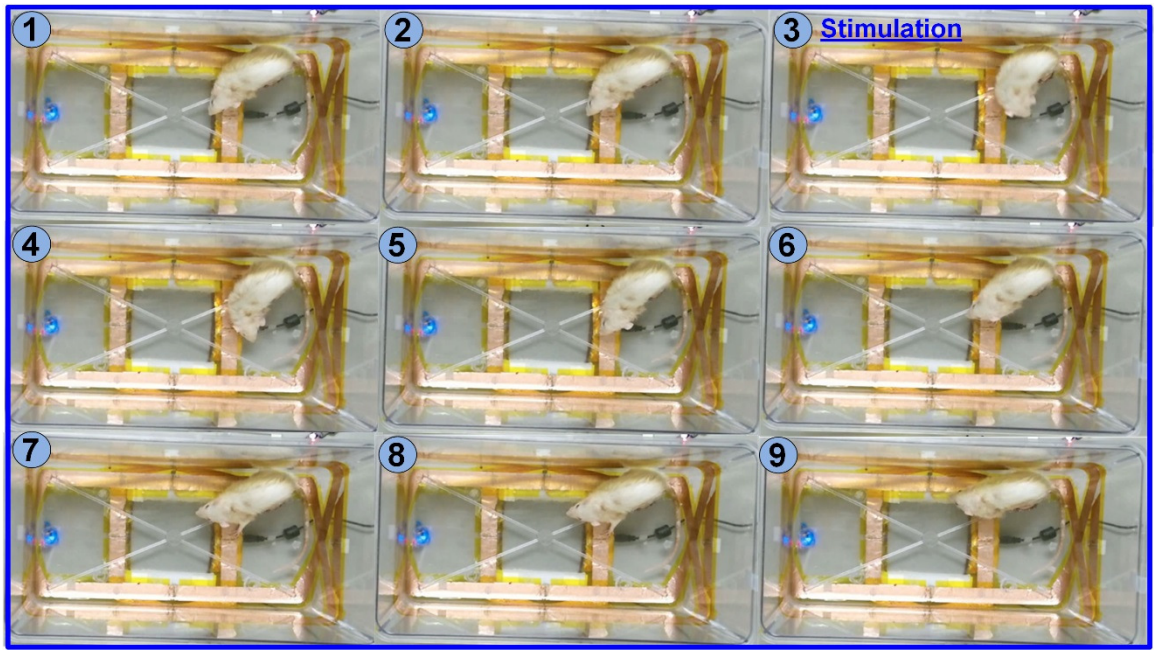

(b)

Fig. 6.10. (a) Recorded evoked compound action potential after biphasic stimulation using the implanted WINeRS-8 system, and (b) the behavior change in the rat captured by Kinect in EnerCage-HC2 system (2.3 frame/s).

VII. CONCLUSIONS AND FUTURE WORKS

This dissertation focused on developing the smart solutions by utilizing innovative system-, package-, and circuit-level designs with analog and digital circuit technique combined with high-performance wireless power and data transmission to implantable biomedical Microsystems, which has resulted in several conference and journal publications [11], [74], [82]-[84], [91], [100], [102]. Several techniques in wireless power transmission system such as triple loop wireless, multi-cycle Q-modulation, and three-phase time-multiplexing power wireless power transmissions could significantly increase the PTE of power transfer link in the presence of various disturbances from inside (e.g. sudden loading variations) and outside (e.g. body movements, changes in surrounding tissue morphology, flexible coil deformations, angular coil misalignment, and nearby conductive objects) the system in real-time. The EnerCage-HC system also creates an automated enriched environment inside standard homecage for long-term electrophysiology experiments while it eliminates cables from the electro-physiology experiments without adding the burden of carrying large battery payloads on the freely behaving animal subjects, or shortening the duration of the trial. The WINeRS-8 system equipped with 32-ch adaptive recording channel and 4-ch biphasic stimulation was designed to enable closed-loop recording and stimulation for both central and peripheral nervous system inside the EnerCage-HC2 system. A robust wirelessly-powered recording and stimulation system for a freely moving animal subject was fully verified by two in-vivo tests in this dissertation, which are LPF recording and sciatic nerve stimulation/recording inside the EnerCage-HC2 system. This chapter summarizes the results and scientific contributions of this dissertation and proposes the future works.

7.1 Conclusions

7.1.1 High-Efficiency and Adaptive Wireless Power Transmission System

A standalone triple-loop wireless power transmission system has been demonstrated for dynamic applications in variable environments, such as implantable biomedical devices. The proposed system includes three loops to adaptively tune Tx and Rx LC-tanks to the power carrier frequency and also adjust the transmitted power in the presence of coils' coupling variations. A sequential control algorithm has been devised to activate these three loops, while maintaining the stability of the power transmission link. The system dynamically maximizes the PTE of the inductive link in the presence of various disturbances from inside (e.g. sudden loading variations) and outside (e.g. body movements, changes in surrounding tissue morphology, flexible coil deformations, and nearby conductive objects) the system in real-time. The prototype Tx is built around a COTS RFID with custom circuitry for the TRC. The Rx was built around a custom-designed ASIC that includes a high efficiency active rectifier, a regulator, a back telemetry circuit, and the ART. To further increase the PTE, a 3-coil inductive link was designed with optimal geometry and used in our measurements. Results showed that the proposed triple loop power transmission system was stable in various conditions, and responds as planned to the parasitic capacitors added to the Tx and Rx tank circuits and coupling variations, while significantly improving the PTE [83].

A new multi-cycle Q-modulation method is also presented, which can maintain the high PTE in wirelessly powered applications that operate in dynamic environments with motion and variable loading, such as implantable medical devices. The proposed multi-cycle Q-modulation circuit can be easily implemented on the Rx side of conventional 2-coil links either in the form of an ASIC or using COTS components, without any complex circuity or fast switching operation, needed in the conventional Q-modulation technique. Moreover, the proposed technique does not need sophisticated synchronization between the power carrier and Q-modulation switching signals, which

facilitate its applicability to wireless links with higher power carrier frequencies. We have also demonstrated usage of the ART along with the new multi-cycle Q-modulation to dynamically maintain the PTE of the inductive link at its peak in the presence of disturbance in the surrounding environment or manufacturing process variations, which can otherwise significantly degrade the PTE by detuning the Rx LC-tank. Thanks to their simplicity, these methods can be extended to a wide variety of applications, utilizing the 2-coil inductive links in wide ranges of loading, separation, misalignment, and environmental variations [84].

7.1.2 Toward A Three-Phase Time-Multiplexed Planar Power Transmission to Distributed Implants

A novel WPT platform has been presented in this chapter that is suitable for a large number of receivers, distributed over an extended area. The proposed three-phase TDM transmitter takes advantage both timing of the excitation carrier signals and geometrical arrangement of a three-layer overlapping hex-PSC array to create a homogenously powered 3D volume that would be robust against arbitrary angular or spatial misalignments of the Rx. The transmitter includes time multiplexed CMCD PAs and a three-phase sinusoidal carrier signal to generate both vertical and lateral magnetic flux to compensate for the angular misalignment of the Rx coils. The functionality of three-phase TDM Tx was demonstrated in both simulation and measurements in comparison to a simple in-phase transmitter by delivering 5.4 mW to the Rx in a worst-case scenario with 90° angular misalignment. The proposed WPT architecture is applicable to distributed implants and other wireless powering applications, in which a large number of receivers with arbitrary angular and spatial misalignments need to be continuously powered [91].

7.1.3 Wirelessly-Powered Homecage System (EnerCage-HC) For Long-Term Behavioral Experiments

A novel wireless platform for electrophysiology experiments inside the standard homecage has been presented. This system, called the EnerCage-HC, takes advantage of multi-coil coupling and Kinect® based optical localization to offer an efficient and low-cost technology for wireless powering any electronics attached to a small animal subject and track its behavior. The EnerCage-HC includes four switchable slanted triangular WWCs covering lower corners of the homecage by establishing 4-coil power transfer as well as a square-shaped WWC at the bottom of the cage for 3-coil power transfer in the center. The Kinect tracking algorithm is key to achieve the switchable 3-/4-coil function, which in turn allows the use of only one PA in the system, which significantly reduces the system complexity, cost, and heat dissipation. The 3-/4-coil mechanism achieves three times higher and more homogeneous PTE in the homecage compared to the conventional single WWC. A PMIC is used in the mobile unit to offer high efficiency voltage rectification/regulation, and communication between mobile and stationary units for closed-loop power control. The functionality of the EnerCage-HC prototype was demonstrated in both bench-top and *in vivo* experiments. To the best of our knowledge, the EnerCage-HC system is the first wirelessly powered cage equipped with the tracking functions for both animal position and orientation. It has the ability to create an automated enriched environment inside standard homecage for long-term electrophysiology experiments [100].

7.1.4 Wireless Implantable Neural Recording and Stimulation (WINeRS-8) System in EnerCage-HC System

A completed inductively-powered wireless implantable neural recording and stimulation system, called WINeRS-8 is presented for longitudinal electrophysiology and behavioral neuroscience experiments fully compatible with the EnerCage-HC system. The WINeRS-8 system equips 32-channel adaptive averaging low noise analog front-end

(AFE) and 4-ch biphasic stimulation, which is suitable for central and peripheral nerve recording applications. An integrated adaptive averaging AFE architecture has been proposed for applications in which input referred noise need to be adjusted based on input signal conditions, such as recording from visceral neural networks. The proposed AFE is equipped with DC-coupled doubled input g_m LNA to increase the NEF while maintaining high input impedance in a structure without AC-coupling capacitors or chopper modulation. The proposed architecture provides higher SNR particularly for multichannel recording from CNS and PNS with flexibility to dedicate the AFE resources to input channels with the most viable and information-rich input signals in various neuroprosthetic or electrophysiology recording applications. The robust data communication method is also developed for uplink and downlink data communications between WINeRS-8 and EnerCage-HC2 systems utilizing multi software-defined radio (SDR), Bluetooth low energy (BLE), and OOK-PPM modulation. In two *in vivo* experiments, five types of WINeRS-8 headstage and implantable device are designed to demonstrate the recording and stimulating functionalities for the central/peripheral nervous system in the EnerCage-HC2 system. To the best of our knowledge, the proposed WINeRS-8 system is the first wirelessly powered implanted device without the battery for the central and peripheral nerve recording/stimulation on a freely-moving animal subject while providing the tracking functions.

7.2 Future Works

Several research groups have considered using real-time closed-loop stimulation based on the incoming information provided by the recording channels. However, these efforts are still at early stages and their possible applications for central and peripheral nervous systems have not been fully explored. Although WINeRS-8 system equips both recording and stimulation functionalities, the real-time algorithm to filtering, sorting, clustering the incoming neural data is still necessary to enable the real-time closed-loop stimulation.

Although the PLL-based OOK transmitter and commercial software defined ratio (SDR) multi-receivers are considered to achieve the robust wideband RF data transmission system for high channel count wireless neural recording data transmission, the current signal processing of RF data in GNU radio software adds the burden to the hardware due to its large number of complex calculations in the PC. Therefore, the number of SDR receivers to increase the coverage of RF data transmission is limited by the performance. To address this issue, the FPGA implementation for RF signal processing is required, which is currently performed by the GNU radio.

The proper RF antenna design and matching circuit is also an important issue for the implanted device inside and around the body. While the proposed triple loop power transmission system provides the power coil with the automatic resonance tuning, the RF antenna also needs additional automated matching circuit considering the environment variations inside the animal body.

REFERENCES

[1] J. R. Manns and H. Eichenbaum, “A congnitive map for object memory in the hippocampus,” *Learning Memory*, vol. 16, no. 10, pp. 616-624, Sep. 2009.

[2] A. M. Sodagar, G. E. Perlin, Y. Yao, K. Najafi, and K. D. Wise, “An implantable 64-channel wireless microsystem for single-unit neural recording,” *IEEE J. Solid-State Circuits*, vol. 44, no. 9, pp. 2591–2604, Sep. 2009.

[3] T. A. Szuts, V. Fadeyev, S. Kachiguine, A. Sher, M. V. Grivich, M. Agrochao, P. Hottowy, W. Dabrowski, E. V. Lubenov, A. G. Siapas, N. Uchida, A. M. Litke, and M.Meister, “A wireless multi-channel neural amplifier for freely moving animals,” *Nature Neurosci*., vol. 14, no. 2, pp. 263–269, Feb. 2011.

[4] E. Greenwald, M. Mollazadeh, C. Hu, W. Tang, E. Culurciello, and N. V. Thakor, “A VLSI neural monitoring system with ultra-wideband telemetry for awake behaving subjects,” *Trans. Biomed. Circuits Syst*., vol. 5, no. 2, pp. 112–119, Apr. 2011.

[5] R.E. Millard and R.K. Shepherd, “A fully implantable stimulator for use in small laboratory animals,” *J. Neuroscience Methods*, vol. 166, pp. 168-177, July 2007.

[6] B. Lenaerts and R. Puers, "Inductive powering of a freely moving system," *Sensors and Actuators A: Physical,* vol. 123-124, pp. 522-530, Mar. 2005.

[7] P. Cong, N. Chaimanonart, W. Ko, and D. Young, “A wireless and batteryless 130mg 300μW 10b implantable blood-pressure-sensing microsystem for real-time genetically engineered mice monitoring”, *Digest of technical papers IEEE Intl. Solid State Cir. Conf.*, pp. 428-429, Feb. 2009.

[8] VitalView Animal Monitoring Products, Starr Life Sciences Corp. [Online]. Available: http://starrlifesciences.com/

[9] W-series, [Online]. Available: http://www.trianglebiosystems.com/

[10] C. T. Wentz, J. G. Bernstein, P. Monahan, A. Guerra, A. Rodriguez, and E. S. Boyden, “A wirelessly powered and controlled device for optical neural control of freely-behaving animals,” *J. Neural Eng.*, vol. 8, no. 4, pp. 424–436, Jun. 2011.

[11] B. Lee, M. Kiani, and M. Ghovanloo, “A Smart Homecage System with 3D Tracking for Long-Term Behavioral Experiments,” *Proc. IEEE 36st Eng. in Med. and Biol. Conf.*, pp. 3134-3137, Aug. 2014.

[12] G. Lazzi, “Thermal effects bioimplants,” *IEEE Eng. Med. Biol. Mag.*, vol. 24, no. 5, pp. 75–81, Sep. 2005.

[13] G. M. Clark*, Cochlear Implants: Fundamentals and Applications.* Berlin, Germany: Springer-Verlag, 2003.

[14] J. Hirai, T. W. Kim, and A. Kawamura, “Study on intelligent battery charging using inductive transmission of power and information,” *IEEE Trans.Power Electron.*, vol. 15, no. 2, pp. 335–345, Mar. 2000.

[15] R. R. Harrison, P. T. Watkins, R. J. Kier, R. O. Lovejoy, D. J. Black, B. Greger, and F. Solzbacher, “A low-power integrated circuit for a wireless 100-electrode neural recording system,” *IEEE J. Solid-State Circuits*, vol. 42, no. 1, pp. 123–133, Jan. 2007.

[16] M. Ortmanns, M. Gehrke, and H. Tiedtke, “A 232-channell epiretinal stimulator ASIC,” *IEEE J. Solid-State Circuits*, vol. 42, no. 12, pp. 2946-2956, Dec. 2007.

[17] L. H. Jung, N. Shany, A. Emperle, T. Lehmann, P. B. Preston, N. H. Lovell, and G. J. Suaning, “Design of safe two-wire interface-driven chip-scale neurostimulator for visual prosthesis,” *IEEE J. Solid-State Circuits*, vol. 48, no. 9, pp. 2217-2229, Sep. 2013.

[18] Y. K. Lo, K. Chen, P. Gad, and W. Liu, “A fully-integrated high-compliance voltage SoC for epi-retinal and neural prostheses,” IEEE Trans. Biomed. Circuits Syst., vol. 7, no. 6, pp. 761-772, Dec. 2013.

[19] K. Finkenzeller*, RFID-Handbook*, 2nd ed. Hoboken, NJ: Wiley, 2003.

[20] Wang, Chwei-Sen, Oskar H. Stielau, and Grant A. Covic. "Design considerations for a contactless electric vehicle battery charger." *IEEE Trans. Industrial Electron.*, vol. 52, no. 5, pp. 1308-1314, Oct. 2005.

[21] J. Hirai, T. W. Kim, and A. Kawamura, "Study on intelligent battery charging using inductive transmission of power and information," *IEEE Trans. Power Electron*., vol. 15, no. 2, pp. 335–345, Mar. 2000.

[22] M. Kiani, U. Jow, and M. Ghovanloo, "Design and optimization of a 3-coil inductive link for efficient wireless power transmission," *IEEE Trans. Biomed. Circuits Syst.,* vol. 5, no. 6, pp. 579–591, Dec. 2011.

[23] M. Kiani, and M. Ghovanloo, "The circuit theory behind coupled-mode magnetic resonance-based wireless power transmission," *IEEE Trans. Circuits Syst. I, Reg. Papers*, vol. 59, no. 9, pp. 2065–2074, Sep. 2012.

[24] A. K. RamRakhyani and G. Lazzi, "On the design of efficient multi-coil telemetry system for biomedical implants," *IEEE Trans. Biomed. Circuits Syst.,* vol. 7, no. 1, pp. 11–23, Feb. 2013.

[25] U. Jow and M. Ghovanloo, "Design and Optimization of Printed Spiral Coils for Efficient Transcutaneous Inductive Power Transmission," *IEEE Trans. Biomed. Circuits Syst.,* vol. 1, no. 3, pp. 193–202, Sep. 2007.

[26] U. Jow and M. Ghovanloo, "Modeling and optimization of printed spiral coils in air, saline, and muscle tissue environments," *IEEE Trans.Biomed. Circuits Syst.,* vol. 3, no. 5, pp. 339–347, Oct. 2009.

[27] W. H. Ko, S. P. Liang, and C. D. F. Fung, "Design of radio-frequency powered coils for implant instruments," *Med. Biol. Eng. Comput.*, vol. 15, pp. 634–640, 1977.

[28] N. N. Donaldson and T. A. Perkins, "Analysis of resonant coupled coils in the design of radio frequency transcutaneous links," *Med. Biol. Eng. Comput.*, vol. 21, no. 5, pp. 612–627, Sep. 1983.

[29] W. J. Heetderks, "RF powering of millimeter and submillimeter-sized neural prosthetic implants," *IEEE Trans. Biomed. Eng.*, vol. 35, no. 5, pp. 323–327, May 1988.

[30] M. W. Baker and R. Sarpeshkar, "Feedback analysis and design of RF power links for low-power bionic systems," *IEEE Trans. Biomed. Circuits Syst.*, vol. 1, no. 1, pp. 28–38, Mar. 2007.

[31] S. O'Driscoll, A. Poon, and T. H. Meng, "A mm-Sized Implantable Power Receiver with Adaptive Link Compensation," *ISSCC Dig. Tech. Papers*, pp. 294-295, Feb. 2009.

[32] H. Xu, U. Bihr, J. Becker, and M. Ortmanns, "A multi-channel neural stimulator with resonance compensated inductive receiver and closed loop smart power management," *Proc. of IEEE ISCAS*, pp. 638-641, May 2013.

[33] P. Si, A. P. Hu, S. Malpas, and D. Budgett, "A frequency control method for regulating wireless power to implantable devices," *IEEE Trans. Biomed. Circuits Syst.,* vol. 2, no. 1, pp. 22–29, Mar. 2008.

[34] S, Lee, J. Yoo, H. Kim, and H. J. Yoo "A dynamic real-time capacitor compensated inductive coupling transceiver for wearable body sensor network," Proc. Symp. VLSI Circuits, pp. 42-43, Jun. 2009.

[35] A. P. Sample, D. A. Meyer, and J. R. Smith, "Analysis, experimental results, and range adaptation of magnetically coupled resonators for wireless power transfer," *IEEE Trans. Ind. Electron*., vol. 58, no. 2, pp. 544–554, Feb. 2011.

[36] G. Wang, W. Liu, M. Sivaprakasam, and G. A. Kendir, "Design and analysis of an adaptive transcutaneous power telemetry for biomedical implants," *IEEE Trans. Circuits Syst. I*, vol. 52, no. 10, pp. 2109–2117, Oct. 2005.

[37] M. Kiani, M. Ghovanloo, "An RFID-based closed-loop wireless power transmission system for biomedical applications," *IEEE Trans. Circuits Syst. II,* vol. 57, no. 4, pp. 260–264, Apr. 2010.

[38] M. Kiani, K. Y. Kwon, F. Zhang, K. Oweiss, and M. Ghovanloo, "Evaluation of a closed loop inductive power transmission system on an awake behaving animal subject," *in Proc. IEEE 33rd Eng. Med. Biol. Conf.*, pp. 7658–7661, Sep. 2011.

[39] N.Y. Kim, K.Y. Kim, J. Choi and C.-W. Kim, "Adaptive frequency with power-level tracking system for efficient magnetic resonance wireless power transfer." *Electronic Letters*, vol. 48, no. 8, pp. 452-454, April 2012.

[40] U. Jow, M. Kiani, X. Huo, and M. Ghovanloo, "Towards a smart experimental arena for long-term electrophysiology experiments," *IEEE Trans. on Biomed. Circuits and Systems*, vol. 6, no. 5, pp. 414–423, Oct. 2012.

[41] D. Russell, D. McCormick, A. Taberner, P. Nielsen, P. Hu, D. Budgett, M. Lim, and S. Malpas. "A high bandwidth fully implantable mouse telemetry system for chronic ECG measurement," Proc. *IEEE Eng. in Med. Biol. Conf*., pp. 7666–7669, Sep. 2011.

[42] TRM Implantable Telemetry System, Millar Inc., [Online] Available: http://millar.com/products/telemetry/
[43] S.A. Mirbozorgi, H. Bahrami, M. Sawa, and B. Gosselin, “A smart multicoil inductively-coupled array for wireless power transmission,” *IEEE Trans. Industrial Electronics*, DOI 10.1109/TIE.2014.2308138.
[44] N. Soltani, M. S. Aliroteh, and R. Genov, “Cellular inductive powering system for weakly-linked resonant rodent implants,” *IEEE BioCAS Conference,* pp. 350-353, Oct. 2013.
[45] K.M. Silay, C. Dehollain, and M. Declercq, “A closed-loop remote powering link for wireless cortical implants,” *IEEE Sensors,* vol. 13, no. 9, pp. 3226-3235, Sep. 2013.
[46] E.G. Kilinc, G. Conus, C. Weber, B. Kawkabani, F. Maloberti, and C. Dehollain, “A system for wireless power transfer of micro-systems *in-vivo* inplantable in freely moving animals,” *IEEE Sensors,* vol. 14, no. 2, pp. 522-531, Feb. 2014.
[47] L.H. Tecott and E. J. Nestler, “Neurobehavioral assessment in the information age,” *Nature Neuroscience*, vol. 7, no. 5, pp. 462-466, May. 2004.
[48] V.H. Deneberg, “Open-field behavior in the rat: what does it mean,” *Annals of N Y Acad Sci*, vol. 159, pp. 852-859, July. 1969.
[49] R.L. Clarke and R.F. Smith, “An infrared device for detecting locomotor activity,” *Behavior Research Methods, Instruments & Computers*, vol. 17, issue 5, pp. 519-525, Sep. 1985.
[50] C.J. Twining, C.J. Taylor, and P. Courtney, “Robust tracking and posture description for laboratory rodents using active shape models,” *Behavior Research Methods, Instruments & Computers*, vol. 33, issue 3, pp. 381-391, Aug. 2001.
[51] D.H. Godden and D. Graham, “`Instant’ analysis of movement,” *J. of exp. Biol.*, vol. 107, pp. 505-508, 1983.
[52] L.P.J.J. Noldus, A. J. Spink, and R.A.J. Tegelenbosch, “EthoVision: a versatile video tracking system for automation of behavioral experiments,” *Behavior Research Methods, Instruments & Computers*, vol. 33, issue 3, pp. 398-414, Aug. 2001.
[53] S. Kato, K. Tamada, Y. Shimada, and T. Chujo, “A quantification of goldfish behavior by an image processing system,” *Behavioural Brain Research*, vol. 80, issue 1-2, pp. 51-55, Oct. 1996.
[54] T-H Ou-Yang, M-L Tsai, C-T Yen, and T-T Lin, “An infrared range camera-based approach for three-dimensional locomotion tracking and pose reconstruction in a rodent,” *J. Neuroscience Methods*, vol. 201, issue 1, pp. 116-123, Sep. 2011.
[55] E. Whitmire, T. Latif, and A. Bozkurt, “Kinect-based system for automated control of terrestrial insect biobots,” *IEEE EMBS Conf.*, pp. 1470-1473, Jul. 2013.
[56] A. Alivisatos, M. Chun, G. Church, K. Deisseroth, J. Donoghue, R. Greenspan, P. McEuen, M. Roukes, T. Sejnowski, P. Weiss, and R. Yuste, "The brain activity map," *Science*, vol. 339, pp. 1284-1285, Mar. 2013.
[57] Christof Koch and R. Reid, “Observatories of the mind,” *Nature*, vol. 483, pp. 397-398, Mar. 2012.
[58] A. Alivisatos, M. Chun, G. Church, R. Greenspan, M. Roukes, and R. Yuste, “The brain activity map project and the challenge of functional connectomics,” *Neuron*, vol. 74, pp. 970-974, Jun. 2012.
[59] M. Ghovanloo and K. Najafi, “A modular 32-site wireless neural stimulation microsystem,” *IEEE J. Solid-State Circuits*, vol. 39, no. 12, pp. 2457-2466, Dec. 2004.
[60] D. Seo, J. Carmena, J. Rabaey, E. Alon, and M. Maharbiz, “Neural dust: an ultrasonic, low power solution for chronic brain-machine interfances,” *arXiv preprint*, 2013.
[61] W. Biederman, D. Yeager, N. Narevsky, A. Koralek, J. Carmena, E. Alon, and J. Rabaey, "A fully-integrated, miniaturized (0.125 mm2) 10.5 uW wireless neural sensor," *IEEE J. Solid State Circuits*, vol. 48, no. 4, pp. 960-970, Apr. 2013.
[62] N. Mano, “A 280 microW/cm2 biofuel cell operating at low glucose concentration,” *Chemical communications (Cambridge, England)*, no. 19 pp. 2221–3, May 2008.
[63] J.A. Paradiso and T. Starner, “Energy Scavenging for Mobile and Wireless Electronics,” *IEEE Pervasive Computing*, vol. 4, no. 1 pp. 18–27, Jan. 2005.
[64] E.K. Reilly and P.K. Wright, “Modeling, fabrication and stress compensation of an epitaxial thin film piezoelectric microscale energy scavenging device,” *J. of Micromechanics and Microengineering* , vol. 19, no. 9 p. 095014, Sep 2009.
[65] R. Vullers, R. Schaijk, H. Visser, J. Penders, and C. Hoof, “Energy harvesting for autonomous wireless sensor networks,” *IEEE Solid-State Circuits Magazine*, vol. 2, no. 2, pp. 29-38, Feb. 2010.

[66] A. Poon, S. O'Driscoll and T. Meng, "Optimal frequency for wireless power transmission into dispersive tissue," *IEEE Trans. Ant. Propagat.*, vol. 58, no. 5, pp. 1739-1750, May 2010.
[67] J. Rabaey, M. Mark, D. Chen, C. Sutardja, C. Tang, S. Gowda, M. Wagner, and D. Werthimer, "Powering and communicating with mm-size implants," *in Proc.*, DATE, pp. 1-6, June 2011.
[68] M. Zargham and P. Gulak, "Maximum achievable efficiency in near-field coupled power-transfer systems," *IEEE Trans. Biomed. Ckt. and Syst.*, vol. 6, no. 3, pp. 228-245, Jun. 2012.
[69] J.S. Ho, A.J. Yeh, E. Neofytou, S. Kim, Y. Tanabe, B. Patlolla, R.E. Beygui, and A.S.Y. Poon, "Wireless power transfer to deep-tissue microimplants." *Proc. of the National Academy of Sciences*, vol. 111, no. 22, pp. 7974-7979, April 2014.
[70] D. Ahn, and M. Ghovanloo, "Optimal design of wireless power transmission links for millimeter-sized biomedical implants," *IEEE Trans. Biomed. Circuits and Systems*, vol. 10, no. 1, Feb. 2016.
[71] A. Yakovlev, S. Kim, and A. Poon, "Implantable biomedical devices: wireless powering and communication," *IEEE Communications Magazine*, vol. 50, no. 3, pp. 152-159, Jan. 2013.
[72] R. Wu, S. Raju, M. Chan, J. K. O. Sin, and C. P. Yue, "Silicon-embedded receiving coil for high-efficiency wireless power transfer to implantable biomedical ICs," *IEEE Electron Device Letters*, vol. 34, no. 1, pp. 9-11, Jan. 2013.
[73] J. S. Ho, A. J. Yeh, E. Neofytou, S. Kim, Y. Tanabe, B. Patlolla, R. E. Beygui, and A. Poon, "Wireless power transfer to deep-tissue microimplants." *Proc. of the National Academy of Sciences*, vol. 111, no. 22, pp. 7974-7979, April 2014.
[74] B. Lee, D. Ahn, and M. Ghovanloo, "Towards a three-phase time-multiplexed planar power transmission to distributed implants," *IEEE Intl. Sym. on Circ. & Syst. Conf.*, pp. 1770-1773, May. 2015.
[75] M. Rizk, C.A. Bossetti, T.A. Jochum, S.H. Callender, M.A.L. Nicolelis, D.A. Turner, and P.D. Wolf, "A fully implantable 96-channel neural data acquisition system," *J. Neural Eng*., vol. 6, no. 2, art. 026002, Apr. 2009.
[76] H. Miranda, V. Gilja, C.A. Chestek, K.V. Shenoy, and T.H. Meng, "HermesD: a high-rate long-range wireless transmission system for simultaneous multichannel neural recording applications," *IEEE Trans. Biomed. Circuits and Systems*, vol. 4, no. 3, pp. 181-191, June 2010.
[77] S. B. Lee, "An inductive powered multichannel wireless implantable neural recording system (WINeR), *Dissertation*, Georgia Institute of Technology, 2014.
[78] F. Shahrokhi, K. Abdelhalim, D. Serletis, P. L. Carlen, and R. Genov, "The 128-channel fully differential digital integrated neural recording and stimulation interface," *IEEE Trans. Biomed. Circ. Syst*., vol. 4, no. 3, pp. 149-161, Jun. 2010.
[79] J. Lee, H. Rhew, D. R. Kipke, M. P. Flynn, "A 64 channel programmable closed-loop neurostimulator with 8 channel neural amplifier and logarithmic ADC," *IEEE J. Solid-State Circuits*, vol. 45, no. 9, pp. 1935-1945, Sept. 2010.
[80] M. Azin, D. J. Guggenmos, S. Barbay, R. J. Nudo, and P. Mohseni, "A battery-powered activity-dependent intracortical microstimulation IC for brain–machine–brain interface," *IEEE J. Solid-State Circuits*, vol. 46, no. 4, pp. 731-745, Apr. 2011.
[81] H. Lee and M. Ghovanloo, "An integrated power-efficient active rectifier with offset-controlled high speed comparators for inductively-powered applications," *IEEE Trans. Circuits Syst. I, Reg. Papers*, vol. 58, no. 8, pp. 1749-1760, Aug. 2011.
[82] B. Lee, M. Kiani, and M. Ghovanloo, "A triple-loop inductive power transmission system for biomedical applications," *IEEE Trans. Biomed. Circuits Syst,* Vol. 10, pp. 138-148, Feb. 2015.
[83] B. Lee, P. Yeon, and M. Ghovanloo, "A multi-cycle Q-modulation technique for wirelessly-powered biomedical implants," *IEEE Biomed. Cir. & Syst. Conf.*, pp. 1-4, Oct. 2015.
[84] B. Lee, P. Yeon, and M. Ghovanloo, "A multi-cycle Q-modulation for dynamic optimization of inductive links," *IEEE Trans. Industrial Electronics,* Vol. 63, pp. 5091-5100, April 2016.
[85] U. Jow, P. McMenamin, M. Kiani, and M. Ghovanloo, "EnerCage: a smart experimental arena with scalable architecture for behavioral experiments," *IEEE Trans. Biomed*. Eng., vol. 61, no. 1, pp. 139–148, Jan. 2014.
[86] M. Ghovanloo and S. Atluri, "A wide-band power-efficient inductive wireless link for implantable microelectronic devices using multiple carriers," *IEEE Trans. Ckt. and Syst. I*, vol. 54, no. 10, pp. 2211-2221, Oct. 2007.

[87] U. Jow and M. Ghovanloo, “Geometrical design of a scalable overlapping planar spiral coil array to generate a homogeneous magnetic field,” *IEEE Trans. Magnetics*, vol. 49, no. 6, pp. 2933-2945, Jun. 2013.
[88] D. Russell, D. McCormick, A. Taberner, P. Nielesn, P. Hu, D. Budgett, M. Lim, and S. Malpas, “Wireless power delivery system for mouse telemeter,” *IEEE BioCas*, pp. 273-276, Nov. 2009.
[89] H. Kobayashi, J. M. Hinrichs, and P. M. Asbeck, “Current-mode class-D power amplifiers for high-efficiency RF applications,” *IEEE Tran. Microwave Theory and Techniques*, vol. 49, no. 12, pp 2480-2485, Dec. 2001.
[90] T-P. Hung, A. G. Metzger, P. J. Zampardi, M. Iwamoto, and P. M. Asbeck, “Design of high efficiency current-mode class-D amplifiers for wireless handsets,” *IEEE Trans. Microwave Theory and Techniques*, vol. 53, no. 1, pp. 144-151, Jan. 2005.
[91] B. Lee, D. Ahn, and M. Ghovanloo, “Three-phase time-multiplexed planar power transmission to distributed implants,” *IEEE J. of Emerging and Selected Topics in Power Electronics,* Vol. 4, pp. 263-272, May 2015.
[92] H. Lee, K-Y Kwon, W. Li, and M. Ghovanloo, “A power-efficient switched-capacitor stimulating system for electrical/optical deep-brain stimulation,” *IEEE Intl. Solid State Cir. Conf.*, pp. 414-415, Feb. 2014.
[93] A. Kurs, A. Karalis, R. Moffatt, J. D. Joannopoulos, P. Fisher, and M. Soljacic, “Wireless power transfer via strongly coupled magnetic resonances,” *Science Express*, vol. 317, pp. 83-86, July 2007.
[94] S. B. Lee, M. Yin, J. R. Manns, and M. Ghovanloo, “A wideband dual antenna receiver for wireless recording from animals behaving in large arenas,” *IEEE Trans. Biomed. Eng*., vol. 60, no. 17, pp. 1993–2004, Jul. 2013.
[95] L. L. Chen, L-H Lin, E. J. Green, C. A. Barnes, and B. L. McNaughton, "Head-direction cells in the rat posterior cortex," *Experimental Brain Research*, vol. 101, no. 1, pp. 8-23, Sept. 1994.
[96] J. L. Calton, and J. S. Taube, "Degradation of head direction cell activity during inverted locomotion," *J. Neuroscience*, vol. 25, no. 9, pp. 2420-2428, Mar. 2005.
[97] M. A.P. Moita, S. Rosis, Y. Zhou, J. E. LeDoux, and H. T. Blair, “Hippocampal place cells acquire location-specific responses to the conditioned stimulus during auditory fear conditioning,” *Neuron*, vol. 37, no. 3, pp. 485-497, Feb. 2003.
[98] IEEE Standard for Safety Levels With Respect to Human Exposure to Radio Frequency Electromagnetic Fields, 3 kHz to 300 GHz, IEEE Standard C95.1-1991, 1992.
[99] K. Eom, J. Jeung, TH. Lee, J. Kim, J. Kim, J. Kim, SE. Lee, and SJ. Kim, “A wireless power transmission system for implantable devices in freely moving rodents,” *Medical & biological engineering & computing,* vol. 52, no. 8, pp. 639-651, Jun. 2014.
[100] B. Lee, M. Kiani, and M. Ghovanloo, “A smart wirelessly-powered homecage for long-term high-throughput behavioral experiments,” *IEEE J. of Sensors*, vol. 15, issue 9, pp. 4905-4916, Sept. 2015.
[101] S. B. Lee, B. Lee, B. Gosselin, and M. Ghovanloo, “A dual slope charge sampling analog front-end for a wireless neural recording system,” *Proc. IEEE 36st Eng. in Med. and Biol. Conf.*, pp. 3134-3137, Aug. 2014.
[102] S. B. Lee, B. Lee, M. Kiani, B. Mahmoudi, R. Gross, and M. Ghovanloo, "An inductively-powered wireless neural recording system with a charge sampling analog front-end," *IEEE J. of Sensors*, vol. 16, issue 2, pp. 475-484, Jan. 2016.
[103] J. del Valle and X. Navarro, "Interfaces with the peripheral nerve for the control of neuroprostheses," *Int. Rev. Neurobiol.,* vol. 109, pp. 63-83, 2013.
[104] X. Navarro et al., “A critical review of interfaces with the peripheral nervous system for the control of neuroprostheses and hybrid bionic systems,” *J. Peripher. Nerv. Syst.,* vol. 10, pp. 229–258, 2005.
[105] E. Kandel, J. Schwartz, and T. Jessell*, Principles of Neural Science*. New York: McGraw-Hill, 2000.
[106] R. Rieger, M. Schuettler, D. Pal, C. Clarke, P. Langlois, J. Taylor, N. Donaldson, “Very Low-Noise ENG Amplifier System Using CMOS Technology,” *IEEE Trans. Neural Systems Rehab. Eng.*, vol. 14, no. 4, pp. 427-437, Dec. 2006.
[107] F. M. Yaul and A. P. Chandrakasan, “A sub-uW 36nV/√Hz chopper amplifier for sensors using a noise-efficient inverter-based 0.2V-supply input stage,” *IEEE Intl. Solid-State Cir. Conf.*, pp. 94-95, Feb. 2016.
[108] F. Zhang, J. Holleman, and B. P. Otis, “Design of ultra-low power biopotential amplifiers for biosignal acquisition applications,” *IEEE Trans. Biomed. Circuits Syst.*, vol. 6, no. 4, pp. 344–355, Aug. 2012.

[109] Y. M. Dweiri, T. Eggers, G. McCallum, and D. M. Durand, "Ultra-low noise miniaturized neural amplifier with hardware averaging," *J. Neural Eng.*, vol. 12, pp. 1-10, June 2015.
[110] F. Wu, L. Tien, F. Chen, D. Kaplan, J. Berke, and E. Yoon, "A multi-shank silk-backed parylene neural probe for reliable chronic recording," *Solid-State Sensors, Actuators and Microsystems Conference*, pp. 888-891, 2013.
[111] O. F. Cota, D. Plachta, T. Stieglitz, S. Kundumattathil, Y. Manoli, and M. Kuhl, "In vivo characterization of a versatile 8-channel digital biopotential recording system with sub-μV_{RMS} input noise," *Proc. IEEE 38th Eng. in Med. and Biol. Conf.,* pp. 6311–6314, Aug. 2016.
[112] J. Simeral, S. Kim, M. Black, J. Donoghue, and L. Hochberg, "Neural control of cursor trajectory and click by a human with tetraplegia 1000 days after implant of an intracortical microelectrode array," *J. Neural Eng.*, vol. 8, p. 025027, 2011.
[113] R. R. Harrison and C. Charles, "A low-power, low-noise CMOS amplifier for neural recording applications," *IEEE J. Solid-State Circuits*, vol. 38, no. 6, pp. 958–965, Jun. 2003.
[114] A. Bagheri, M. T. Salam, J. L. P. Velazquez, and R. Genov, "Low-frequency noise and offset rejection in DC-coupled neural amplifiers: a review and digitally-assisted design tutorial," *Trans. Biomed. Circuits Syst.*, vol. PP, no. 99, pp. 1–16, Aug. 2016.
[115] R. Muller, S. Gambini, and J. M. Rabaey, "A 0.013mm^2 5μW DC-coupled neural signal acquisition IC with 0.5 V supply," *IEEE J. Solid-State Circuits*, vol. 47, no. 1, pp. 232–243, Jan. 2012.
[116] B. Gosselin, M. Sawan, and C. A. Chapman, "A low-power integrated bioamplifier with active low-frequency suppression," *IEEE Trans. Biomed. Circuits Syst.*, vol. 1, no. 3, pp. 184–192, Sep. 2007.
[117] K. A. Ng and Y. P. Xu, "A multi-channel neural-recording amplifier system with 90dB CMRR employing CMOS-inverter-based OTAs with CMFB through supply rails in 65nm CMOS," *IEEE Intl. Solid-State Cir. Conf.*, pp. 206-207, Feb. 2015.
[118] T. Wu, J. Xu, Y. Lian, A. Khalili, A. Rastegarnia, C. Guan, and Z. Yang, "A 16-channel nonparametric spike detection ASIC based on EC-PC decomposition," IEEE *Trans. Biomed. Circuits Syst.*, vol. 10, no. 1, pp. 3–16, Feb. 2016.
[119] J. Vidal, and M. Ghovanloo, "Towards a Switched-Capacitor Based Stimulator for Efficient Deep-Brain Stimulation," *Proc. IEEE 32nd Eng. in Med. and Biol. Conf.*, pp. 2927-2930, Aug. 2010.
[120] X. F. Wei and W. M. Grill, "Impedance characteristics of deep brain stimulation electrodes in vitro and in vivo," *J. of Neural Eng.*, vol. 6, no. 4, pp. 1-9, July 2009.
[121] T. J. Lee, C. L. Lee, Y. J. Ciou, C. C. Huang, and C. C. Wang, "All-MOS ASK demodulator for low-frequency applications," *IEEE Trans. Cir. Syst. II, Express Briefs*, vol. 55, no. 5, pp. 474-478, May. 2008.
[122] J. Wang, S. Liu, Q. Shen, H. Li, and Q. An, "A fully fledged TDC implemented in field-programmable gate arrays," *IEEE Trans. Nuclear Science*, vol. 57, no. 2, pp. 446-450, April. 2010.
[123] X. Zhang, and A. B. Apsel, "A low-power, process-and-temperature compensated ring oscillator with addition-based current source," *IEEE Trans. Cir. Syst. I, Reg. Papers*, vol. 58, no. 5, pp. 868-878, May. 2011.
[124] A. A. Abidi, "The path to the software-defined radio receiver," *IEEE J. Solid-State Circuits*, vol. 42, no. 5, pp. 954–966, May. 2007.
[125] BladeRF, [Online]. Available: http://nuand.com/
[126] GUN Radio, [Online]. Available: http://gnuradio.org/redmine/projects/gnuradio/wiki/
[127] ZeroMQ, [Online]. Available: http://zeromq.org/
[128] Y. Jia, Z. Wang, D. Canales, M. Tinkler, C. C. Hsu, T. E. Madsen, S. A. Mirbozorgi, D. Rainnie, and M. Ghovanloo, "A wirelessly-powered homecage with animal behavior analysis and closed-loop power control," *Proc. IEEE 38th Eng. in Med. and Biol. Conf.*, pp. 6323-6326, Aug. 2016.
[129] Tucker-Davis Technologies, [Online]. Available: http://tdt.com/
[130] Z. Wang, S. A. Mirbozorgi, and M. Ghovanloo, "Towards a Kinect-based behavior recognition and analysis system for small animals," *Proc. IEEE Biomed. Circuits Syst. Conf.*, pp. 1-4, Oct. 2015.
[131] Y. Choi, S. Park, Y. Chung, R. K. Gore, A. W. English, R. V. Bellamkonda, "PDMS microchannel scaffolds for neural interfaces with the peripheral nervous system", *Proc. IEEE 27th Int. Conf. Micro Electro Mech. Syst. (MEMS)*, pp. 873-876, Jan. 2014.
[132] D. J. Tyler and D. M. Durand, "Functionally selective peripheral nerve stimulation with a flat interface nerve electrode," *IEEE Trans. Neural Syst. Rehabil. Eng.*, vol. 10, no. 4, pp. 294-303, Feb. 2003.

[133] D. Seo, R. M. Neely, K. Shen, U. Singhal, E. Alon, J. M. Rabaey, J. Carmena, and M. M. Maharbiz, "Wireless recording in the peripheral nervous system with ultrasonic neural dusk," *Neuron*, vol. 91, no. 3, pp. 529-539, Aug. 2016.
[134] B. K. Thurgood, D. J. Warren, N. M. Ledbetter, G. A. Clark, and R. R. Harrison, "A wireless integrated circuit for 100-channel charge-balanced neural stimulation," *IEEE Trans. Biomed. Circuits Syst.*, vol. 3, no. 6, pp. 405–414, Dec. 2009.
[135] J. J. FitzGerald, N. Lago, S. Benmerah, J. Serra, C. P. Watling, R. E. Cameron, E. Tarte, S. P. Lacour, S. B. McMahon, and J. W. Fawcett, "A regenerative microchannel neural interface for recording from and stimulating peripheral axons in vivo," *J. Neural Eng.*, vol. 9, no. 1, pp. 029601, Mar. 2012.
[136] R. K, Gore, Y. Choi, R. Bellamkonda, and A. English, "Functional recordings from awake, behaving rodents through a microchannel based regenerative neural interface," *J. Neural Eng.*, vol. 12, no. 1, pp. 016017, Mar. 2015.
[137] Y. K. Lo, C. W. Chang, Y. C. Kuan, S. Culaclii, B. Kim, K. Chen, P. Gad, V. R. Edgerton, and W. Liu, "A 176-channel 0.5 cm^3 0.7g wireless implant for motor function recovery after spinal cord injury," *IEEE Intl. Solid-State Cir. Conf.*, pp. 382-384, Feb. 2016.
[138] R. Hossain, B. Kim, R. Pankratz, A. Ajam, S. Park, S. L. Biswal, and Y. Choi, "Handcrafted multilayer PDMS microchannel scaffolds for peripheral nerve regeneration," *Biomed. Microdevices*, vol. 17, no. 6, pp. 109, Dec. 2015.
[139] Triangle Biosystems International (TBSI), [Online]. Available: http://trianglebiosystems.com/.
[140] A. Ali, "Microwire regenerative peripheral nerve interfaces with wireless recording and stimulation capabilities," *Dissertation*, University of Texas Rio Grande Valley, 2016.